Evolution of deformation and collectivity away from magic numbers

Malin Klintefjord
Department of Physics
University of Oslo
May 2016

Acknowledgments

I am very thankful to my supervisors Andreas Görgen, Katarzyna Hadynska-Klek, Joa Ljungvall and Alfredo Galindo-Uribarri. You are all very supportive, wise and notable nuclear physicists. Andreas, thanks for your calmness and patience in our discussions. Kasia, you will always be my GOSIA-guru with a friendly and happy smile. Thank you for giving me perspective on both physics and the world outside. Joa, your efficiency and sense for details are highly appreciated and helped a lot to progress and stay motivated. Alfredo, thanks a lot for your hospitality during my stay at ORNL, for teaching me about Bragg detectors, supporting my running and showing me the city of Chicago.

I am also grateful to the whole Nuclear physics group at the University of Oslo. Thanks for all discussions and hytteturer. Many thanks to the Physics division at ORNL for making me a part of this group too, and to the subatomic physics group at Chalmers for your hospitality. I deeply appreciate the professional help and kindness I have received from the ISOLDE collaboration during experiments and analysis.

My thanks goes also to sportsklubben Vidar langdistanse gruppe, for all our fun, sunny, rainy, hard and easy runs and for teaching me a lot about Norwegian culture. Thanks to all my friends that are lighting up my days. And to my family, my sister Linda with husband and kids and my brother Martin, for always being there for me. To our wonderful mother Elisabeth, and to Leif, who took care of me as his own daughter. Thanks also to Iris for all your care.

Finally, I want to thank Boris for your endless love and support.

Malin Klintefjord

August 17, 2016

Contents

CONTENTS

Chapter 1

Introduction

The structure of the atomic nucleus has been intensely studied since its discovery in 1911. The nuclear structure is successfully described by the shell model, where protons and neutrons are placed in orbital shells corresponding to different energy levels. Nuclei with all its nucleons in closed shells are particularily stable while the nuclear properties are characterized by the valence nucleons in open shells. Away from the closed-shell nuclei, collective behavior of the nucleons give rise to deformed shapes. The question of how shapes evolve in open-shell regions have attracted physicists in the past decades. Many theoretical models have been developed to describe the collective behavior of nuclei. This thesis is focused on the experimental investigation of nuclear shape evolution around $N = 82$ and $Z = 28$. The predicted ground state deformations [1] are presented in Fig. 1.1, where the two regions of interest for this thesis are marked in circles.

To develop reliable models that can describe the nuclear properties, experimental data is crucial. Measurements of spectroscopic data in exotic nuclei away from stability are, however, limited by the short decay time and technical difficulties in producing the elements of interest. In this thesis the low lying structure and deformation of ^{140}Sm were investigated using the Coulomb excitation technique. For this purpose electromagnetic transition strengths and quadrupole moments were extracted. This experiment was made possible thanks to the recent improvements of post accelerated heavy ion beams and selective ionization schemes, allowing to produce an exotic ^{140}Sm beam at CERN-ISOLDE. Furthermore, spins of excited states in ^{140}Sm were investigated in a dedicated β-decay experiment at the Heavy Ion Laboratory in Warsaw.

The nuclei in the $A \approx 60$ region are of interest for nuclear structure, due to the vanishing shell gap at $N = 40$ and the onset of collectivity. Lifetimes
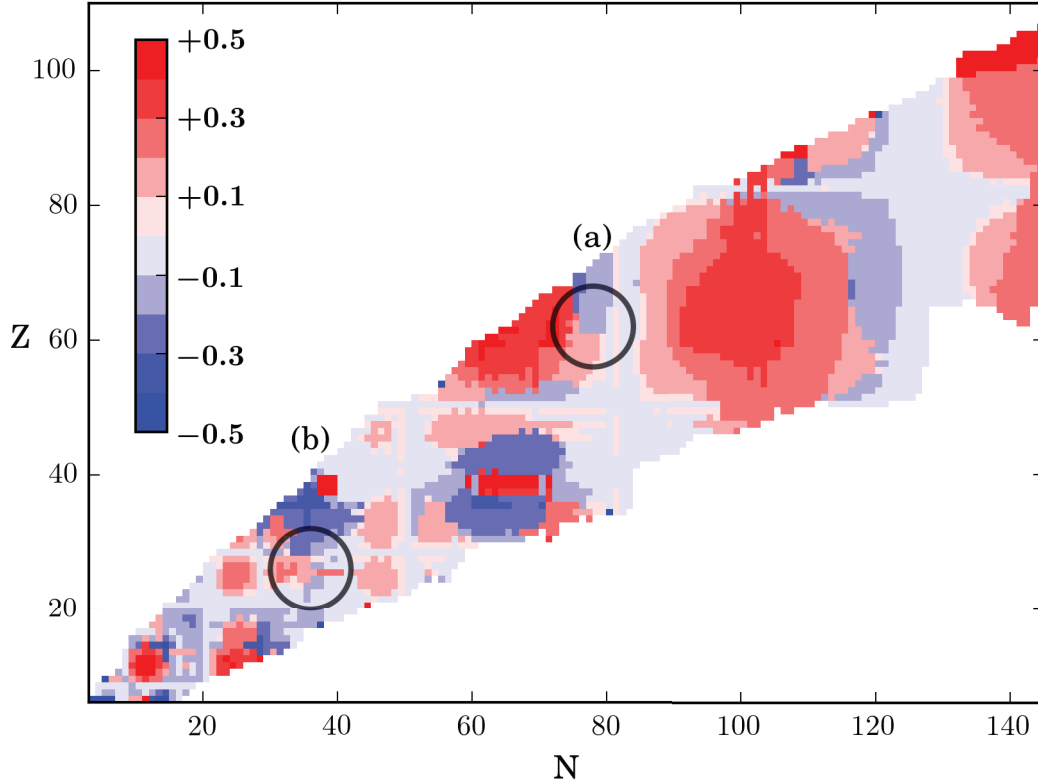
Figure 1.1: The ground-state β-deformation parameter (data from Ref. [1]) predicted for all nuclei. In this thesis nuclear structure in ^{140}Sm (marked in region (a)) and nuclei with $A \approx 60$ (marked in region (b)) are investigated.

of excited states were extracted from an experiment performed at GANIL, France, using the Recoil Distance Doppler Shift (RDDS) method.

In Coulomb excitation analysis, knowledge about the composition of the beam and energy loss of the target used in the reaction are crucial. Usually energy losses are calculated using Monte Carlo based programs. However, this can also be measured directly using Bragg detectors. As a part of this thesis, the assembling and testing of a Bragg detector at the Oak Ridge National Laboratory, USA, is presented.

This thesis is organized as follows: Chapter 2 gives an introduction to nuclear structure with the concepts and theoretical nuclear models relevant to this work. In Chapter 3, the analysis of the Coulomb experiment of ^{140}Sm at CERN-ISOLDE is described in details, while the ^{140}Sm angular correlation experiment at the Heavy Ion Laboratory, Warsaw, is presented in Chapter 4. Chapter 5 is dedicated to the RDDS lifetime measurement in ^{62,64}Fe, ^{61,63}Co and ^{59}Mn, performed at GANIL and Chapter 6 presents

the work with the Bragg detector done at Oak Ridge National Laboratory. Chapter 7 contains and describes the papers included in the thesis. Finally, conclusions and an outlook are given in Chapter 8.

Chapter 2

Motivation

In this chapter a brief introduction to the theory and concepts used in the analysis is given, with the purpose of facilitating further reading. For a better understanding, the reader is referred to detailed works in Refs. [2], [3] and [4].

In Section 2.1, nuclear deformation is discussed in terms of collective excitations in nuclei. Here, the theoretical models and important properties of γ decay are presented. Experimental techniques for the extraction of electromagnetic transition strengths are introduced in Section 2.2 and particle and γ detection techniques are explained in Section 2.3.

For more detailed motivations and introductions to the various experiments described in this thesis, the reader is referred to the respective papers, found in Chapter 7.

2.1 Theory

In nuclei with only one valence nucleon, the energy and spin of the nucleus in its ground state is determined by this single nucleon, as described by the Independent Particle Model [2]. In open-shell nuclei, the nucleon-nucleon interactions are significant and the spherical shape approximation is no longer valid. Instead, a deformed shape tends to be energetically more favored [3]. The surface of the nucleus can be described by the multipole expansion in Eq. (2.1) [3],

$$R(\theta, \phi) = R_0 \left(1 + \sum_{\lambda \geq 2} \sum_{\mu=-\lambda}^{+\lambda} \alpha_{\lambda\mu} Y_{\lambda\mu}(\theta, \phi) \right) \tag{2.1}$$

where R_0 is the average radius, α are expansion coefficients, λ is the multipole, μ is the order of the expansion and θ and ϕ are the intrinsic

angles and $Y_{\lambda\mu}$ are the spherical harmonics.

To first order, the deformation is given by a quadrupole deformation, $\lambda = 2$, with the expansion coefficients $\alpha_{20} = \beta\cos(\gamma)$ and $\alpha_{22} = \frac{1}{\sqrt{2}}\beta\sin(\gamma)$. For the axial symmetry, $\gamma = 0$ and $\beta > 0$ corresponds to the prolate deformed shape and $\gamma = 0$ and $\beta < 0$ corresponds to the oblate shape. In a triaxial shaped nucleus, $0 < \gamma < \frac{\pi}{3}$. An illustrative picture of nuclear shapes is shown in Fig. 2.1

$\beta = 0.0$ $\beta = -0.2$ $\beta = 0.2$ $\beta = 0.2$
$\gamma = 0°$ $\gamma = 0°$ $\gamma = 0°$ $\gamma = 30°$
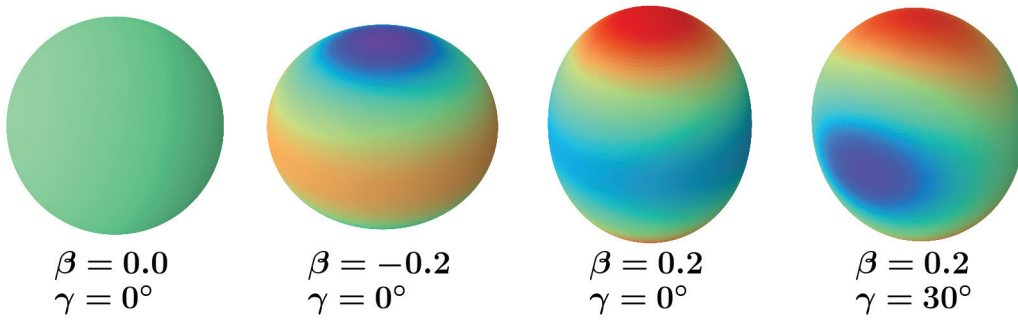
Figure 2.1: Spherical ($\gamma = 0$ and $\beta = 0$), prolate deformed ($\gamma = 0$ and $\beta > 0$), oblate deformed ($\gamma = 0$ and $\beta < 0$) and triaxial ($0 < \gamma < \frac{\pi}{3}$) nuclear shape.

The deformation parameter, β, is related to the intrinsic quadrupole moment, Q_0, given in Eq. (2.2),

$$Q_0 = \frac{3}{\sqrt{5\pi}}ZR_0^2(\beta + 0.16\beta^2), \tag{2.2}$$

where $R_0 = 1.2\,A^{1/3}$fm is the nuclear radius and Z is the proton number. Adding just a few nucleons outside a closed shell leads to a polarizing effect on the nuclear shape which is, however, reduced by the residual force in the nucleus. This results in a spherical shape that is sensitive to vibrations. In the vibrational model [3], the excited states are described in terms of vibrational oscillations due to collective behavior of the valence nucleons. The first excited state in the nucleus is given by an excited quadrupole phonon, hence $\lambda = 2$ implies that the first excited state is 2^+. Two phonon excitation results in a triplet of $0^+, 2^+$ and 4^+ state at the same energy, two times the energy value of the 2_1^+.

Further away from closed shells the polarizing effects dominate and the nucleus may rotate around its deformed shape. In the rotational model [5] the energy levels are given by Eq. (2.3),

$$E_J = \frac{\hbar^2}{2I}[J(J+1) - K^2], \tag{2.3}$$

where I is the moment of inertia, J is the total angular momentum, and K is the projection of J on the symmetry axis. This predicts the energy levels at $E(0^+) = 0$, $E(2^+) = 6(\frac{\hbar^2}{2I})$ $E(4+) = 20(\frac{\hbar^2}{2I})$. In the Davydov and Filippov model [6], energy levels are obtained assuming a well defined minimum in the nuclear potential as a function of deformation parameter γ. If the minimum is less well defined the nucleus is called γ soft and the Wilets-Jean model [7] may be applicable. In this model the nucleus vibrates smoothly between $\gamma = 0°$ and $\gamma = 60°$. Predicted excited states in the vibrational, rotational, Davydov and Filippov triaxial and γ-soft models are shown in Fig. 2.2.

(a)   **(b)**   **(c)**   **(d)**

$\underline{0^+ 2^+ 3^+ 4^+ 6^+}$ $3E_{\text{vib.}}$ $\underline{8^+}$ $72E_{\text{rot.}}$ $\underline{8^+}$ $96E_{\text{tri.}}$ $\underline{2^+ 4^+ 5^+ 6^+ 8^+}$ $28E_{\text{soft}}$

$\underline{4^+}$ $80E_{\text{tri.}}$

$\underline{4^+}$ $\underline{5^+}$ $72E_{\text{tri.}}$

$\underline{0^+}$ $\underline{2^+}$ $\underline{4^+}$ $2E_{\text{vib.}}$ $\underline{4^+}$ $68E_{\text{tri.}}$ $\underline{0^+}$ $\underline{3^+}$ $\underline{4^+}$ $\underline{6^+}$ $18E_{\text{soft}}$

$\underline{6^+}$ $\underline{6^+}$ $60E_{\text{tri.}}$

$\underline{6^+}$ $42E_{\text{rot.}}$

$\underline{2^+}$ $E_{\text{vib.}}$ $\underline{4^+}$ $\underline{3^+}$ $36E_{\text{tri.}}$ $\underline{2^+}$ $\underline{4^+}$ $10E_{\text{soft}}$

$32E_{\text{tri.}}$

$\underline{4^+}$ $20E_{\text{rot.}}$ $\underline{2^+}$ $24E_{\text{tri.}}$

$\underline{2^+}$ $12E_{\text{tri.}}$ $\underline{2^+}$ $4E_{\text{soft}}$

$\underline{2^+}$ $6E_{\text{rot.}}$

$\underline{0^+}$ —0 $\underline{0^+}$ —0 $\underline{0^+}$ —0 $\underline{0^+}$ —0
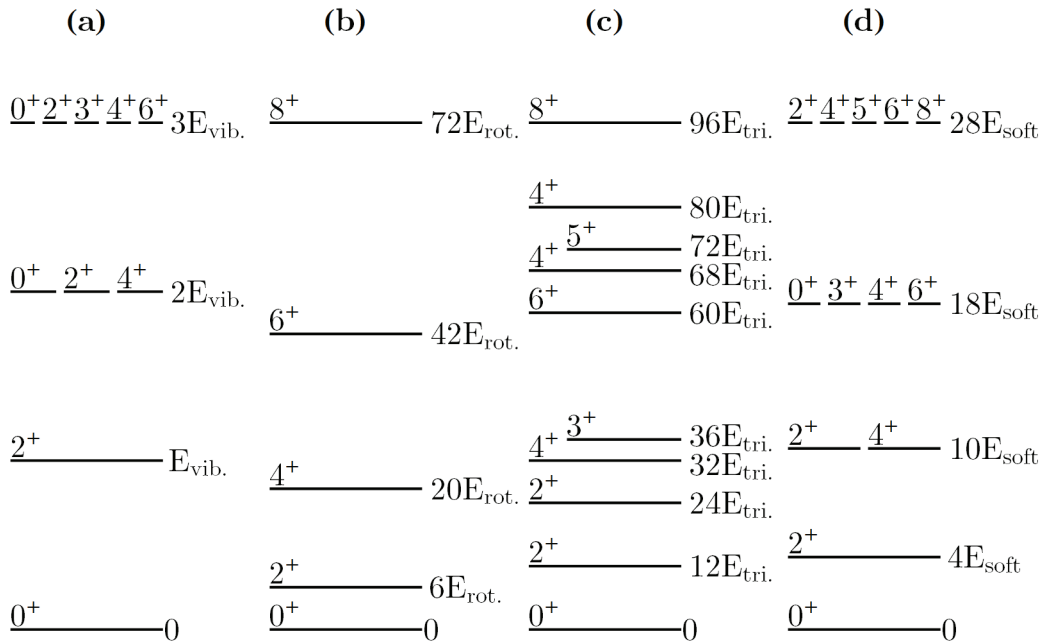
Figure 2.2: Excited states in the vibrational (a), the rotational (b), the Davydov and Filippov (for $\gamma = 30°$) (c) and the γ soft model (d).

Excited states with the lowest energy, for a given angular momentum, are called yrast states. Non-yrast bands are built on excited states with different J, occurring due to single-particle excitations or vibrations in deformation parameters β and γ. A band built on an intrinsic state with spin $J \neq 0$ will have the spin sequence: J, $J + 1$, $J + 2$, …. If states belonging to bands with different intrinsic deformations have similar energies, the *shape coexistence* phenomenon occurs. Shape coexistence has been experimentally found in nuclei since 1956. It was first believed to be a rare phenomenon in nuclei situated on some isolated islands in the

nuclear chart. However, today both experimental findings and theoretical models indicate that it occurs almost all over the nuclear landscape [8].

2.1.1 γ decay

The de-excitation of low-lying nuclear excited states is mainly due to the electromagnetic discrete transitions, where γ photons or conversion electrons are emitted. When a nucleus decays from an excited state via photon emission, the angular momentum, l, carried by the photon, is limited by the coupling rules stated in Eq. (2.4) [9],

$$|I_i - I_f| \leq l \leq |I_f + I_i|$$
$$l > 0,$$
(2.4)

where I_i and I_f are the initial and final states, respectively. The multipolarity of the transition is defined as a 2^l-pole, meaning that $l = 1$ is a dipole, $l = 2$ is a quadrupole etc. The parity of the transition, $\pi = \pi_i \pi_f$, where π_i and π_f are the parity of the initial and final states, respectively, is $(-1)^l$ for an electric transition ($E\lambda$) and $(-1)^{l+1}$ for a magnetic transition ($M\lambda$). Usually the transition is dominated by the lowest possible allowed multipolarity [9].

For an electric quadrupole transition, the reduced transition probability, $B(E2)$ value, is related to the transitional matrix element in Eq. (2.5) [3],

$$B(E2; I_i \rightarrow I_f) = \frac{|\langle I_f ||E2|| I_i \rangle|^2}{2I_i + 1}.$$
(2.5)

In the single particle model the strength of an electric quadrupole transition is equal to one Weisskopf Unit. One Weisskopf Unit for a ($2 \rightarrow 0$) transition is given in Eq. (2.6) [3],

$$B(E2) = 5.940 \times 10^{-6} A^{4/3} e^2 b^2.$$
(2.6)

A $B(E2)$ much larger than $1\,\text{W.u.}$ indicates a collective behavior of the nucleus. The spectroscopic quadrupole moment in the laboratory frame, Q_s, related to the shape of the nucleus, is in turn given by the diagonal matrix element in Eq. (2.7) [3].

$$Q_s(I) = \sqrt{\frac{16\pi}{5}} \frac{\langle II20|II \rangle}{\sqrt{2I+1}} \langle I ||E2|| I \rangle,$$
(2.7)

where $\langle II20|II \rangle$ is a Clebsch-Gordan coefficient. In the rotational model the relation between Q_s and the quadrupole moment in the intrinsic frame, Q_0, is given by Eq. (2.8),

$$Q_s = Q_0 \frac{3K^2 - I(I+1)}{(2I+3)(I+1)}.$$

(2.8)

Furthermore, the $B(E2)$ value is directly connected to the lifetime, τ, of the state by Eq. (2.9) [10],

$$\tau_i[ps] = \frac{40.81 \cdot 10^{13} E^{-5}[keV]}{B(E2; I_i \to I_f)[e^2b^2]} \frac{1}{1+\alpha},$$

(2.9)

where α are the internal conversion coefficients. Thereby measurement of lifetimes and $B(E2)$ values can provide insight into the collective behavior of the nuclei.

2.1.2 Shell model calculations

In the shell model [11], nuclear properties are predicted by solving the many-body problem consisting of the valence protons and neutrons outside an inert core. The nucleons are treated as independent particles and the nucleon-nucleon interaction is based on empirical fitting of two-body-matrix elements or on microscopic interactions, for example the CD-Bonn potential [12]. However, the valence space requires fine-tuning of parameters and introduction of effective charges of the protons and neutrons, only valid in that valence space and core. The shell model applies well for small systems with few nucleons. In particular, shell model calculations were suitable to successfully reproduce experimental data in the iron region, presented in this thesis, where a ^{48}Ca core was used.

In the case of the heavier nuclei, such as ^{140}Sm, shell model calculations are more challenging. In this thesis, calculations obtained using a ^{100}Sn core, 12 valence protons and 28 valence neutrons are presented. The large matrix dimensions of about 10^{11} requires truncation schemes to carry out the calculations.

2.1.3 The Interacting Boson Model

Since the increasing number of nucleons in heavier nuclei makes the number of configurations in the shell model huge, other approaches are

developed to decrease the model space. In the Interacting Boson Model (IBM) [13] it is assumed that the nucleons in the low-lying states are coupled together in so-called nucleon pairs, behaving like bosons, with total spin equal to either 0 or 2. In this model, the s-bosons ($l = 0$) and d-bosons ($l = 2$) dominate the interaction. The Hamiltonian used to describe the interaction contains parameters that like the effective charges in the shell model, are only valid in the specific space.

In the first version of IBM, no distinction between protons and neutrons are made. However, for heavier nuclei ($A > 50$) with $N > Z$ the valence protons and neutrons occupy different orbitals due to the Coulomb force between the protons. In this region, the extended version (IBM-2) [14], which applies the distinction, is needed. Paper 3 presents calculations in ^{140}Sm, obtained using IBM-2.

2.1.4 Mean-field based calculations

Another method to handle nuclei with a large number of valence nucleons is the mean-field approach [15]. In this method, the nucleons are treated as independent particles surrounded by an effective field from the other nucleons. This model is well suited for nuclei with many valence nucleons and does not rely on any effective charges. Only the parameters of the nuclear interaction have to be fitted to known data.

In this thesis, the energies and transition strengths in ^{140}Sm are compared to calculations based on the Constrained-Hartree-Fock-Bogoliubov (CHFB) method using the Gogny D1S interaction [16, 17], which is globally used over the nuclear chart. These calculations generate an energy potential surface in the plane spanned by the deformation parameters, β and γ, as seen in Fig. 12 in Paper 3. For calculations of transition strengths and quadrupole moments in ^{140}Sm, the Generator Coordinate Method (GCM) with Guassian Overlap Approximation (GOA) was used with a five dimensional collective quadrupole Hamiltonian [18]. The model is limited to calculations of positive parity states due to symmetry. The calculations are reliable up to spin $J = 6$.

Mean-field based calculations were also performed for nuclei in the iron region. In this region this approach is more demanding due to the decreased collectivity, arising close to the $Z = 28$ shell and makes the assumption used in the CGM+GOA approximations less valid.

2.2 Experimental techniques

In this section experimental techniques used for measuring electromagnetic transition strengths and quadrupole moments are discussed. The section describes two complementary methods, low-energy Coulomb excitation and Recoil Distance Doppler Shift (RDDS), a technique to measure lifetimes of excited states.

2.2.1 Coulomb excitation method

Elastic scattering of nuclei, known as Rutherford scattering, occurs when a target is bombarded by a projectile that passes through the target without entering the nucleus, in a monopole-monople interaction. If either the projectile or target nucleus is inelastically scattered in a monople-multipole or multipole-monopole interaction, the process is called Coulomb excitation. Both the projectile and target may also be simultaneously excited in a multipole-multipole interaction, although this process is less likely. The Coulomb excitation process is illustrated in Fig. 2.3.
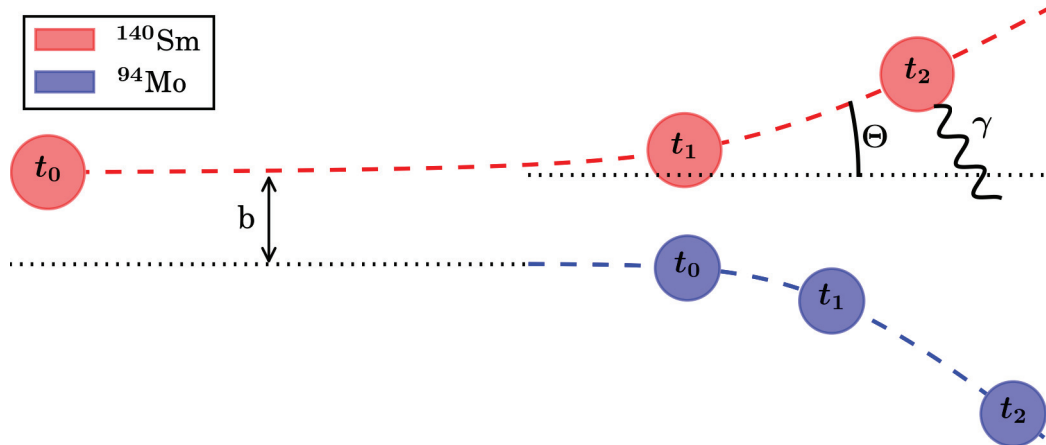
Figure 2.3: Illustration of the Coulomb excitation process. Between t_0 and t_1 the ^{140}Sm projectile passes through the ^{94}Mo target, with the impact parameter b, and is inelastically scattered with an angle θ. At t_2 the nucleus de-excites by emission of a γ photon.

In the semi-classical approach of Coulomb excitation theory [4], the excitation probability after the collision is described by quantum mechanics, while the relative motion of the projectile and the target are described by hyperbolic orbits. This requires a small value of the de Broglie wavelength,

λ, compared to the dimensions of the impact parameter, b. The ratio defines the Sommerfeld parameter given in Eq. (2.10) [4],

$$\eta = \frac{b}{2\lambda} = \frac{Z_p Z_t e^2}{\hbar v},\tag{2.10}$$

were Z_p and Z_t are the atomic numbers of the projectile and the target nucleus, respectively and v is the relative velocity. For a pure electromagnetic interaction, with a negligible contribution from the strong nuclear force, the distance of closest approach, d, has to fulfill the empirical condition given in Eq. (2.11) [19],

$$d > 1.25(A_p^{1/3} + A_t^{1/3}) + 5 \text{ fm},\tag{2.11}$$

where A_p and A_t are the mass numbers of the projectile and the target nucleus, respectively. This corresponds to the maximum beam energy in Eq. (2.12),

$$E_{max}(MeV) = 1.44 \frac{A_p + A_t}{A_t} \frac{Z_p Z_t}{1.25(A_p^{1/3} + A_t^{1/3}) + 5}.\tag{2.12}$$

Furthermore, the excitation energy, ΔE, is required to be small enough to ensure that the orbits of the reaction partners are not modified in the semi classical approach. The condition on the adiabaticity parameter, ξ, is described by Eq. (2.13),

$$\xi = \eta \frac{\Delta E}{E} \leq 1.\tag{2.13}$$

The differential cross section for Rutherford scattering as a function of scattering angle is given by Eq. (2.14) [4],

$$\frac{d\sigma_r}{d\Omega} = \left(\frac{Z_1 Z_2 e^2}{8\pi\epsilon_0 m v_0^2} \right)^2 \cdot \frac{1}{\sin^4(\frac{\theta}{2})},\tag{2.14}$$

where Z_1 and Z_2 are the atomic number of the projectile and the target, e is the electric charge, m is the mass of the projectile, v_0 is the velocity of the projectile in the center of mass frame and ϵ_0 is the vacuum permittivity. The cross section for Coulomb excitation of the projectile or the target is given by the product of the Rutherford cross section and the excitation probability, P, given in Eq. (2.15).

$$P_{I_i \rightarrow I_f} = \frac{1}{2I_i + 1} \sum_{M_i, M_f} |b_{if}^2|,\tag{2.15}$$

where I_i is the spin of the initial state and I_f is the spin of the final state. M_i and M_f are the magnetic quantum numbers and b_{if} are the transition amplitudes, expressed using first-order perturbation theory in Eq. (2.16).

$$b_{if} = \frac{1}{i\hbar} \int_{-\infty}^{\infty} \langle f|H(t)|i\rangle e^{i\frac{E_f - E_i}{\hbar}t} dt. \qquad (2.16)$$

Here $H(t)$ is the interaction energy, which in a pure electromagnetic excitation can be expanded in electric and magnetic multipole moments.

The cross section for the magnetic component of the excitation is suppressed with a factor $(v/c)^2$ compared to the electric component. In safe Coulomb excitation, with low beam energies, the excitation is therefore dominated by electric excitations. Because of the fact that the population of states in Coulomb excitation depends on the scattering angle, the angular γ-ray distribution from the de-excitation is non-uniform and described in the case of a $E2$ transition in Eq. (2.17).

$$W(\theta_\gamma, t) = 1 + a_2 G_2(t) P_2(\cos(\theta_\gamma)) + a_4 G_4(t) P_4(\cos(\theta_\gamma)). \qquad (2.17)$$

Here a_n are coefficients and P_n are Legendre polynomials. G_2 and G_4 are attenuation factors to account for deorientation effects caused by the distortion due to hyperfine interaction between the nuclei and the surrounding electrons.

If the excited states are populated from an intermediate state in so-called multiple step excitation, second order corrections to Eq. (2.16) are needed. This is usually the case when the 4_1^+ state in an even-even nucleus is populated, because the cross section for $E4$ transition from the ground state is weak compared to $E2$ from the 2_1^+ to 4_1^+ state. In this case the probability of populating the 4^+ is proportional to the product of $P_{0\rightarrow 2}$ and $P_{2\rightarrow 4}$. Another second order effect, called reorientation, occurs if the excitation from the initial to the final state goes via a magnetic substate, z, to the final state. This intermediate transition from z to f is due to the interaction with the quadrupole moment of the final state. The excitation probability, $P_{0\rightarrow 2}^{(2)}$ using second order perturbation will then be modified according to Eq. (2.18).

$$P_{0\rightarrow 2}^{(2)} = P_{0\rightarrow 2}^{(1)} \left(1 + \frac{A_p \Delta E \langle 2_1^+ \|E2\| 2_1^+ \rangle}{Z_p(1 + A_p/A_t)} \cdot K(\vartheta, \epsilon) \right), \qquad (2.18)$$

where $K(\vartheta, \xi)$ is a function that depends on the scattering angle and the adiabaticity. The contribution from the quadrupole moment can either lower or increase the total Coulomb excitation cross section. In this way

the cross section is sensitive to the sign of the spectroscopic quadrupole moment. To extract $B(E2)$ values from experimentally obtained γ intensities, theoretical yields are calculated for various matrix elements and fitted to the data. Moreover, the measurement of differential cross sections, as a function of particle scattering angle, provides more observables and may allow extraction of the spectroscopic quadrupole moment from the Coulomb excitation data. In this thesis the GOSIA [20] and GOSIA2 coupled channel codes were used to perform the fit in a least squares minimization routine.

2.2.2   The RDDS method

Transition strengths can also be extracted from lifetime measurements, using Eq. (2.9). In contrast to Coulomb excitation, a lifetime measurement does not depend on reorientation effects. The recoil distance Doppler shift (RDDS) method [21] is applicable to lifetime measurements in the range from 10^{-12} to 10^{-8} seconds. In this method, the different Doppler shift of a γ photon emitted before and after a metallic stopper or degrader foil, is used. In a traditional *stopper* the particles are fully stopped while a thinner *degrader* only reduces the velocity. In the experiment leading to the extraction of lifetimes in the $A \approx 60$ region, described in this thesis, a degrader was used to allow for particle identification in a magnetic spectrometer.

To extract the lifetime of an excited state, the degrader is placed at a distance, d, from the target, so that the flight time is comparable to the lifetime of the state. The γ spectra, Doppler corrected for the velocity after the degrader, will have a shifted component corresponding to the photons emitted before the degrader. By changing the distance, the relative intensity of the shifted and unshifted component can be studied as a function of d. The device used to accurately control the distance is called a plunger [21]. The setup is illustrated in Fig. 2.4

The γ photons emitted before the degrader are Doppler shifted according to Eq. (2.19),

$$E = E_0 \left(\frac{\sqrt{1 - \beta^2}}{1 - \beta \cos(\theta)} \right), \tag{2.19}$$

where $\beta = \frac{v}{c}$ is the velocity before the degrader and θ is the gamma emission angle. The number of γ photons emitted before and after the degrader are given by Eq. (2.20) and Eq. (2.21), respectively.

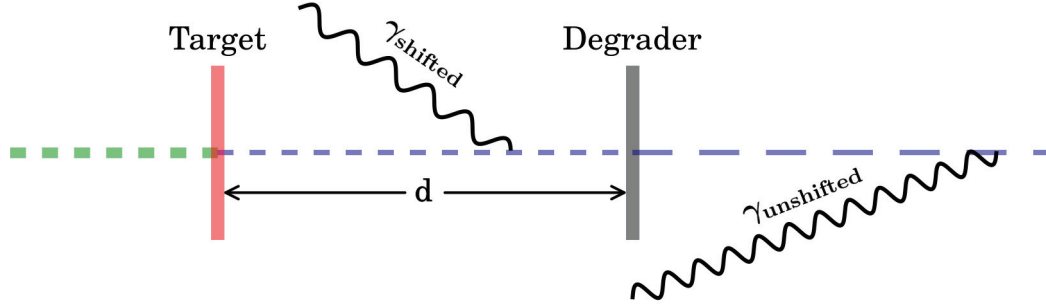$$I_s = N_0 exp(\frac{-d}{v\tau}). \tag{2.20}$$

Figure 2.4: In the RDDS method, the different Doppler shift of a γ photon emitted before and after a metallic degrader foil is used to extract the lifetime of an excited state. The degrader is placed at a distance, d, from the target, comparable to the lifetime of the state multiplied by the recoil velocity.

$$I_u = N_0(1 - exp(\frac{-d}{v\tau})). \tag{2.21}$$

Here τ is the mean lifetime and v is the velocity before the degrader. In the Differential Decay Curve Method (DDCM) [21], the decay curve, R, defined in Eq. (2.22), is used to obtain the mean lifetime.

$$R = \frac{I_u}{I_u + I_s} = exp(\frac{-d}{v\tau}). \tag{2.22}$$

In the case of feeding from higher excited states, the mean lifetime differs from the lifetime of the state i, and I_u and I_s depend on the feeding according to Eq. (2.23) [21],

$$\tau_i(t) = \frac{-N_i(t) + \Sigma_h b_{hi} N_h(t)}{\frac{dN_i(t)}{dt}}, \tag{2.23}$$

where h sums over all feeding transitions. Incomplete information about the feeding induces a source of error in the analysis. If the statistic allows, this problem can be solved by applying a $\gamma - \gamma$ coincidence gate on a known feeding transition [21], see Fig. 2.5 for an illustration. If the statistics is poor, seen feeding transitions together with assumptions about unseen feeding have to be included in the lifetime extraction. Excluding the feeding in general leads to an overestimation of the lifetime.
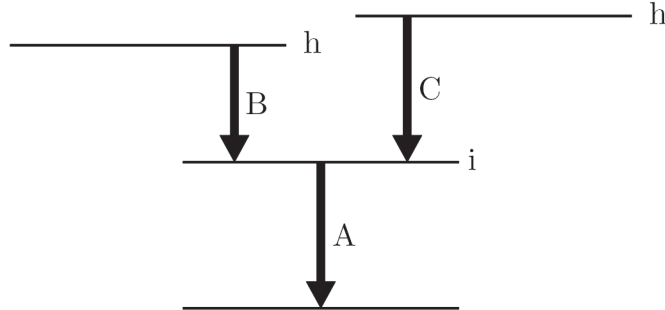
Figure 2.5: Incomplete information about the feeding transition, C induces a source of error in the extraction of the lifetime of state *i*. If the statistic allows, this problem can be solved by a direct $\gamma - \gamma$ coincidence gate on the known feeding transition, B.

2.2.3 γ-γ angular correlation

When a nucleus de-excites via a cascade of γ decays, as shown in Fig. 2.6, the probability distribution depends on the relative angle between the photons. The emission of the first γ ray defines a quantization axis and the angular distribution of the second γ ray is measured with respect to that axis. Note that this ignores any orientaion effects from the way the initial state is created. The angular dependence is theoretically given by
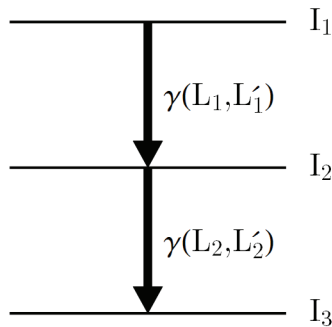
Figure 2.6: The emission of the first γ-ray ($I_1 \rightarrow I_2$) defines the quantization axis and the angular distribution of the second γ-ray ($I_2 \rightarrow I_3$) is measured with respect to that axis.

Eq. (2.24) [22],

$$W(\theta) = 1 + A_{22}P_2(\cos(\theta)) + A_{44}P_4(\cos(\theta)), \qquad (2.24)$$

where P_k are Legendre polynomials and A_{kk} are given by Eq. (2.25) [22].

$$A_{kk}(\delta_1, \delta_2) =$$
$$\frac{1}{1+\delta_1^2}\left[F_k(L_1, L_1, I_1, I_2) + 2\delta_1 F_k(L_1, L_1', I_1, I_2) + \delta_1^2 F_k(L_1', L_1', I_1, I_2)\right] \times$$
$$\frac{1}{1+\delta_2^2}\left[F_k(L_2, L_2, I_3, I_2) + 2\delta_2 F_k(L_2, L_2', I_3, I_2) + \delta_2^2 F_k(L_2', L_2', I_3, I_2)\right]. \quad (2.25)$$

Here, δ is the mixing parameter for $L \rightarrow L'$ transition from state I_i to I, defined as $\delta^2(L/L', J_1 \rightarrow J_2) = \frac{T(L, J_1 \rightarrow J_2)}{T(L', J_1 \rightarrow J_2)}$, where T is the transition probability. F_k are calculated from the expression in Eq. (2.26) [23].

$$F_k(L, L', I_i, I) = (-1)^{I_i + I - 1}[(2L+1)(2L'+1)(2I+1)(2k+1)]^{\frac{1}{2}} \times$$
$$\begin{pmatrix} L & L' & k \\ 1 & -1 & 0 \end{pmatrix} \begin{Bmatrix} L & L' & k \\ I & I & I_i \end{Bmatrix}. \quad (2.26)$$

In a $(0^+ \rightarrow 2^+ \rightarrow 0^+)$ cascade, the transitions are of pure $E2$ character and the values of A_{22} and A_{44} can be unambiguously determined, while a $(2^+ \rightarrow 2^+ \rightarrow 0^+)$ cascade implies a dependence of the mixing ratio δ of the $2^+ \rightarrow 2^+$ transition. Theoretical values of A_{22} and A_{44} for a $(0^+ \rightarrow 2^+ \rightarrow 0^+)$ or $(2^+ \rightarrow 2^+ \rightarrow 0^+)$ cascade, for different mixing ratios are shown in Fig. 2.7.
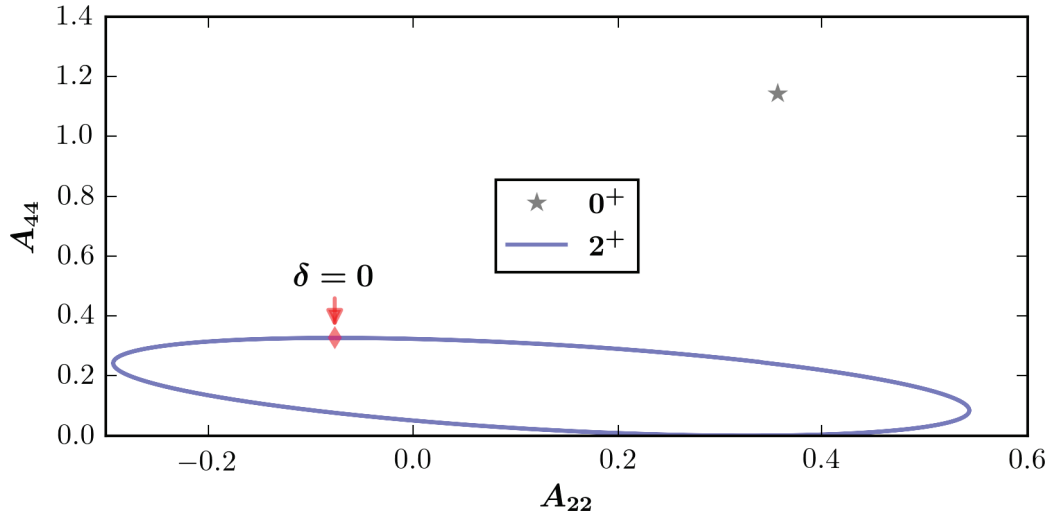
Figure 2.7: Theoretical values of A_{22} and A_{44}. In a $(0^+ \rightarrow 2^+ \rightarrow 0^+)$ cascade, the transitions are of pure $E2$ character and the values of A_{22} and A_{44} can be unambiguously determined, while a $(2^+ \rightarrow 2^+ \rightarrow 0^+)$ cascade implies a dependence of the mixing ratio δ of the $2^+ \rightarrow 2^+$ transition.

2.3   Particle and γ detection

In the Coulomb excitation experiment, described in Chapter 3, semiconducting silicon strip detectors were used for charged particle detection. In a semiconducting material, the charged particles hitting the detector create electron-hole pairs. The drift of electrons and holes, caused by the applied reverse voltage, generates a signal proportional to the particle energy. The high density of the ionizing material in a semiconductor leads to high efficiency and good energy resolution [9].

In the project described in Chapter 6, gas-filled detectors were used for charged-particle detection and identification. Ionization chambers operate on the principle that ions entering a gas (for example CH_4, CF_4 or C_4H_{10}) deposit energy, creating secondary electrons. When entering the gas the particle loses energy in various processes and if the transferred energy is above the binding energy for the electron (typically 10-25 eV), an ion pair, consisting of a positive ion and a free electron can be formed. An applied voltage potential creates an electric field in the gas that causes a drift of electrons towards the anode and the charge collected at the anode is proportional to the number of ion pairs created in the gas [9].

For detection of γ photons, either scintillation detectors or semiconductor based detectors can be used. Scintillation detectors usually yield

a high efficiency but poor resolution, while a semiconductor detector yields a good resolution [24]. In the experiments presented in this thesis, three types of semiconductor based on High-purity Germanium detectors were used for γ detection. In the β-decay experiment described in Chapter 4, where the decaying particles are stopped, standard unsegmented coaxial Germanium detectors were used. However, for the photons from the faster particles in the Coulomb excitation with the exotic beam, described in Chapter 3, more accurate information about the location of the γ interaction in the detector was needed to obtain a suffcient Doppler correction of the measured γ rays. This was possible due to the better position sensitivity of the segmented MINIBALL [25] clusters used in this experiment. For the study of lifetimes in the $A \approx 60$ region, presented in Chapter 5, the AGATA array [26] was used to detect the emitted γ photons. The tracking algorithms allowed for full reconstruction of the γ trajectories in the crystal, as further explained in Chapter 5.

At energies above about 200 keV, the energy dependence of the efficiency of Germanium detectors follow approximately the empirical formula given in Eq. (2.27) [27],

$$\ln(\epsilon(E)) = p_0 + p_1 \cdot \ln\left(\frac{E}{1000}\right) + p_2 \cdot \ln\left(\left(\frac{E}{1000}\right)^2\right), \qquad (2.27)$$

where p_0, p_1 and p_2 are fit parameters. In this work, γ sources with well known intensities were used to obtain relative efficiency curves, $\epsilon(E)$.

Chapter 3

^{140}Sm Coulomb excitation experiment

As discussed in Chapter 2, nuclei with open shell structure tend to be deformed. For nuclei with Z and N > 50, the deformation is predominantly prolate, with the exception of regions with holes in high-spin, low-Ω orbitals near the top of the proton and neutron shells [3]. In nuclei close to the transition from prolate to oblate ground state deformation, coexistence of shapes may occur at low excitation energies. Examples of this were found in the $Z = 82$ region near neutron mid-shell for ^{186}Pb [28] and Hg isotopes [29]. The same phenomenon may be expected near proton mid-shell at $N \approx 78$. Lifetime measurements have found evidence of coexisting rotational bands at higher excitation energies in ^{140}Sm, where two bands built on two isomeric 10^+ states are consistent with prolate and oblate shape, respectively [30].

At the beginning of the data analysis presented in this thesis, transition strengths and lifetimes of states below the isomers were completely unknown. In Ref. [31] the state at 990 keV excitation energy was assigned as (0^+). Such low lying 0_2^+ could possibly be an indication of shape coexistence in the nucleus. However, the spin was reassigned to 2^+ in the course of the data analysis presented in Chapter 4. The level scheme of ^{140}Sm, shown in Fig. 3.1 is known from fusion-evaporation [31] and β-decay experiments from ^{140}Eu [32, 33].

The goal of the Coulomb excitation experiment presented here was to obtain information about the transition strengths below the 10^+ isomeric states. The $B(E2)$ values and quadrupole moments in ^{140}Sm were investigated using Coulomb excitation of a ^{140}Sm beam on a ^{94}Mo target. Known transition strengths in ^{94}Mo served as normalization of the transition strengths in ^{140}Sm.
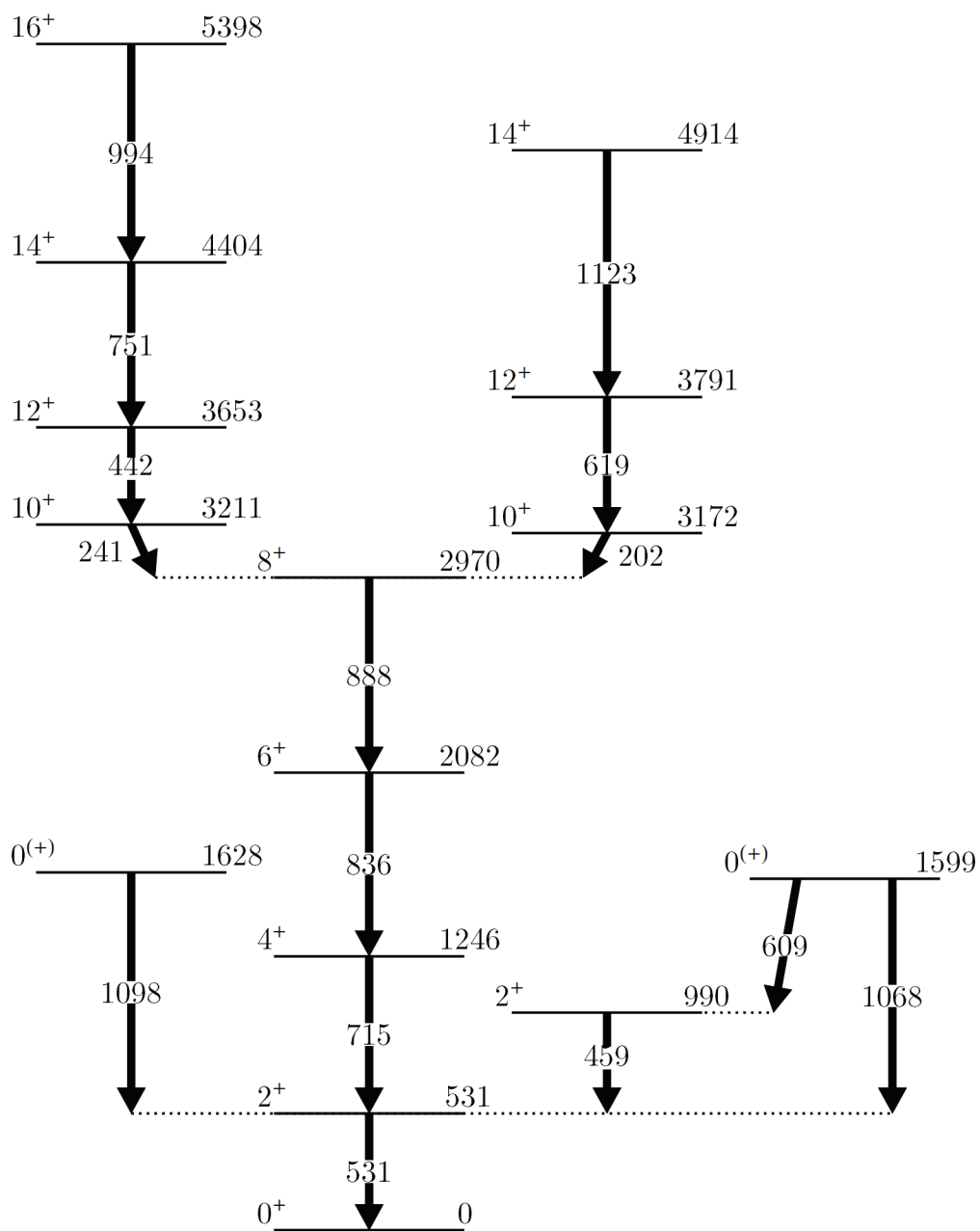
Figure 3.1: Level scheme for ^{140}Sm, known from fusion-evaporation and β-decay experiments from ^{140}Eu. In this work the structure below the 10^+ isomeric states were studied.

In this chapter an experiment to measure the Coulomb excitation of ^{140}Sm is presented. Section 3.1 gives an introduction to the CERN-ISOLDE facility, while the experiment is described in Section 3.2. The data analysis and the extraction of transition strenghts, using GOSIA and GOSIA2, are presented in Section 3.3 and 3.4 respectively. Finally, the results are compared to theoretical predictions in Section 3.5.

3.1 The ISOLDE facility

ISOLDE is an Isotope Separator On Line (ISOL) radioactive ion beam facility located at CERN, Geneva, Switzerland. Experiments have been performed at this facility since the 1960s and important upgrades with the installation of a post-accelerator were made in 2001 [34].

3.1.1 Beam production

Bunches of protons of 1.4 GeV energy and 2 μA intensity from the PS Booster hit a thick target to produce radioactive nuclei in spallation, fission or fragmentation processes. The time between two proton bunches is 1.2 s. For the ^{140}Sm Coulomb excitation experiment, a tantalum production target was used. The reaction products were selected in an ion source, using stepwise resonant laser ionization (RILIS) equipped with GdB_6 low-work function cavity [35, 36]. ISOLDE is equipped with two different mass separators, the General Purpose Separtor (GPS) with one bending magnet and the High Resolution Separator (HRS) with two bending magnets. To select $A = 140$, the GPS was used. The ions are then accumulated, bunched and cooled in the penning trap (REXTRAP) [37], before they are transferred to the electron beam ion source (REXEBIS) [38]. They are then slowed down by collision with a buffer gas of Neon or Argon. In REXEBIS the ions are charge-bred to a mass-to-charge ratio <4.5 by a 3-6 keV electron beam. ^{140}Sm ions were charged-bred to a 34^{+} charge state. To select ions from REXTRAP and REXEBIS the ions are selected in an A/q separator with a resolution of A/q =1/150. The ions are then injected into the linear accelerator (REX-Linac) [34]. When the ions reach the REX-Linac they are first accelerated by a 4-rod RFQ up to 300A keV. Then an Interdigital H-type Structure (IHS) accelerates the ions up to a chosen energy between 0.8 and 1.2A MeV. The next accelerating step consist of three 7-gap resonators and one 9-gapIHS that can deliver a beam energy of up to 3.0A MeV [34].

3.2 Experimental setup

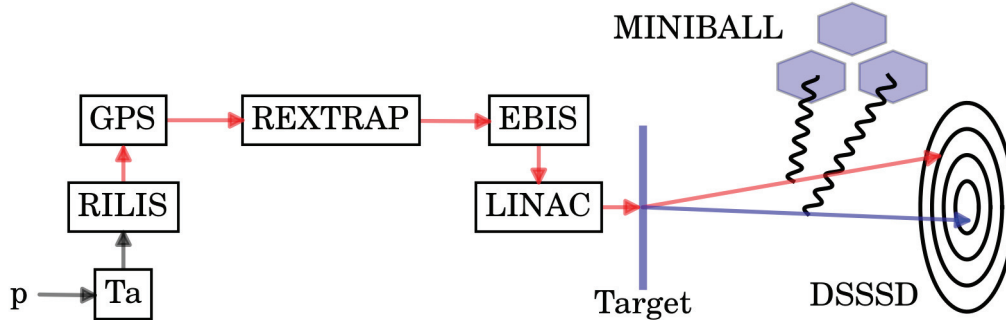The experimental setup used in the recent Coulomb excitation experiment of ^{140}Sm is illustrated in Fig. 3.2.

Figure 3.2: Radioactive ^{140}Sm, with intensity $2 \cdot 10^5$ pps and energy 2.85A MeV were produced at ISOLDE, from 1.4 GeV protons hitting a primary tantalum target. Ion selection was performed, using the General Purpose Separator (GPS) and stepwise Resonant Laser Ionization (RILIS). The ions were bunched, cooled and trapped in REXTRAP, charged-bred in EBIS and further accelerated by the REX-LINAC. Scattered ^{140}Sm and target ^{94}Mo particles were detected in a DSSSD, in coincidence with γ photons detected in MINIBALL.

The ^{140}Sm projectiles were scattered on a 2 mg/cm^2 thick ^{94}Mo target and γ photons from the de-exciting nuclei were detected in seven clusters of the MINIBALL HPGe array, presented in Fig. 3.3. Each of the MINIBALL clusters consists of three six-fold-segmented crystals [25]. The annular 1000 μm thick Double Sided Silicon Strip Detector (DSSSD), (see Fig. 3.4) was mounted inside the MINIBALL target chamber and used to detect the scattered beam and target nuclei. The DSSSD consists of four detecting quadrants coupled to four ADC modules. Each quadrant consists of 16 annular front strips with a strip pitch of 1.9 mm and 12 azimuthal back strips covering $3.5°$ each. In total the detectors cover an area of 5000 mm^2, with an active area of 93 % [39]. For the ^{140}Sm experiment the DSSSD was placed 25.2 cm from the target, hence the detector covered the angular range from 19.7 to 58.4 degrees in the laboratory frame. In this experiment, 2 front strips and 6 back sectors were not working.
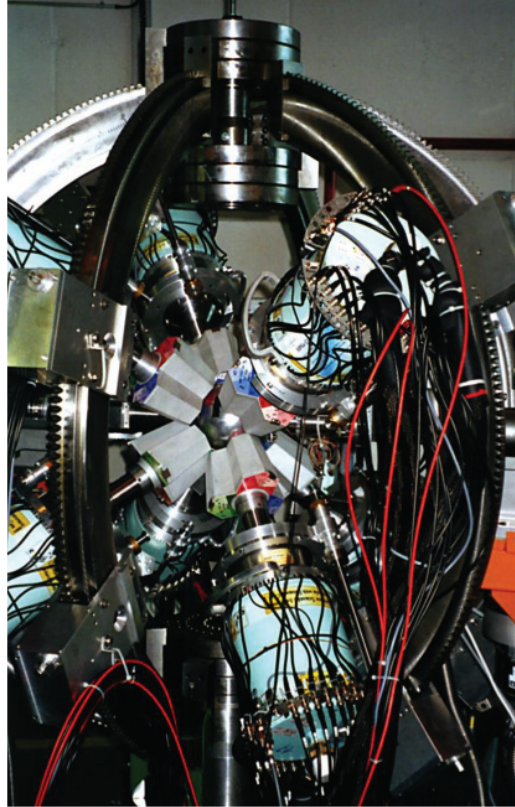
Figure 3.3: The γ photons from the de-exciting nuclei were detected in seven clusters of the MINIBALL HPGe array.

Figure 3.4: The annular Double Sided Silicon Strip Detector (DSSSD), mounted inside the MINIBALL target chamber for the ^{140}Sm Coulomb excitation experiment. The target wheel allows mounting of several targets in one experiment.

3.2.1 Data acquisition system

The signals from the six segments and the core of each MINIBALL crystal were read out by two Digital Gamma Finder (DGF) modules with four input channels each. The output from all DGF modules were then synchronized to provide a common start and stop of the data acquisition [25]. For each quadrant of the DSSSD, the 29 signals (16 from the front strips, 12 from the back strips and 1 for the total energy), were shaped, amplified and sent to an ADC. The signals from the DSSSD were used as event trigger and a 800 ns wide coincidence gate with the DGF was applied to collect γ-particle coincidences. In order to avoid collecting data during the EBIS breeding time, the EBIS timestamp was used to generate a window of 800 μs data collecting time followed by 800 μs without data taking. Another timestamp was sent from the RILIS to register if the laser was switched on or off. Finally the timestamp of each proton pulse was saved in the DGF.

3.3 Data analysis

3.3.1 Reaction kinematics

In the semi-classical approximation, the kinematics of the inelastic scattering is obtained from two-body kinematics and the projectile angle in the laboratory frame, θ_p^{lab} is related to the angle in the center-of-mass system, ν_p^{CM} in Eq. (3.1) [4]

$$\tan(\theta_p^{lab}) = \frac{\sin(\nu_p^{CM})}{\cos(\nu_p^{CM}) + \tau_p}, \tag{3.1}$$

where τ_p is given by Eq. (3.2)

$$\tau_p = \frac{m_p}{m_t} \cdot \sqrt{\frac{E_p}{E_p - \Delta E(1 + \frac{m_p}{m_t})}}. \tag{3.2}$$

Here, E_p is the particle energy and ΔE is the excitation energy due to Coulomb excitation. Similarly, the scattering angle of the target in the laboratory frame is obtained from Eq. (3.3)

$$\tan(\theta_t^{lab}) = \frac{\sin(\nu_t^{CM})}{\cos(\nu_t^{CM}) + \tau_t}, \tag{3.3}$$

where τ_t is given by Eq. (3.4).

$$\tau_t = \sqrt{\frac{E_p}{E_p - \Delta E(1 + \frac{m_p}{m_t})}} \qquad (3.4)$$

The energy of the scattered ^{140}Sm and ^{94}Mo as a function of scattering angle in the laboratory frame is shown in Fig. 3.5.
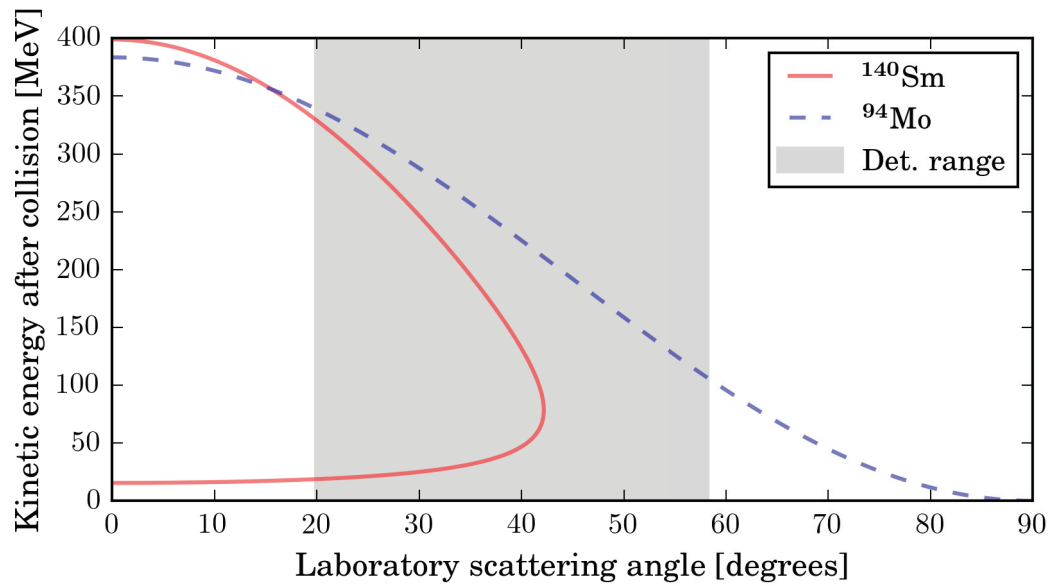
Figure 3.5: The energy of scattered ^{140}Sm and ^{94}Mo as a function of the scattering angle in the laboratory frame. The range covered by the DSSSD is marked in grey.

3.3.2   Doppler correction

Since the γ photons coming from the de-excitation process are emitted in flight they are shifted due to the Doppler effect. The energy detected in the laboratory frame, given in Eq. (2.19) [9], is related to the energy in the center of mass frame, E_{CM}, the velocity of the scattered particle relative to the speed of light, $\beta = v/c$ and the angle between the nucleus and the γ photon, α. The value of β for the particle, using a non-relativistic approximation, is given by Eq. (3.5).

$$\beta = \sqrt{\frac{2E_{particle}}{mc^2}}. \qquad (3.5)$$

Using the DSSSD it was possible to obtain a better angular resolution than energy resolution in the ^{140}Sm experiment, therefore the velocity of the particles was calculated from the average β value, using Eq. (3.6) [40]

$$\beta = \beta_{avg}\sqrt{1 - 4(A_t/A_p)\frac{\cos^2(\theta_t)}{(1 + A_t/A_p)^2}}. \tag{3.6}$$

The importance of the Doppler correction for the identification of the γ peaks is clearly seen in Fig. 3.6, where the shape of the $2^+ \rightarrow 0^+$ transition peak at 531 keV is shown before and after applying the Doppler correction for ^{140}Sm velocity.
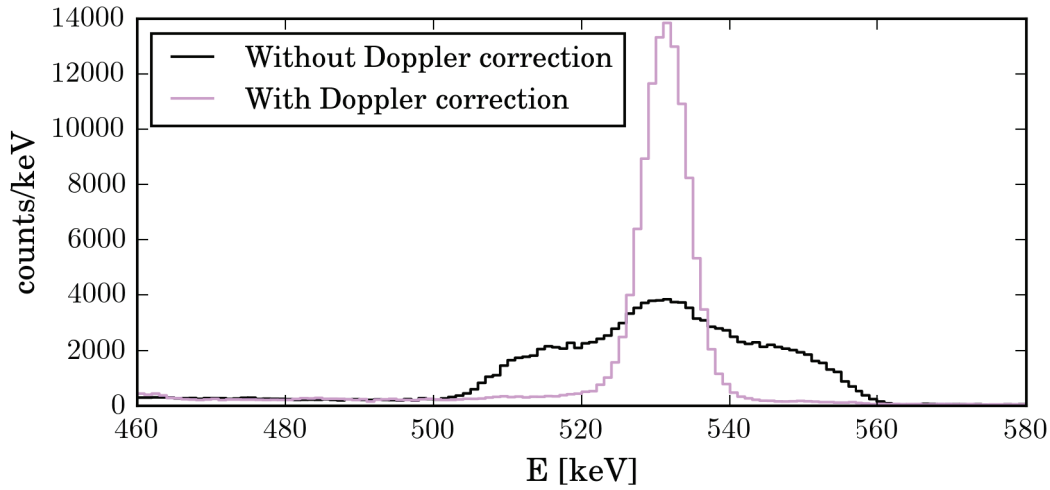
Figure 3.6: The γ spectra before and after applying Doppler correction for ^{140}Sm.

3.3.3 Data sorting

The data from the ^{140}Sm experiment was converted from a dedicated data format used at the ISOLDE facility to the *root* format files, using the `offl_med_run` [41] script, originally written by Oliver Niedermaier, at the Max-Planck Institute in Heidelberg. The next step of the data sorting was performed using programs written in $C + +$. The time gate for prompt particle-γ coincidences was applied on the root data. Events corresponding to the detection of ^{140}Sm projectiles and ^{94}Mo target nuclei were separated using cuts on the energy signal from the DSSSD, before the Doppler correction for ^{140}Sm and ^{94}Mo velocities were applied. Subtraction of random events was performed and events were further divided into different bins corresponding to different angular ranges.

3.3.4 Energy and efficiency calibration

Energy calibration of the MINIBALL detector was performed for each segment and each crystal core, using the γ rays from a ^{152}Eu-^{133}Ba source (see spectrum in Fig. 3.7). The γ lines used in ^{152}Eu are listed in Tab. 3.1 and in ^{133}Ba the line at 356.02 keV was used. Tab. 3.2 presents the resolution of the line at 1408 keV, after the calibration for each core.

Energy [keV]	Relative intensity
121.91	13620(160)
244.67	3590(60)
344.25	12750(90)
411.04	1070(10)
443.85	1480(20)
778.64	6190(80)
867.17	1990(40)
963.86	6920(90)
1111.92	6490(90)
1212.85	670(8)
1299.08	780(10)
1408.09	10000(30)

Table 3.1: Relative intensities from ^{152}Eu-^{133}Ba used for calibration of the MINIBALL detector

Core	FWHM [keV]	Core	FWHM [keV]	Core	FWHM [keV]
1	3.31	9	2.98	17	2.91
2	2.65	10	3.30	18	3.15
3	3.13	11	3.33	19	4.85
4	2.75	12	2.89	20	2.78
5	2.81	13	-	21	4.01
6	2.71	14	-	22	3.35
7	3.13	15	-	23	3.71
8	2.89	16	3.06	24	2.83

Table 3.2: Resolution of the line at 1408 keV after calibration of each MINIBALL crystal core.

Relative-efficiency curves were obtained from the fit of the intensities of the ^{152}Eu-^{133}Ba peaks to Eq. (2.27). The fit of the sum of all MINIBALL
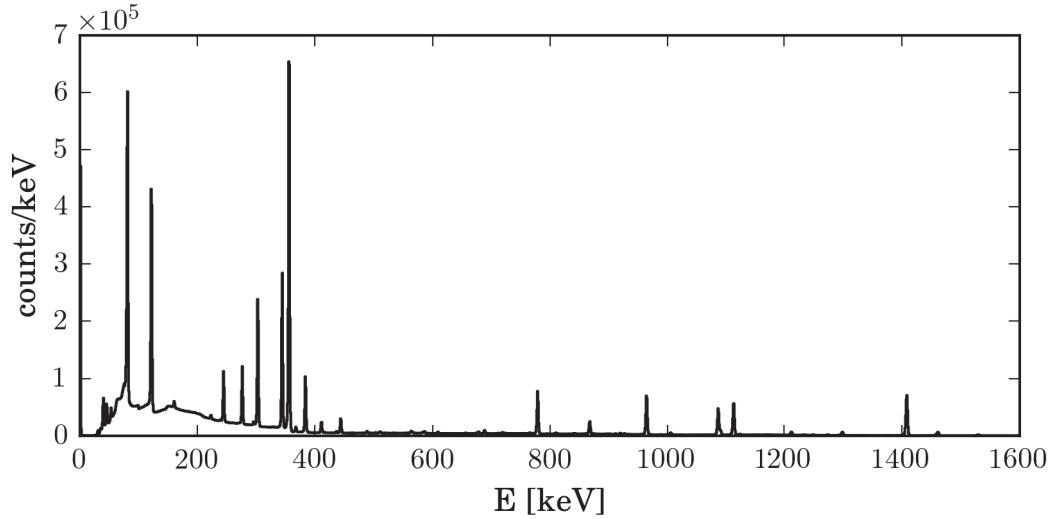
Figure 3.7: The γ spectrum from ^{152}Eu-^{133}Ba was used for calibration of the MINIBALL detector.

crystals is shown in Fig. 3.8. Calibration of the γ-ray detectors was performed in *addback mode*, meaning that γ photons hitting different crystals in the same cluster are summed into one γ ray [25], as well as without addback. It was found that application of the addback increased the efficiency by 8% at 500 keV and by 16% at 1000 keV. The addback mode was therefore used in the further analysis.

Figure 3.8: Relative-efficiency curve for the total MINIBALL spectrum.

For the DSSSD the calibration was performed by adjusting the energy of each strip that deviated from the trend presented in Fig. 3.5, with

a constant offset. A rough energy calibration was needed to distinguish between scattered ^{140}Sm and ^{94}Mo, while the exact energies were less important. The resolution of the s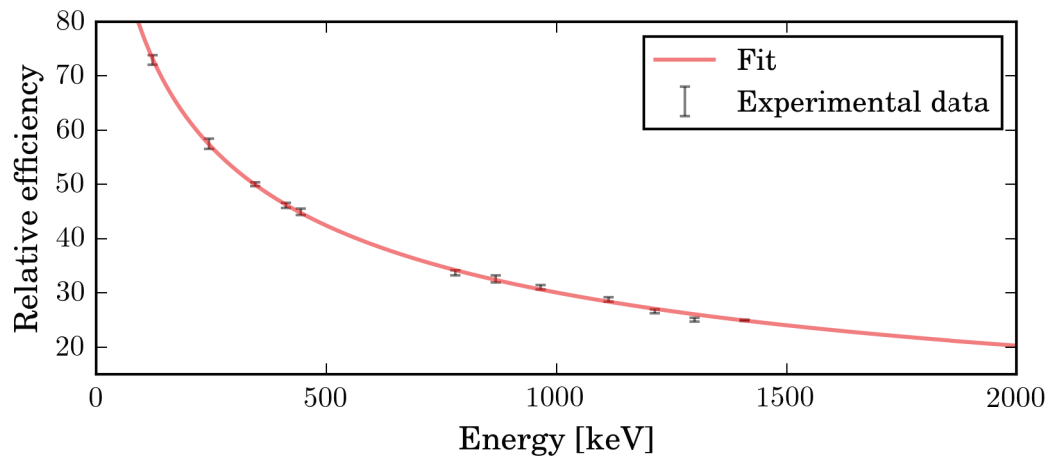pectra was improved by looking at each of the four DSSSD quadrants separately, as shown in Fig. 3.9. Here the particle energy spectrum measured in coincidence with γ rays detected in the MINIBALL array, as a function of scattering angle, for the four DSSSD quadrants are shown together with the cuts used to distinguish between detected projectile and target nuclei. For the innermost strips, where the separation was poor, the data were excluded from the analysis.
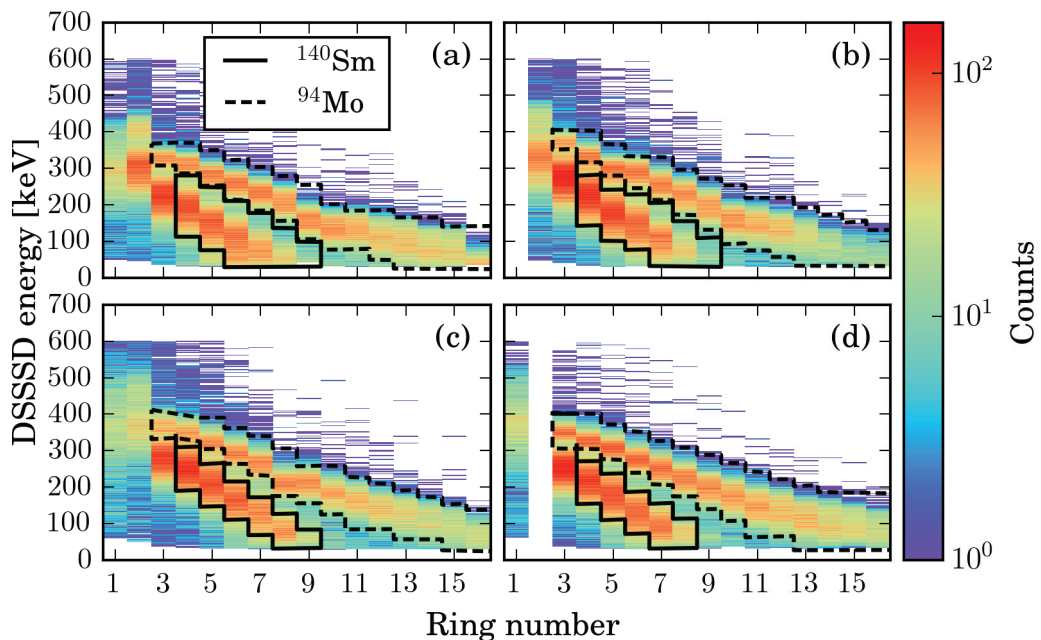

Figure 3.9: The particle energy spectrum measured in coincidence with γ rays detected in the MINIBALL array, as a function of scattering angle, for the four DSSSD quadrants together with the cuts used to distinguish between detected projectile and target nuclei. The ring number is counted from the center of the DSSSD.

3.3.5 Selection of prompt coincidences

The DSSSD was used as an event trigger, meaning that only the events with one or more γ-rays detected in coincidence with a particle detected in the DSSSD were collected. However, the hardware coincidence gate of about 1 μs was too wide to contain only prompt coincidence events, as seen in Fig. 2 in Paper 3, where the time difference between the DSSSD and the MINIBALL signals is shown. In order to collect sufficient statistics, the time gate for random coincidences, used later for background subtraction, was four times as wide as the gate for prompt coincidences.

Due to the kinematics of the ^{140}Sm $+^{94}$Mo reaction, most of the γ photons were expected to be detected not as γ-particle events but rather as γ-particle-particle coincidences with both the ^{140}Sm and the ^{94}Mo target nuclei. Hence, two particles should be detected in opposite quadrants of the DSSSD array. The time difference between two particles detected in prompt coincidence with the same γ photon, is shown in Fig. 3.10. The peak is shifted for coincidences between quadrant 0 and 2 compared to 1 and 3, meaning that slightly different time gates were needed for the two cases. The angle between the two detected particles was used to separate
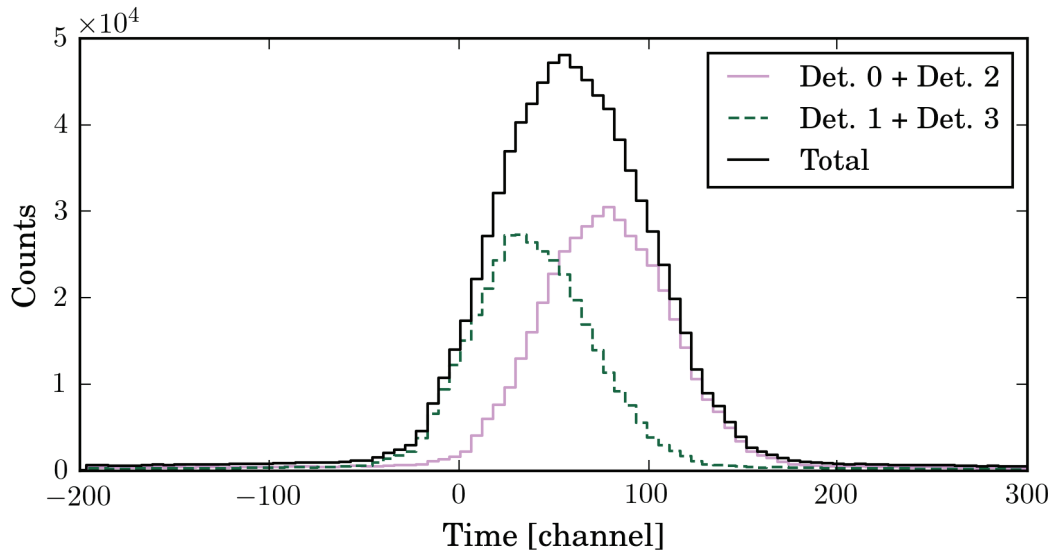
Figure 3.10: The time difference between two particles detected in prompt coincidence with the same γ photon. The peak is shifted for coincidences between Det. 0 + Det. 2 compared to Det. 1 + Det. 3.

real Sm-Mo-γ events from the random particle-particle-γ-events. Panel a) of Fig. 3.11 shows the ring number of the first detected particle against the ring number of the second detected particle in coincidence with the

same γ ray. All quadrants are in agreement with the theoretical locations of the coincidences, calculated using LISE++ [42] under the assumption of a circular symmetry with a well centered point-like beam. If the beam is centered with respect to the DSSSD, the intensity of the elastically scattered particles (random particle-γ events) as a function of ring number should follow the Rutherford cross section from Eq. (2.14) independent of the detector quadrant. The number of particles detected in random coincidence with a γ photon, divided by the integration of $1/sin^4(\theta/2)$ over each ring number, as a function of ring number (see panel b) in Fig. 3.11), is therefore expected to be constant for all quadrants. For the rings used in this analysis, the data were consistent with a well centered beam. The total number of the prompt particle-particle-γ coincidences, as a function of ring number is not straight forward to predict, since it includes the sum of detected ^{140}Sm and detected ^{94}Mo at each laboratory angle. However, as presented in panel c) in Fig. 3.11 the intensity distributions follows the same trend for all four quadrants, which further strengthen the assumption of a centered beam. Assuming a particle detection efficiency of 100%, all detected ^{94}Mo target nuclei should be in coincidence with detected ^{140}Sm projectiles. Taking into account the non active area of the DSSSD and the two non-working front strips, 87% of the prompt γ rays were expected to be in coincidence with two particles. In the current experiment, 76% of the prompt γ photons were in coincidence with two particles. The missing two-particle coincidences are due to the fact that 6 of the 48 back strips were not working.

The distribution of all detected particle-γ coincidences in the DSSSD is presented in Fig. 3.12. The missing front and back strips are visible through the variation in intensity. The innermost rings were very noisy and damaged due to high irradiation rate. These rings were excluded from the further analysis. The particle-particle-γ coincidence gate and the distribution of the 2nd particle, when the first particle was detected in ring 3 or 4, (see Fig. 3.13), were used for cleaning the γ-ray spectra. The figure presents a symmetric intensity distribution of the registered particles.
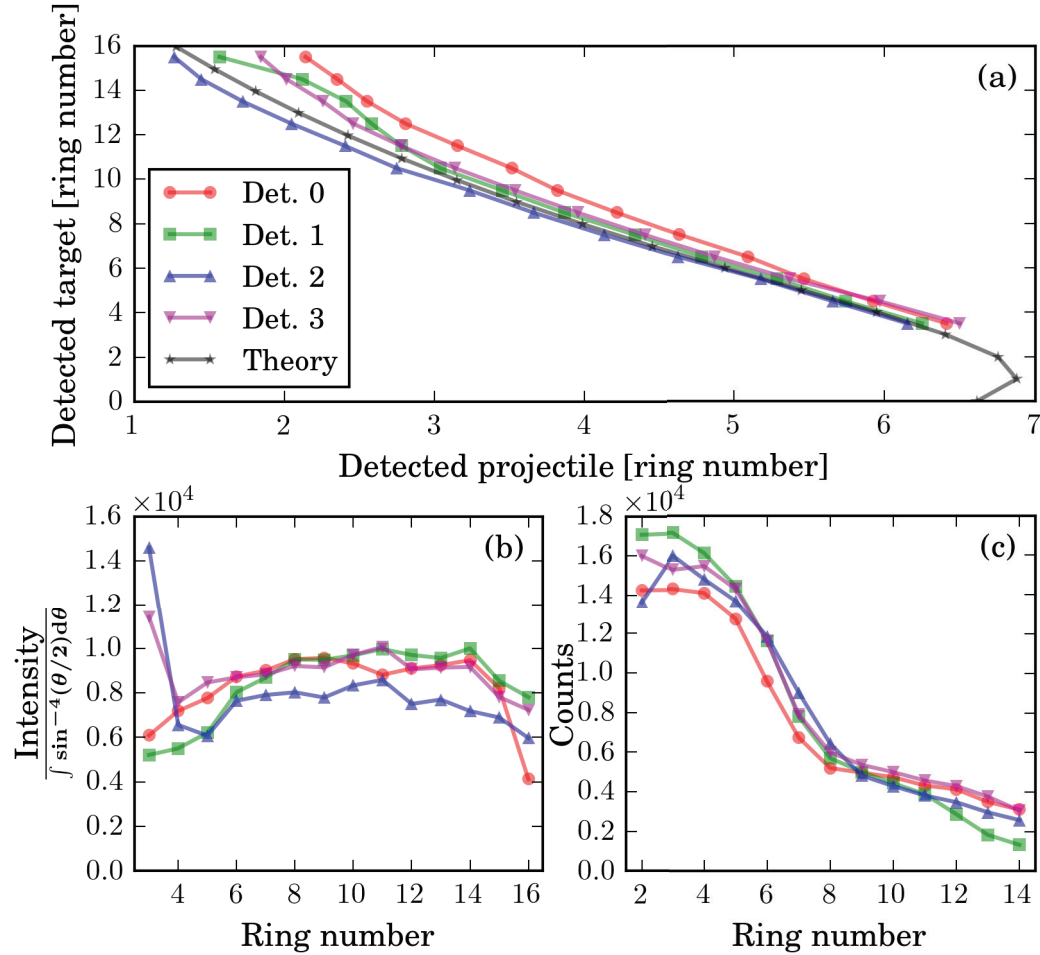
Figure 3.11: Tests performed to verify the centering of the beam. a): The ring number of the first detected particle against the ring number of the second detected particle in coincidence with the same γ photon. The different curves are for the different quadrants of the DSSSD detecting the target particle in coincidence with a projectile detection in the opposite quadrant. All quadrants are in agreement with the theoretical curve, calculated under the assumption of a circular symmetry with a well centered point-like beam. b): The number of the particles detected in random coincidence with γ photons, divided by the integration of the Rutherford cross section, as a function of ring number, is expected to be constant for all quadrants. c): The intensity of the prompt particle-particle-γ coincidences as a function of ring number. The plot shows only minor differences in the intensity distribution for the different quadrants, which strengthen the assumption of a centered beam.

Figure 3.12: Distribution of all particle-γ coincidences in the DSSSD. The innermost rings were excluded from the further analysis.

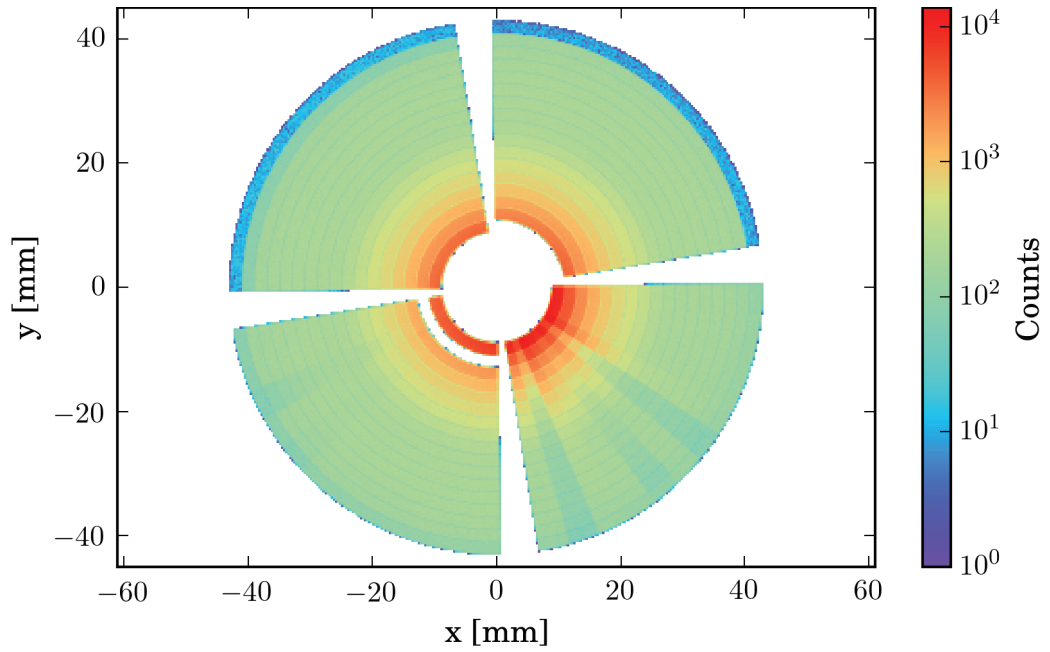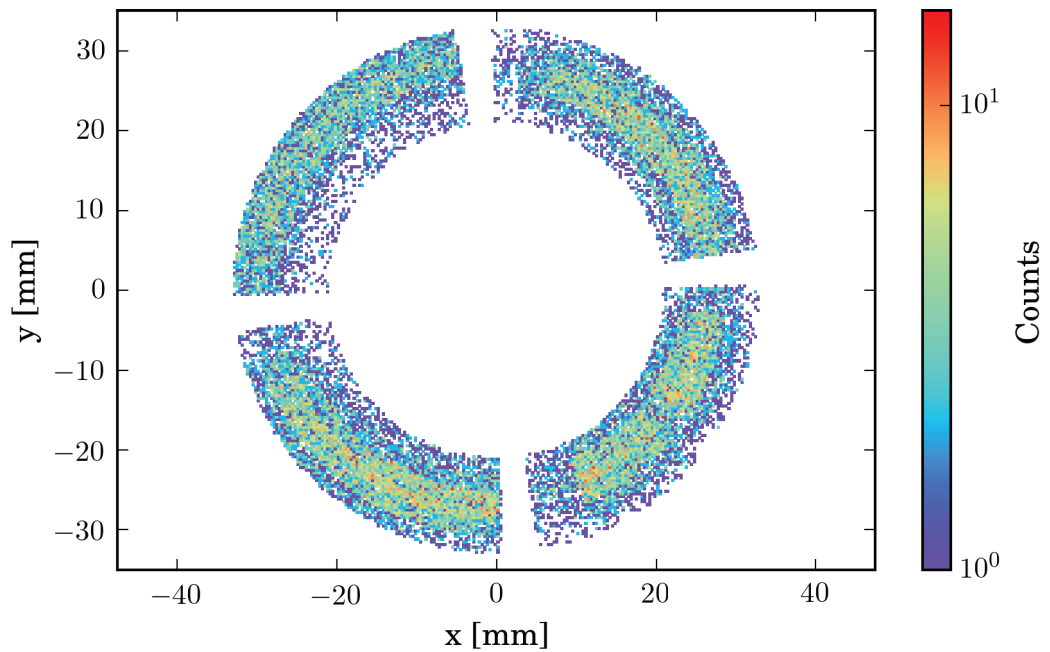Figure 3.13: The distribution of the 2nd particle, under the condition that the first particle was detected in ring 3 or 4.

3.3.6 DSSSD angular range binning

To increase the sensitivity on the quadrupole moment of the 2_1^+ state in ^{140}Sm, the data set was first divided into ten DSSSD angular ranges. Tab. II in Paper 3 presents the number of counts in the $2_1^+ \rightarrow 0_1^+$ transitions in ^{140}Sm and ^{94}Mo, for each angular range, selected outside the missing DSSSD strips, where it was possible to distinguish between projectile and recoil nuclei.

The angular dependence of the intensity of the $4_1^+ \rightarrow 2_1^+$ and $2_2^+ \rightarrow 2_1^+$ γ transitions could be obtained by dividing the spectra into five angular bins. In Tab. I in Paper 3, the number of counts from the transitions observed in ^{140}Sm and ^{94,95}Mo are presented for each angular bin. The Doppler corrected ^{140}Sm γ spectra corresponding to these five bins are shown in Fig. 7 in Paper 3 and the particle-particle coincidence gates for different scattering angles are listed in Tab. 3.3. The obtained angular

Target particle		Projectile particle	
Ring no.	θ_{CM} (deg)	Ring no.	θ_{CM} (deg)
3-4	112-125	5-7	90-146
5-7	95-112	4-7	80-146
8-10	82-95	3-5	70-100
11-13	71-82	2-4	60-90
14-16	63-71	1-4	50-90

Table 3.3: Coincidence gates on the kinematic to define Sm-Mo-γ coincidences, used in the ^{140}Sm Coulomb excitation analysis.

dependences of the γ yields for the $4_1^+ \rightarrow 2_1^+$ and the $2_2^+ \rightarrow 2_1^+$ transitions are presented in Fig. 3.14, where the intensities are normalized to the intensity of the $2_1^+ \rightarrow 0_1^+$ transition.
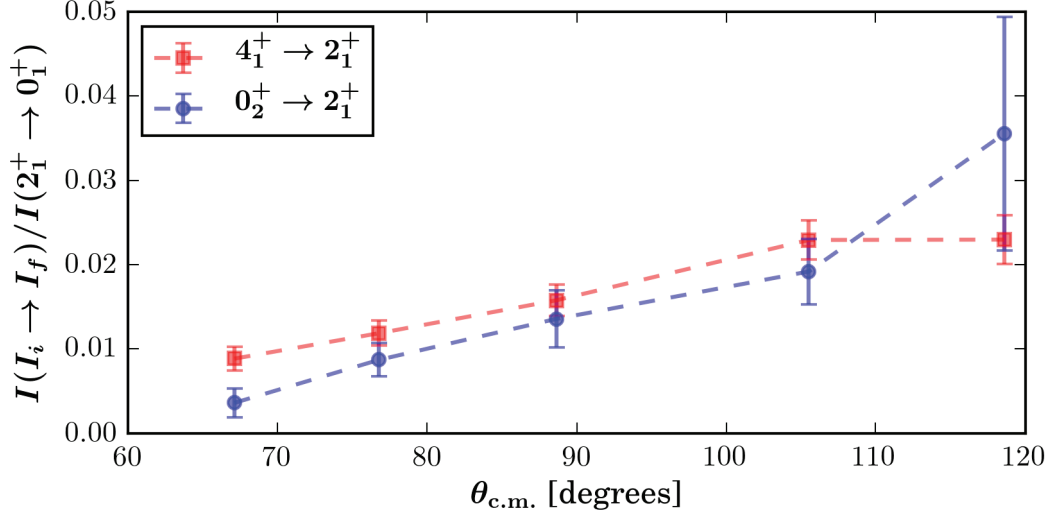
Figure 3.14: The intensities of the γ transitions from the 4_1^+ and 2_2^+ state (normalized to the $2_1^+ \rightarrow 0_1^+$ transition) increase with increasing scattering angle.

3.3.7 The γ-ray spectra

The γ-ray spectra collected with prompt and random particle-γ coincidences condition, Doppler corrected for ^{140}Sm velocity are presented in Fig. 3.15. The peaks appearing in the prompt spectra at 460, 531 and 715 keV originate from Coulomb excitation of ^{140}Sm and the broad line at 871 keV is associated with Coulomb excitation of ^{94}Mo. In the random coincidence spectrum the 511 keV γ line is clearly visible. The final background subtracted γ spectra, Doppler corrected for ^{140}Sm and ^{94}Mo velocities, are presented in Fig. 4 and Fig. 5 in Paper 3, respectively. The γ rays at energies 459, 531 and 715 keV are visible in the spectrum Doppler corrected for the ^{140}Sm projectile velocity. The γ lines at 871 keV ($2_1^+ \rightarrow 0_1^+$ transition in ^{94}Mo) and 204 keV ($3/2^+ \rightarrow 5/2^+$ transition in ^{95}Mo) are observed in the γ spectrum Doppler corrected for the target-like recoil velocity.

Figure 3.15: Prompt and random γ-particle coincidence spectra, Doppler corrected for the projectile velocity. Lines seen in the prompt spectra at 460, 531 and 715 keV energies originate from Coulomb excitation of ^{140}Sm and the line at 871 keV is from Coulomb excitation of ^{94}Mo.
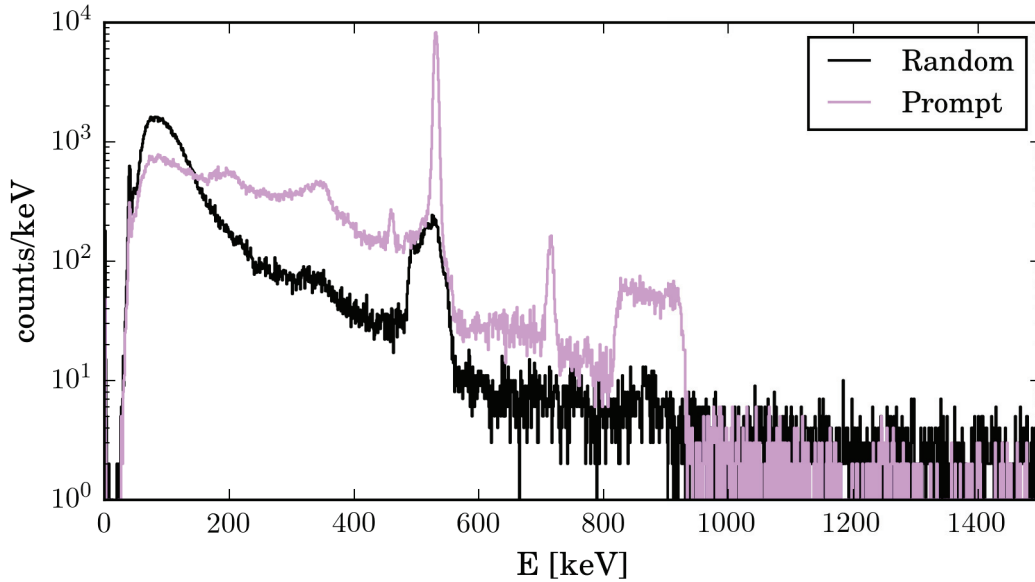
3.3.8 Contamination

Depending on the nucleus of interest, the beam is usually produced as a cocktail of different elements and isotopes. As a consequence, the beam purity can be affected by some isobaric contamination. At the CERN-ISOLDE facility the laser switched ON and OFF method is used for measuring the beam of interest and the possible contamination ratio by comparing the γ spectra collected during both periods. Fig. 6 in Paper 3 presents the spectra acquired in laser ON and laser OFF modes. The laser OFF spectrum shows some surface ionized ^{140}Sm and no indication of any beam contamination.

The 0.8% upper limit of ^{140}Nd beam contamination was determined from the intensity of the 773 keV peak corresponding to the $2_1^+ \rightarrow 0_1^+$ transition in ^{140}Nd. This line was observed in the γ spectrum Doppler corrected for the projectile nuclei velocity (marked with an arrow in Fig. 4 in Paper 3). This insignificant contamination was not taken into account in the further Coulomb excitation data analysis.

The observation of a transition at 204 keV in the spectrum Doppler corrected for the target recoils velocity, suggests the presence of ^{95}Mo in the target foil. The number of ^{95}Mo atoms, N_{95}, relative to the number of

^{94}Mo atoms, N_{94}, in the target foil can be found as:

$$\frac{N_{95}}{N_{94}} = \frac{Y_{95}}{Y_{94}} \frac{\epsilon_{95}}{\epsilon_{94}} \frac{\sigma_{94}}{\sigma_{95}} \qquad (3.7)$$

where Y_A and ϵ_A are the respective γ-ray yields and efficiencies for the $2_1^+ \rightarrow 0_1^+$ transition in ^{94}Mo and $3/2^+ \rightarrow 5/2^+$ transition in ^{95}Mo. The cross sections, σ_A, for the populations of the states were calculated from the known reduced matrix elements. In this way a 4.4(11)% admixture of ^{95}Mo is found, which is in good agreement with the value of 5(2)% that was found in another Coulomb excitation experiment using the same target foil [43].

Towards the end of the Coulomb excitation experiment, the data was collected with the beam turned off, with the purpose of collecting γ-ray spectra dominated by lines originating from β decay to the daughter nuclei. For this purpose, a thick copper target was first irradiated with the ^{140}Sm beam prior to the β decay study. Fig. 3.16 shows the beam-off spectrum with identified γ lines and no indication of a beam contaminant.
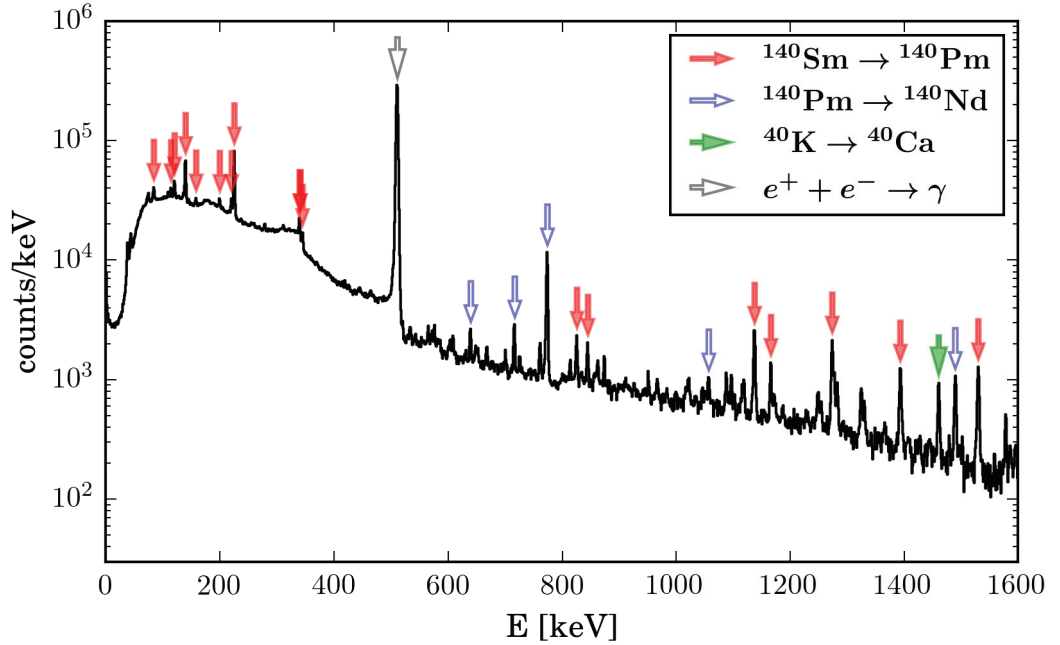

Figure 3.16: The γ spectrum obtained in the beam turned off mode. The γ lines from the β decay to the daughter nuclei are visible. γ transitions identified in the measurement are marked.

3.4 GOSIA and GOSIA2 analysis

The data collected in the Coulomb excitation of ^{140}Sm experiment was analyzed using the GOSIA [20] and GOSIA2 coupled channel codes, according to the iterative procedure described in detail in Paper 3.
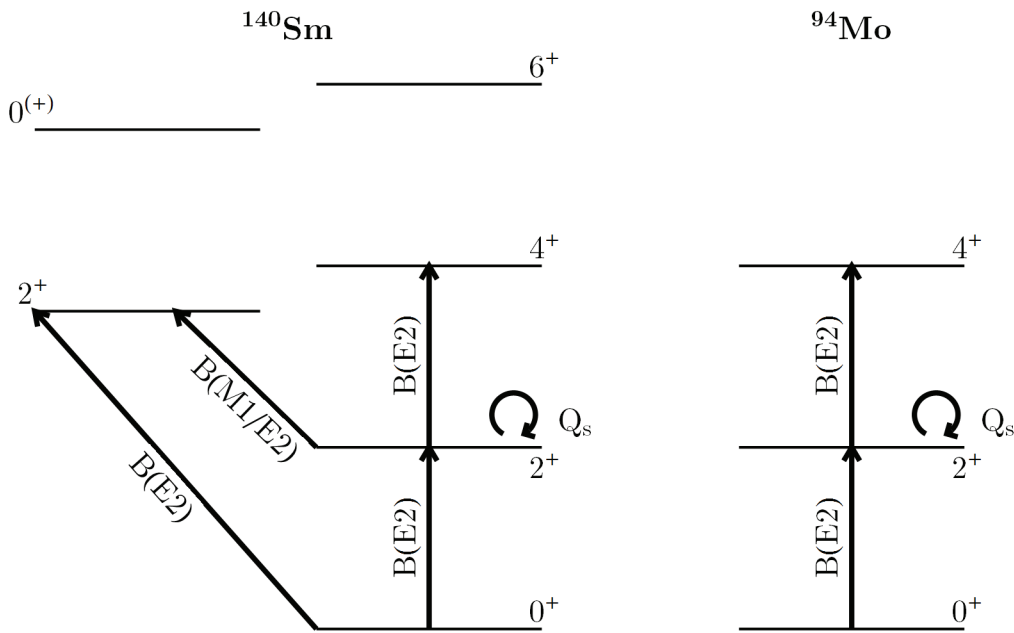
Figure 3.17: Level scheme for ^{140}Sm and ^{94}Mo taken into account in the recent Coulomb excitation analysis using the normalization to target excitation approach.

In order to reproduce the observed γ-ray intensities in the χ^2 function minimization routine, the GOSIA code fits the set of matrix elements to the spectroscopic data points. The program calculates the yields and compares them with the experimental ones taking into account the geometry and efficiency of both particle and γ-detection systems. The analysis procedure consists of integration over the scattering particle angular and energy ranges, minimization of the χ^2 function and calculation of the diagonal and correlated uncertainties for the set of extracted reduced transitional and diagonal matrix elements.

To convert the measured γ-ray intensities into the absolute excitation cross sections, single-particle events can be used to normalize to the Rutherford cross-section. This, however, requires a precise knowledge of the particle detector efficiency, dead time and the beam intensity, which may be limited in radioactive ion beam experiments. In the multistep

Coulomb excitation where the lifetime of one or more excited states are known, this problem can be overcome by normalizing the cross-section to the lifetime, in the standard GOSIA analysis. When little is known about the structure and lifetimes in the nucleus of interest, this approach doesn't provide the trustworthy results. Therefore a different Coulomb-excitation cross-section normalization must be applied. The GOSIA2 code was developed to allow for analysis of simultaneous projectile and target nuclei excitation.

Two approaches were used in the data analysis for the current Coulomb excitation ^{140}Sm experiment. Since the low-spin structure of ^{140}Sm was initially unknown, the first approach was based on the normalization to the target excitation method. The second one was based on the lifetime of the 2_1^+ state normalization, measured during the time of the Coulomb excitation analysis, in an independent RDDS experiment [44]. The detailed description of both analysis approaches are presented in Paper 3.

Angular ranges are defined in GOSIA either from detected projectile or detected target nuclei in the laboratory system. In the main part of the ^{140}Sm analysis, angles were defined in the laboratory system of the ^{140}Sm projectile. However, since coincidences between detected projectile and target particles were used, the consistency in yield calculation was confirmed by constructing the GOSIA input file with data sets corresponding to the angular ranges of ^{94}Mo target nuclei, defined in the laboratory frame.

In the GOSIA input file, the MINIBALL array was defined as 21 detectors at the positions given in Tab. 3.4, with relative efficiency taken from Fig. 3.8. The integration of yields was performed for angular and energy ranges of the scattered particles. For this purpose, 50 integration points were declared in both integration grids. The grids were defined with 18 equidistant angular grid point and 19 grid points in energy. Further, the energy loss in the target was calculated using SRIM code [45] and the electron conversion coefficients were obtained from Ref. [46]. For details on the GOSIA minimization input file, see Appendix A.

Fig. 3.18 shows the χ^2 as a function of the $\langle 0_1^+||E2||2_1^+ \rangle$ and $\langle 2_1^+||E2||2_1^+ \rangle$ matrix elements in ^{140}Sm from the first step in the GOSIA-GOSIA2 iteration. In this first approximation step of the data analysis, where only low scattering angles were used, the minimum is not well established. The next step of the data analysis was formed by including higher scattering angles, $\langle 2_1^+||E2||4_1^+ \rangle$, $\langle 2_1^+||E2||2_2^+ \rangle$, $\langle 0_1^+||E2||2_2^+ \rangle$, $\langle 2_1^+||M1||2_2^+ \rangle$ matrix elements and the experimental γ yield for the $4_1^+ \rightarrow 2_1^+$ and $2_2^+ \rightarrow 2_1^+$ transitions in ^{140}Sm. In this step the sensitivity for the $\langle 2_1^+||E2||2_1^+ \rangle$

Table 3.4: MINIBALL positions.

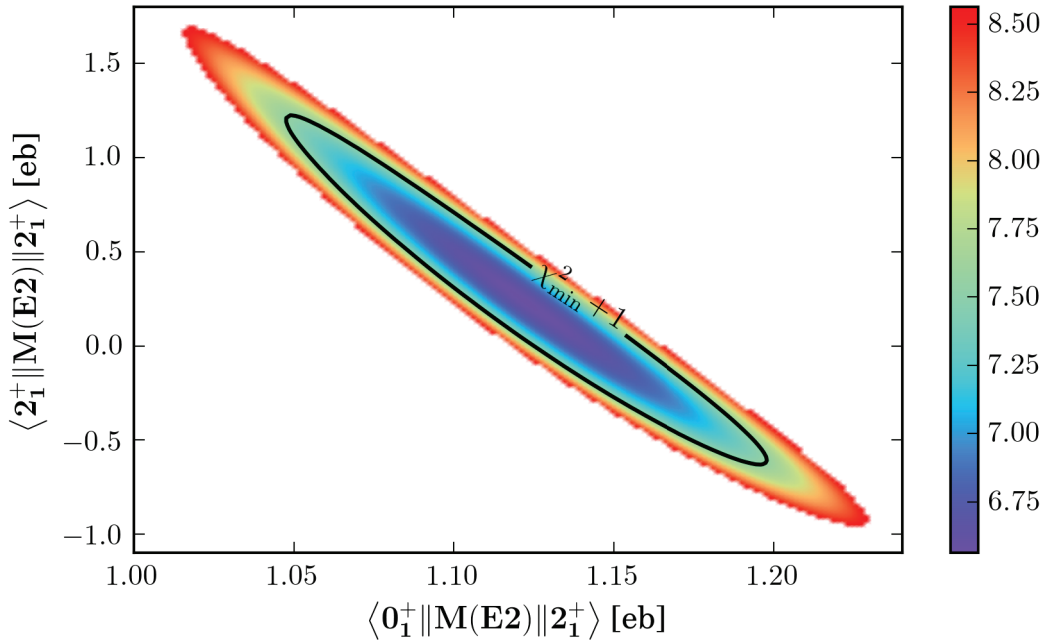| θ [deg]	ϕ [deg]	θ [deg]	ϕ [deg]
108.5	133.7	137.9	29.4
126.6	157.0	42.4	242.0
134.0	122.2	67.5	228.5
60.1	58.9	49.0	204.6
71.4	31.6	123.5	339.9
44.1	30.4	132.1	307.4
65.7	117.7	106.4	316.8
38.5	120.0	43.2	341.0
57.2	147.4	69.3	330.9
111.2	36.8	52.6	306.0
126.2	63.1		

Figure 3.18: The χ^2 as a function of matrix element $\langle 0_1^+||E2||2_1^+ \rangle$ and $\langle 2_1^+||E2||2_1^+ \rangle$ from the first step in the GOSIA-GOSIA2 iteration procedure. When only low scattering angles were used, the minima is poorly localized.

matrix element was significantly increased, as seen in the final χ^2 surface, presented in Fig. 9 in Paper 3, where the error bars on $\langle 2_1^+||E2||2_1^+\rangle$ are about a factor of 3 lower compared to the first approximation result in Fig. 3.18 .

The set of matrix elements to describe the structure of ^{140}Sm, $B(E2; I_i \to I_f)$ and $Q_s(2_1^+)$, obtained in the course of normalization to the ^{94}Mo target excitation and the lifetime analysis are presented in Paper 3, in Tab. III and Tab. IV respectively. From the slightly smaller value of the $B(E2; 2_1^+ \to 0_2^+)$ obtained from the lifetime measurement compared to the normalization to target excitation approach, some systematic errors in either of or in both of RDDS measurement and the Coulomb excitation experiment are indicated. However, the strengths of the transitions populating the 2_1^+ state remain within the errorbars.

A sensitivity test of the $\langle 0_1^+||E2||2_1^+\rangle$ yield to the quadrupole moment was performed, using the GOSIA code to calculate the $2_1^+ \to 0^+$ yield for different scattering angles, assuming the same $\langle 0_1^+||E2||2_1^+\rangle$ matrix element but different values of $\langle 2_1^+||E2||2_1^+\rangle$ diagonal matrix element. Fig. 3.19 shows calculated yield as a function of ^{140}Sm scattering angle in the laboratory system, for Q_s within the error band obtained in the GOSIA analysis. The sensitivity increases with increased scattering angle.
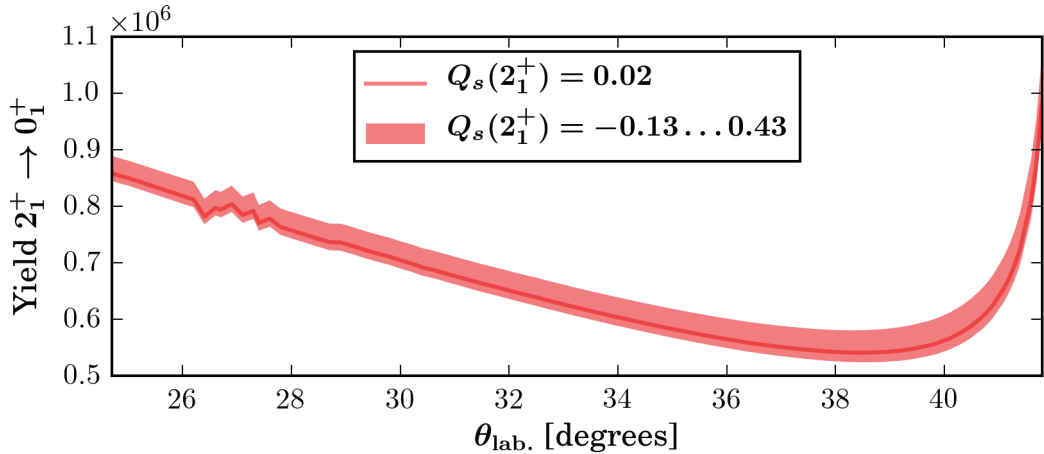
Figure 3.19: The calculated yield as a function of ^{140}Sm scattering angle in the laboratory system for Q_s within the errorband obtained in the GOSIA analysis. The sensitivity increases with increased scattering angle.

The spin of the state at 990 keV has recently been assigned as 2^+ in the dedicated angular correlation experiment performed at the Heavy Ion Laboratory, Warsaw. The full analysis, performed using the old spin assignment (0^+) resulted in enormous $B(E2; (0_2^+) \to 2_1^+)$>200 W.u. values

for both, target excitation and lifetime normalization analysis methods. After a careful revision of the applied approaches, the only possible explanation of the obtained results was the wrong spin assignment. The detailed description of the angular correlation experiment and its results are presented in Chapter 4.

3.5 Theoretical calculations

The experimental results obtained in this analysis are compared to theoretical calculations in the triaxial rotor and the γ soft model in Paper 3. The interacting boson approximation (IBA) placed ^{140}Sm in the transitional region between the spherical vibration and the triaxially soft rotational limit. At the critical point in this transition, the potential is approximately a five-dimensional infinite well, leading to analytic expressions of the wave functions in the E(5) symmetry critical point. As discussed in Paper 3, ^{140}Sm shows many features consistent with E(5) symmetry. The experimental findings are well reproduced, both by shell model calculations performed in collaboration with *IPHC, CNRS, UMR7178, Strasbourg, France* and by mean-field based calculations performed in collaboration with *CEA, DAM, DIF Arpajon, France*, suggesting a weak quadrupole deformation with maximum triaxiality and significant γ softness. For more details, see the discussion in Paper 3.

Chapter 4

^{140}Sm angular correlation experiment

For a proper interpretation of the Coulomb excitation analysis results, correct information regarding spin and parity of the excited states are crucial. In the recent Coulomb excitation analysis of ^{140}Sm, described in Chapter 3, the (0_2^+) assignment [31] of the state at 990 keV excitation energy resulted in an enormous $B(E2; 0_2^+ \rightarrow 2_1^+)$ value (> 200 W.u.) This problem indicated that the spin assignment couldn't be correct, and was therefore investigated in a dedicated β-decay experiment performed at the Heavy Ion Laboratory, University of Warsaw, Poland. The $\gamma - \gamma$ angular correlation data analysis presented in Paper 1 and Paper 2 resulted in a reassignment of the excited states at 990 keV and 1599 keV excitation energy in ^{140}Sm. In this chapter the experimental setup is described in Section 4.1 and the details of the data analysis are presented in Section 4.2.

4.1   Experimental setup

Excited states in ^{140}Sm were populated in β^+ and EC-decay from ^{140}Eu$\rightarrow$ ^{140}Sm and ^{140}Gd$\rightarrow$ ^{140}Eu $\rightarrow$^{140}Sm, at the Heavy Ion Laboratory in Warsaw. The ^{140}Eu ($T_{1/2} = 1.5$ s) and ^{140}Gd ($T_{1/2} = 15.8$ s) isotopes were produced in the ^{112}Cd(^{32}S,p3n)^{140}Eu and ^{112}Cd(^{32}S,4n)^{140}Gd reaction at 155 MeV incident beam energy. The self-supporting target consisting of 3.6 mg/cm^2 ^{112}Cd was used, and a 5 mg/cm^2 thick Au stopper foil was placed behind the target.

With many possible reaction channels opened and the following β decay of the produced nuclei, the γ spectrum becomes complex. Prior to the experiment, to get an overview of which γ lines were to be

expected at certain energies, simulations of γ spectra were performed using MATLAB [47] code (see Fig. 4.1). Cross sections were calculated using the COMPA code [48], for the reaction channels producing ^{139}Eu, ^{139}Sm, ^{140}Gd, ^{140}Eu, ^{140}Sm, ^{141}Gd and ^{141}Eu. Relative γ intensities and halflifes of the reaction products and the daughter nuclei were taken from tabulated values [49]. Furthermore, a gaussian peak shape with FWHM equal to 2.4 keV was assumed. The strong peak corresponding to the $2_1^+ \rightarrow 0_1^+$ transition in ^{140}Sm seen at 531 keV was of particular interest for this experiment, since it served as the gate condition to obtain $\gamma - \gamma$ coincidence data from the experimental data. In this experiment, the γ lines at 460, 1068 and 1097 keV (see Fig. 3.1) in coincidence with 531 keV were investigated. It was seen from the simulation that no other strong γ line would overlap with the 531 keV transition, hence gating on this line would provide a clean coincidence spectrum.
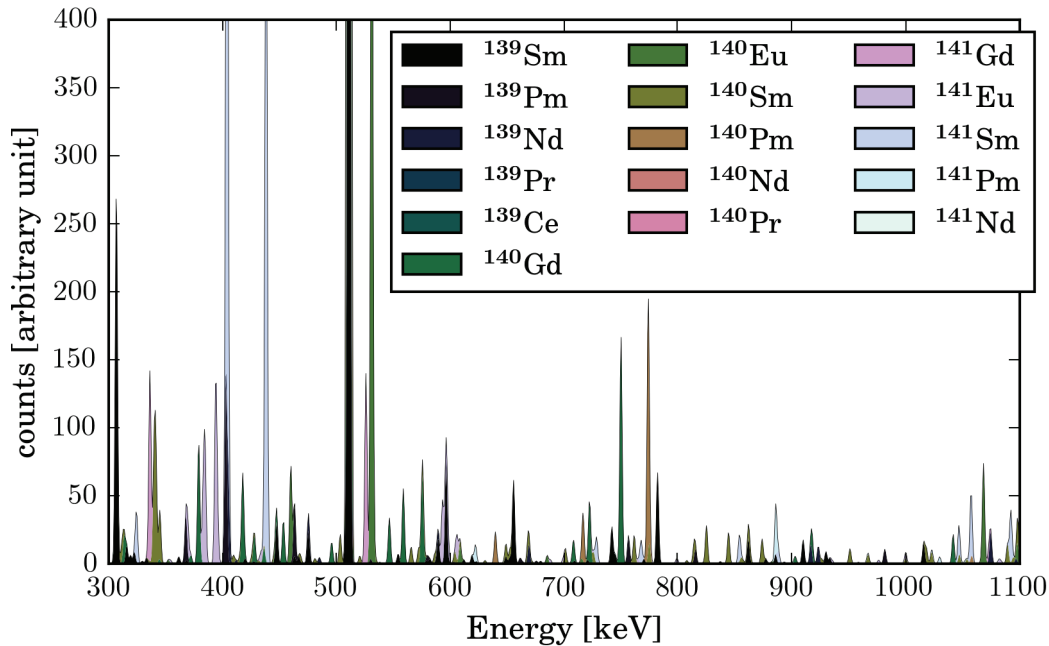
Figure 4.1: Simulated γ spectra for the ^{112}Cd+^{32}S reaction at 155 MeV. The strong peak corresponding to the $2_1^+ \rightarrow 0_1^+$ transition in ^{140}Sm seen at 531 keV was of particular interest for this experiment.

The macro-structure of the beam delivered from the U200P cyclotron allowed to produce the ions in periods of 2 ms followed by 4 ms off-beam time. By measuring the γ radiation during the off-beam periods, the prompt radiation was suppressed. The γ photons following the β decay were detected in the EAGLE array [50], seen in Fig. 4.2, consisting of

12 high-purity germanium detectors in anti-Compton shields, placed at the positions given in Tab. 4.1. The relative angle between two detectors are given in Tab. 4.2. This geometry gives 11 detector pairs at $42°$, 20 pairs at $70°$, 20 pairs at $110°$, 10 pairs at $138°$ and 5 pairs at $180°$.

Figure 4.2: The EAGLE array with 12 HPGe detectors.

The signals from the EAGLE array were processed by the analog electronics using amplifiers and constant fraction discriminators. In this experiment, the data taking was mainly triggerd on $\gamma - \gamma$ coincidences, but the additional down-scaled single spectra, needed for the calibration were collected.

Detector	ϕ [deg]	θ [deg]	Distance from source [mm]	FWHM [keV]	ϵ_{531keV}	Q_2	Q_4
1	0	101	188	1.74	1.000(15)	0.9945	0.9818
2	108	37	186	2.33	1.663(19)	0.9944	0.9815
3	72	101	231	2.02	0.503(13)	0.9963	0.9876
4	288	143	209	2.48	1.531(24)	0.9955	0.9851
5	0	143	211	1.85	1.018(24)	0.9956	0.9853
6	72	143	219	2.22	0.793(24)	0.9959	0.9863
7	324	37	216	2.99	0.986(9)	0.9958	0.9860
8	252	37	221	2.01	0.882(14)	0.9960	0.9866
10	180	79	191	2.33	1.223(31)	0.9947	0.9824
11	144	143	196	2.05	1.659(38)	0.9949	0.9832
13	108	79	201	2.12	0.879(18)	0.9952	0.9840
14	180	37	201	1.90	0.868(10)	0.9952	0.9840

Table 4.1: Position, width, efficiency (relative to detector 1) and solid angle corrections factors of the germanium detectors in the EAGLE array, used in the experiment.

Ge	1	2	3	4	5	6	7	8	10	11	13
1	-	-	-	-	-	-	-	-	-	-	-
2	109.6	-	-	-	-	-	-	-	-	-	-
3	70.5	71.0	-	-	-	-	-	-	-	-	-
4	70.4	180.0	109.0	-	-	-	-	-	-	-	-
5	42.0	138.6	70.4	41.4	-	-	-	-	-	-	-
6	70.4	110.2	42.0	69.8	41.4	-	-	-	-	-	-
7	71.0	69.8	109.6	110.2	110.2	138.6	-	-	-	-	-
8	109.6	69.8	138.0	110.2	138.6	180.0	41.4	-	-	-	-
10	180.0	70.4	109.5	109.6	138.0	109.6	109.0	70.4	-	-	-
11	109.0	110.2	70.4	69.8	69.8	41.4	180.0	138.6	71.0	-	-
13	109.5	42.0	42.0	138.0	109.6	71.0	109.0	109.0	70.5	71.0	-
14	138.0	41.4	109.6	138.6	180.0	138.6	69.8	41.4	42.0	110.2	70.2

Table 4.2: Relative angle (in deg.) between the germanium detectors, used in the experiment.

4.2   Data analysis

4.2.1   Data sorting and Calibration

The data from 87 hours of beam time, were sorted using the `mult_sorting` program developed at HIL, Warsaw. A time gate was applied to select only the off-beam data. Energy calibration was performed using the γ intensities from a ^{152}Eu source. Each HPGe detector was calibrated by applying a 3rd order polynomial fit, resulting in a chi square per degree of freedom, χ^2/N_{dof} between 7.7 and 35.9 for different detectors. With a linear fit, χ^2/N_{dof} between 1200 and 2889 were obtained. The quality of the fit for one of the detectors (see in Fig. 4.3), clearly shows a non-linear energy dependence. In Tab. 4.1 the FWHM of the 531 keV peak
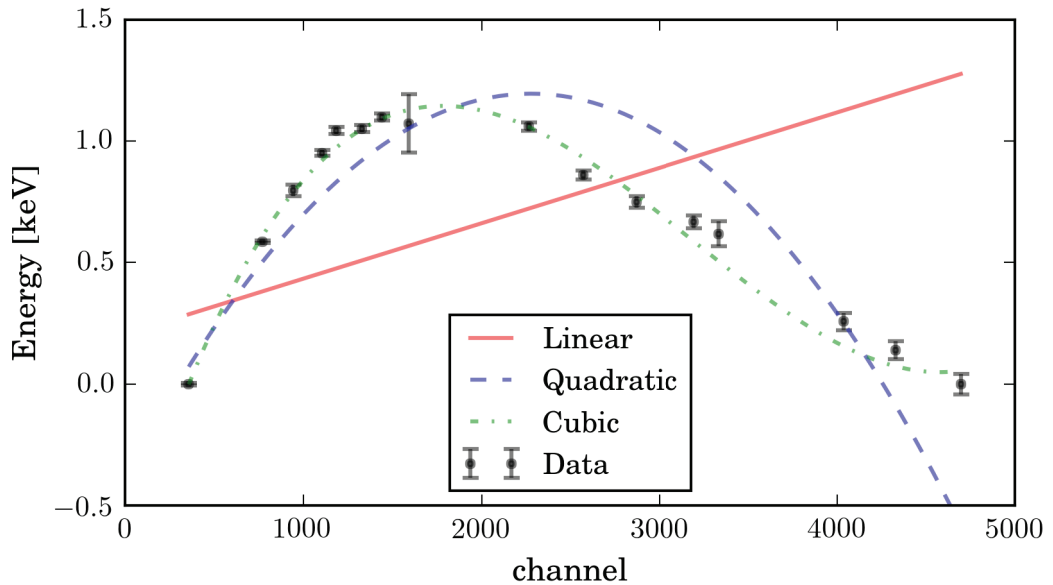
Figure 4.3: The figure shows the quality of a linear, a quadratic and a cubic calibration of the Ge detectors. The energy, subtracted by a straight line through the first and last point as a function of channel, clearly shows a non-linear energy dependence.

after calibration are listed for one data file.

A drift of the calibration parameters was found as a function of time and taken into account by adjusting the gain and offset for each data file. This was done using the intense peaks at 531 keV from ^{140}Eu and 404 keV from ^{141}Sm, taken from the single spectra. The drift in time of the channel position of the 531 keV line is shown in Fig. 4.4.

Figure 4.4: From the channel position of the peak at 531 keV as a function of run number it is seen that the gain and offset drift during the time of the experiment.

4.2.2 Efficiency of γ-ray detectors
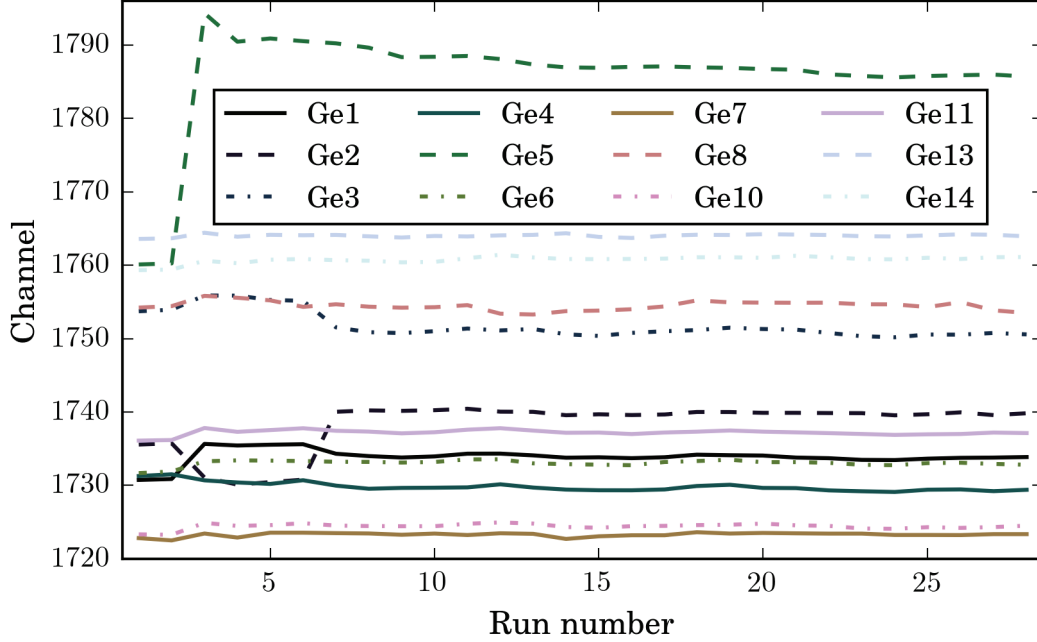
Relative efficiency curves were obtained for each HPGe detector using the ^{152}Eu source. However, the center of the source was slightly different from the center of the beam, therefore the fitted efficiency curves had to be corrected for this effect to give the proper efficiency for the in-beam runs. For this purpose, so-called *internal calibration*, the intensities of the 531 and 404 keV lines were measured in the single spectra. The difference between the calibration obtained using the ^{152}Eu source and using the intensity of the 531 keV line is shown in Fig. 4.5.

To compare the efficiency of different detectors, the efficiency curves were normalized to one arbitrary chosen detector (Ge1). It is seen in Fig. 4.6 that efficiency as a function of energy decreases faster for three of the detectors compared to the others. The efficiency of each detector at 531 keV relative to Ge1 is presented in Tab. 4.1. The efficiency of a detector pair with coincident γ detection is further given by the product of the efficiency of two detectors according to Eq. (4.1)

$$\epsilon_{avg} = \frac{\epsilon_{Ge1}(E_{g1}) \cdot \epsilon_{Ge2}(E_{g2}) + \epsilon_{Ge1}(E_{g2}) \cdot \epsilon_{Ge2}(E_{g1})}{2}. \qquad (4.1)$$
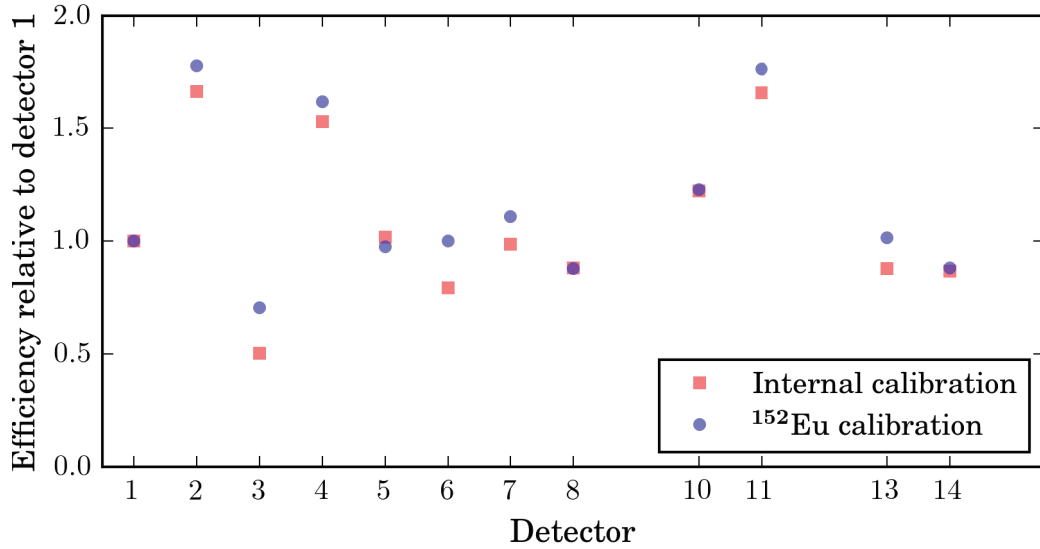
Figure 4.5: The difference between the calibration obtained using the ^{152}Eu source and using the intensity of the 531 keV line.
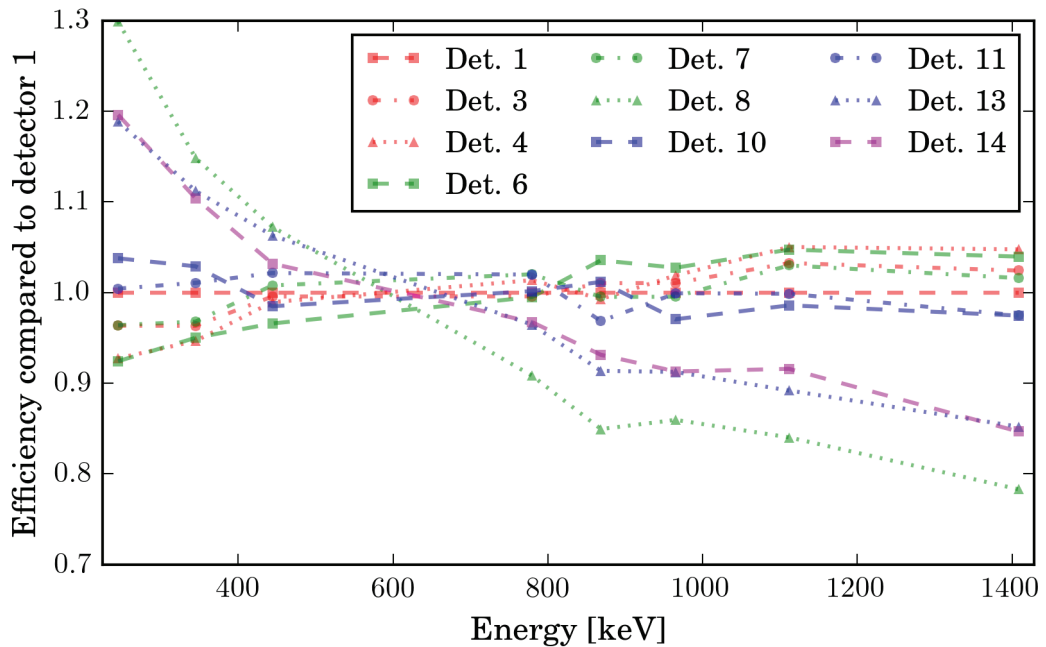

Figure 4.6: Relative efficiency curves normalized to Ge1. The efficiency decreases faster for detector 8, 13 and 14 as a function of energy, compared to the other detectors.

To account for the detector efficiency, the relative efficiencies were summed over all detector pairs corresponding to the same relative angle.

4.2.3 γ spectra

Energy calibrated coincidence data were divided into 66 $\gamma - \gamma$ matrices, one for each detector pair. Spectra collected by the detector pairs forming the same relative angle were then summed up together. FWHM of the 531 keV line after the summation are listed in Tab. 4.3 together with the number of coincidence events at $531 - 460$ and $531 - 1068$ keV γ energies. The spectra gated in coincidence with a γ ray of 531 keV energy are shown in Fig. 4.7, for three relative angles.

	FWHM	Coincidences	
	[keV]	531-460 keV	531-1068 keV
42°	1.82	500(36)	277(17)
70°	1.86	1384(68)	701(26)
110°	1.81	1301(42)	692(26)
140°	1.76	437(97)	178(13)
180°	1.79	413(22)	463(22)

Table 4.3: FWHM at 531 keV, after summation of spectra corresponding to the same relative angle and the number of coincidences for the considered cascades.
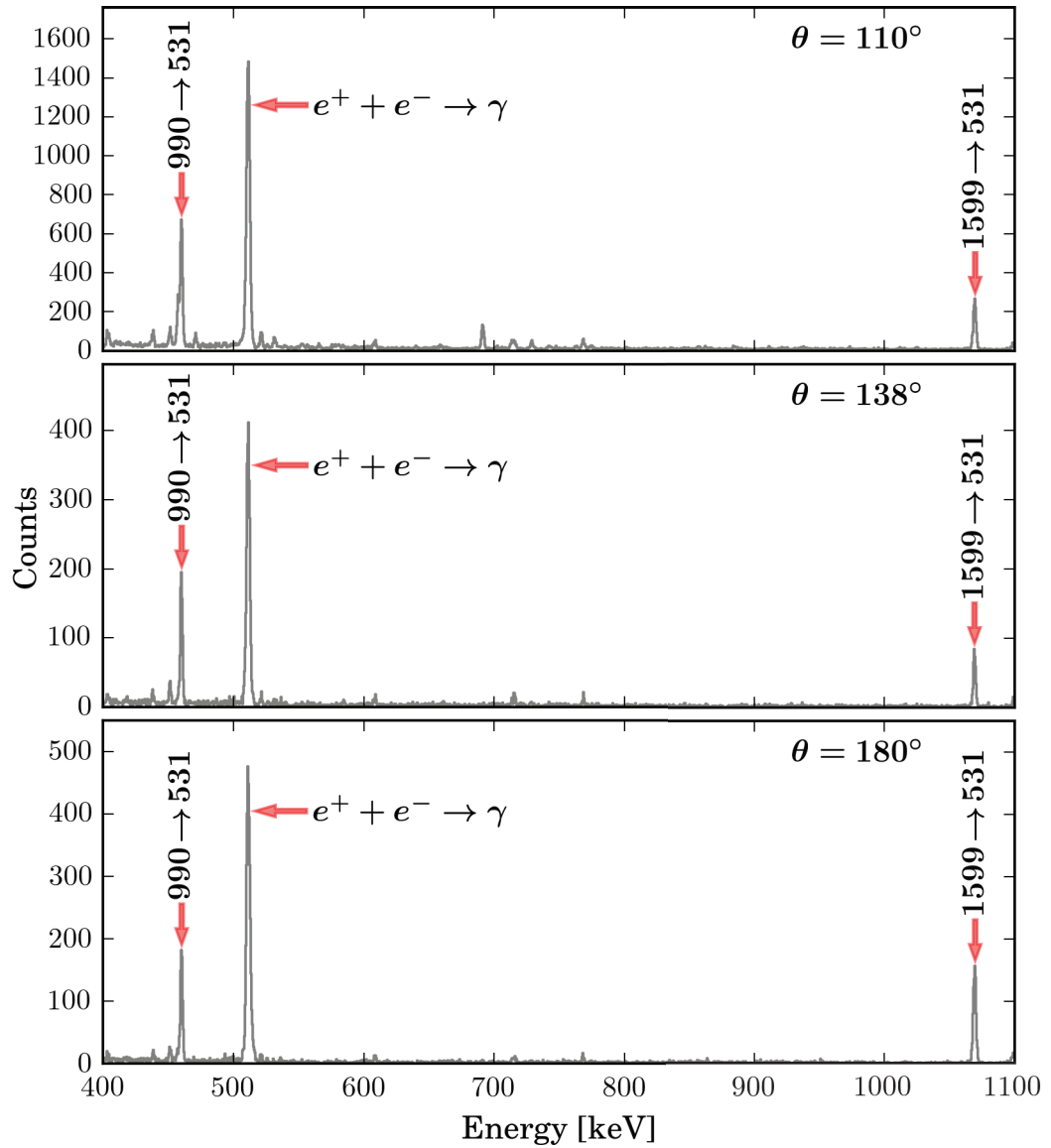
Figure 4.7: Coincidence spectra, gated on the line at 531 keV in the other detector.

4.2.4   Determination of A_{22}, A_{44} and the δ-mixing ratio

The angular correlation factors, A_{22} and A_{44} were first extracted without requiring any correlation between A_{22} and A_{44} in a fit of experimental intensities to Eq. (2.24). To account for the approximately $10°$ opening angle of each germanium detector, the A_{kk} factors were divided by the solid angle correction factors, $Q_{kk} = Q_k^{Ge1} \cdot Q_k^{Ge2}$, calculated from Eq. (4.2),

$$Q_k = \frac{\int_0^\rho P_k(\cos(\theta))\epsilon(\theta)\sin(\theta)d\theta}{\int_0^\rho \epsilon(\theta)\sin(\theta)d\theta}, \tag{4.2}$$

where ρ is the angle between the detector edge and the center. It was assumed that the relative efficiency as a function of angle, $\epsilon(\theta)$, follows the trend presented in Eq. (4.3) [23],

$$\epsilon(\theta) = 1 - e^{-\tau\rho x}, \tag{4.3}$$

where x is the path length in the detector, ρ is the density and τ is the absorption factor at 500 keV. The Q_k values for each detector are presented in Tab. 4.1. In this experiment the differences in Q_k values between two detectors were small compared to statistical errors and the mean value was used in the analysis. The main contributions to the error bars are statistical errors and errors from the relative efficiencies between different detectors. To estimate the error from the efficiency, the relative intensities of the peaks at 531 and 404 keV for different runs were compared.

Extracted A_{22} and A_{44} values are presented in Fig. 4.8 for the γ cascades at $460 - 531$, $1068 - 531$ and $1097 - 531$ keV seen in Fig. 1 in Paper 2. In Fig. 2 in Paper 2, the fit to theoretical $W(\theta)$ is shown. The results indicate that the state at 990 keV excitation energy in ^{140}Sm, previously assigned (0^+), is 2^+, while the state at 1599 keV excitation energy, previously assigned 2^+, is actually $0^{(+)}$ and that the state at 1628 keV is $0^{(+)}$. The mixing ratio, δ, for $M1/E2$ multipolarities was also extracted, assuming a $2^+ \rightarrow 2^+ \rightarrow 0^+$ cascade. As seen in Fig. 4.9, the resulting χ^2/N_{dof} of the fit suggest almost pure $E2$ transition.

To test the reliability of the analysis, the method was applied on the well known $0^+ \rightarrow 2^+ \rightarrow 0^+$ cascade from the state at 1414 keV excitation energy in ^{140}Nd and on the $2^+ \rightarrow 2^+ \rightarrow 0^+$ cascade from the state at 1086 keV excitation energy in ^{152}Sm. For ^{152}Sm, coming from the ^{152}Eu source, the efficiency calibration without the internal adjustment was used. The results shown in Fig. 4.8, are in good agreement with previous assigned spin states [49].
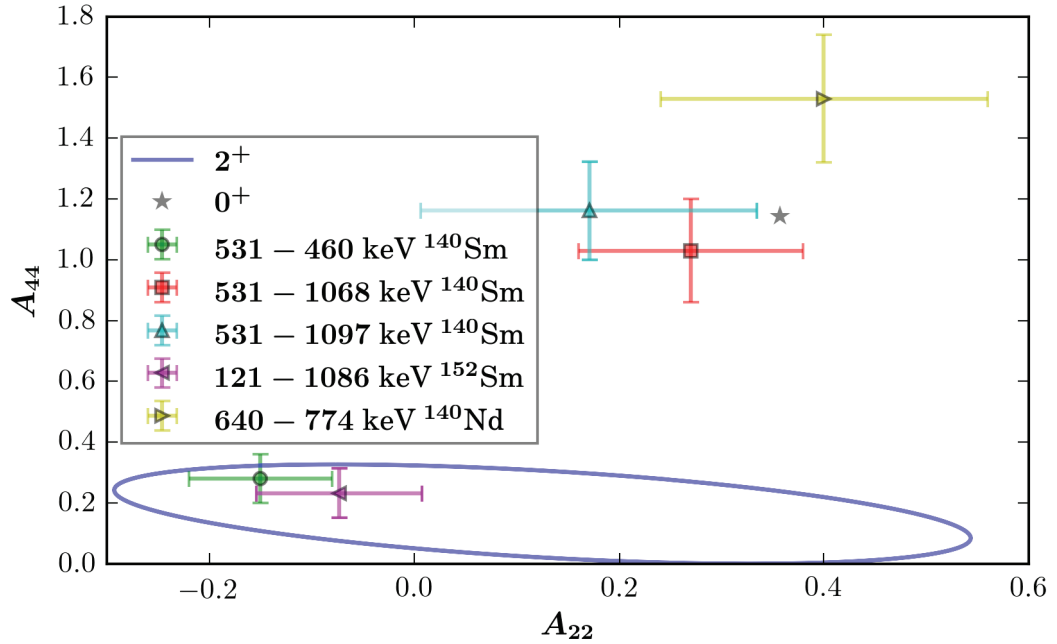
Figure 4.8: Angular correlation coefficients, A_{22} and A_{44} extracted in this experiment.
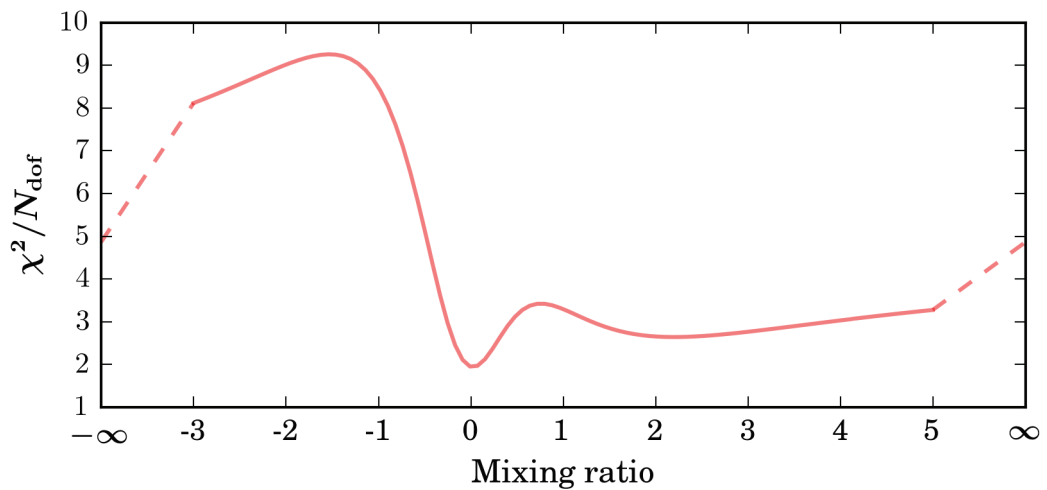
Figure 4.9: The χ^2/N_{dof} of the fit of the M1/E2 mixing ratio for the $2_2^+ \rightarrow 2_1^+ \rightarrow 0^+$ transition in ^{140}Sm. The minimum value suggest almost pure $E2$ transition.

With the new $0^{(+)}$ spin-parity assignment of the state at 1599 keV, the observed γ line of 352 keV energy, suggested in [31] to originate from the transition from the state at 1599 keV to the 4_1^+ state, would correspond to a $4^+ \rightarrow 0^+$ transition, which is very unlikely. In this recent experiment, no γ line at 352 keV was observed when gating on coincidences with the $4_1^+ \rightarrow 2_1^+$ transition, hence if this line belongs to a transition in ^{140}Sm it is located elsewere in the level scheme. For more detailed discusion on this subject, see Paper 2.

Chapter 5

RDDS measurements in $A \approx 60$ nuclei

As discussed in Chapter 3, both Coulomb excitation and lifetime mea-
surements can be used to extract electromagnetic transition strengths in
nuclei. In the work presented in this chapter, the Recoil Distance Doppler
Shift (RDDS) method was applied to measure lifetimes of excited states in
nuclei in the $A \approx 60$ region (marked in Fig. 1.1). The experiment was
performed at the Grand Accélérateur National d'Ions Lourds (GANIL)
facility in Caen, France. This region of modified shell structure is a so-
called *island of inversion*, where an increased collectivity and weakening of
the shell gap at $N = 40$ are seen below $Z = 28$. This effect is interpreted
in the frame of the shell model as an influence of the monopole part
of the tensor force between the $1f_{7/2}$ protons and $1g_{9/2}$ neutrons [51].
The first island of inversion discovered was around $N = 20$ [52, 53].
Although the theoretical calculations, performed using the shell-model
constrained to the *sd*-shell, were in good agreement with the $N < 20$
isotopes for both binding energies and spin-parity assignments, a sudden
disagreement was seen for $N = 20$. For example, the ground state of
^{31}Na ($N = 20$), was predicted by the shell model to be a $(5/2)^+$ state
whereas experimentally a $(3/2)^+$ state was observed. At the same time
the nucleus was significantly more bound than predicted. Also the energy
of the first excited 2^+ in the even-even magnesium isotopes showed
a sudden disagreement at $N = 20$, with the experimentally observed
value being much lower than expected. This could later be explained
theoretically [54] when shell-model calculations including also the fp-
shell for neutrons were performed. It was seen that for $N = 20 - 22$
the $2p2h$ neutron excitation to the fp-shell constituted the ground-state,
instead of the conventional *sd* configuration. Thus the term *island of*

inversion. Three different effects were seen to contribute to this inversion of the energy levels [54]: (a) A reduction of the shell-gap between the *sd* and *fp* shells, (b) increased pairing correlations between the two excited neutrons and (c) an increased proton-neutron correlation. The island of inversion around $N = 20$ is now known to be only one of many such islands of inversion [55], with the one at $N = 40$ studied in this chapter being another example [56].

The following chapter describes the RDDS experiment and the determination of lifetimes in ^{62}Fe, ^{64}Fe, ^{61}Co, ^{63}Co, ^{59}Mn and ^{65}Ni. The experimental details are described in Section 5.1 and the data analysis and results are presented in Section 5.2 and 5.3, respectively.

5.1 Experimental setup

Excited nuclei in the $A \approx 60$ region were produced in a multi-nucleon transfer-reaction between a 6.5A MeV ^{238}U beam and a 1.25 mg/cm^2 thick ^{64}Ni target, at Ganil. The target-like reaction products were detected in the VAMOS spectrometer [57], with the optical axis positioned at 45° with respect to the beam direction. For identification of particles in VAMOS, the energy loss, ΔE, the residual energy, E, and the time-of-flight, *TOF*, are measured. The position is measured by two drift chambers, the energy loss by a segmented ionization chamber, the residual energy by a second ionization chamber and the time-of-flight by a secondary electron-based fast-timing detector and the Dual Position Sensitive Multi-Wire Proportional Counter. The total area of the focal plane of VAMOS is 1000 mm × 150 mm [57]. For a schematic view of the spectrometer, see Fig. 5.1.

The dimensionless mass-to-charge ratio, M/Q, is related to the magnetic rigidity, $B\rho$, of the dipole magnet in VAMOS via Eq. (5.1),

$$\frac{M}{Q} = \frac{eB\rho}{m_a c \gamma \beta},$$

(5.1)

where m_a is the atomic mass, β is the velocity of the particle and $\gamma = \frac{1}{\sqrt{1-\beta^2}}$. In this experiment, $B\rho = 0.97$ was first used and later $B\rho = 0.92$. The $B\rho$ was changed to investigate if this could improve the statistics. This was, however, not the case.

The γ photons were detected in 19 crystals forming the AGATA γ-tracking HPGe array [26], shown in Fig. 5.2. Each crystal is segmented using 36 electrodes and has one common core anode. An incident
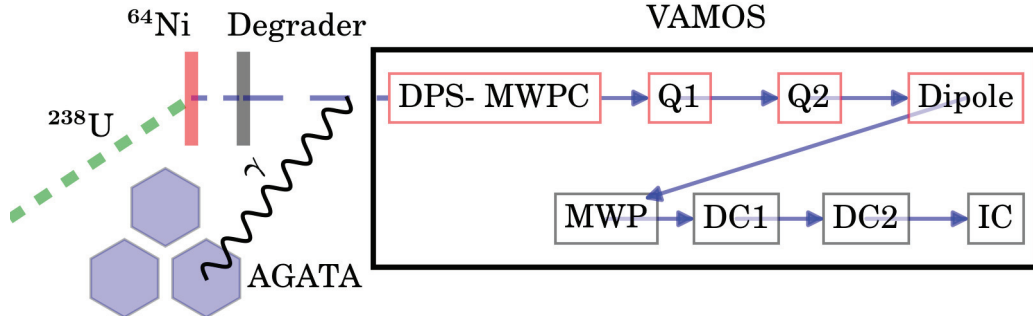
Figure 5.1: A schematic view of the VAMOS spectrometer. The position is measured by a pair of drift chambers (DC), the energy loss by a segmented ionization chamber (IC), the residual energy by a second ionization chamber and the time of flight by the Dual Position Sensitive Multi-Wire Proportional Counter (DPS-MWPC) and a secondary electron based fast timing detector (SeD).

γ ray interacts with the germanium detectors at discrete *interaction points* through the photoelectric effect, Compton and Rayleigh scattering and pair production. By detecting the energy and location of all interaction points and knowing the theoretical behaviour of the interaction mechanisms the γ ray paths and energies are reconstructed. All 37 signals are pre-amplified and transmitted to the pre-processing system, including pulse-shape analysis (PSA). Here the position of all interaction points are determined from the pulse shape of the signals with an accuracy better than 5 mm. This is possible due to well developed pulse-shape simulations and experiments with collimated γ sources. The risetime of the net-charge signal and the amplitude and shape of the transient signals on neighboring crystals are compared to pre-determined reference signals to obtain the location of the interaction. To deduce the total energy of the photons the γ trajectories in the detectors are reconstructed in advanced tracking algorithms. A chi squared function is minimized to find the energies and paths that best fit the measured interaction points. This is a computationally demanding task and often requires a dedicated farm of computers, as is the case for AGATA. In this experiment the detectors covered the backward angles from 145° to 180°. A 3.0 mg/cm^2 thick ^{24}Mg degrader was used to slow down the recoiling particles, in order to apply the RDDS method. The degrader was positioned at six distances in the μm range, controlled by the plunger device shown in Fig. 5.3.

Figure 5.2: The γ photons were detected in 19 crystals from the AGATA γ tracking Ge array, positioned 23.5 cm from the target chamber.
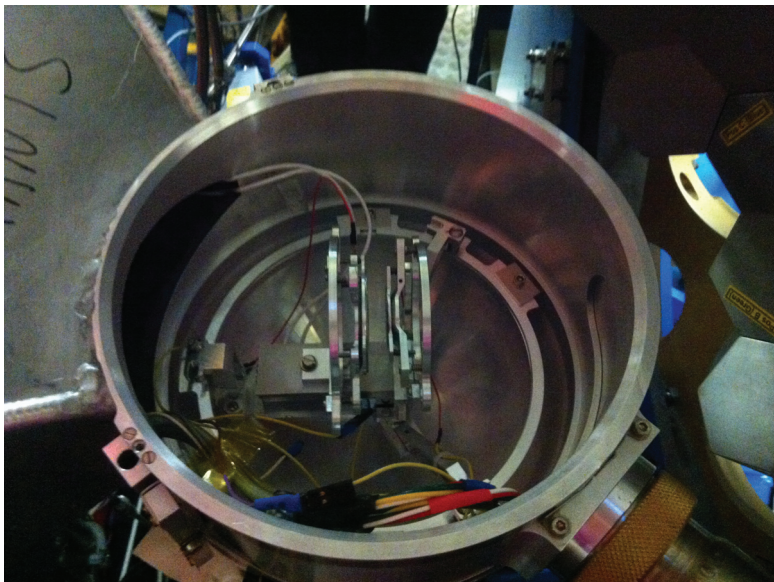
Figure 5.3: The plunger device with mounted target, used in the RDDS measurement to control the position of the degrader.

5.2 Data analysis

5.2.1 Efficiency calibration

Efficiency calibration of the AGATA crystals was performed as described in Chapter 2, using the known γ transitions from ^{152}Eu, as displayed in Fig. 5.4. To ensure all crystals exhibit the same behavior, relative efficiency curves were obtained for each crystal, as presented in Fig. 5.5. In the further analysis the total relative efficiency curve after tracking was used.
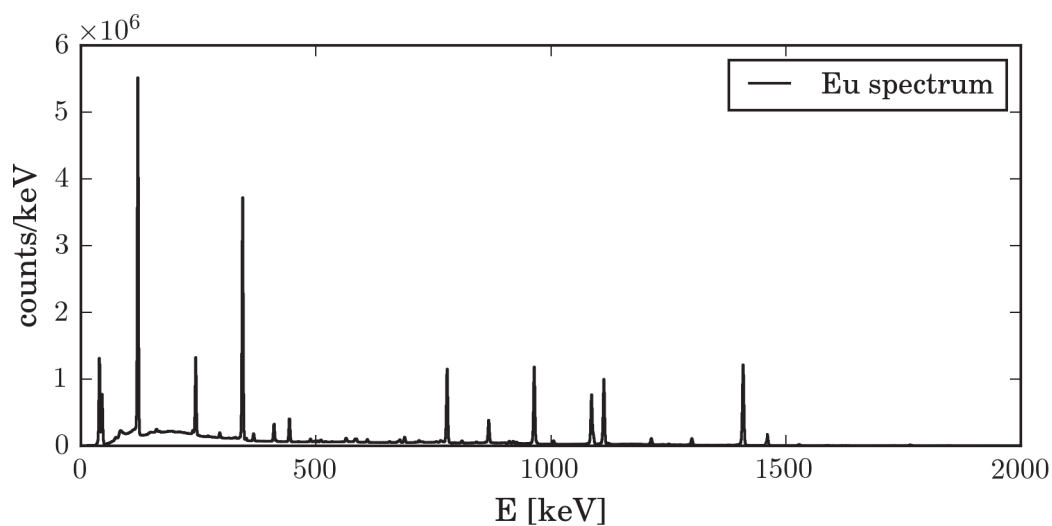
Figure 5.4: The ^{152}Eu γ-ray spectrum, used for efficiency calibration of the AGATA detector.
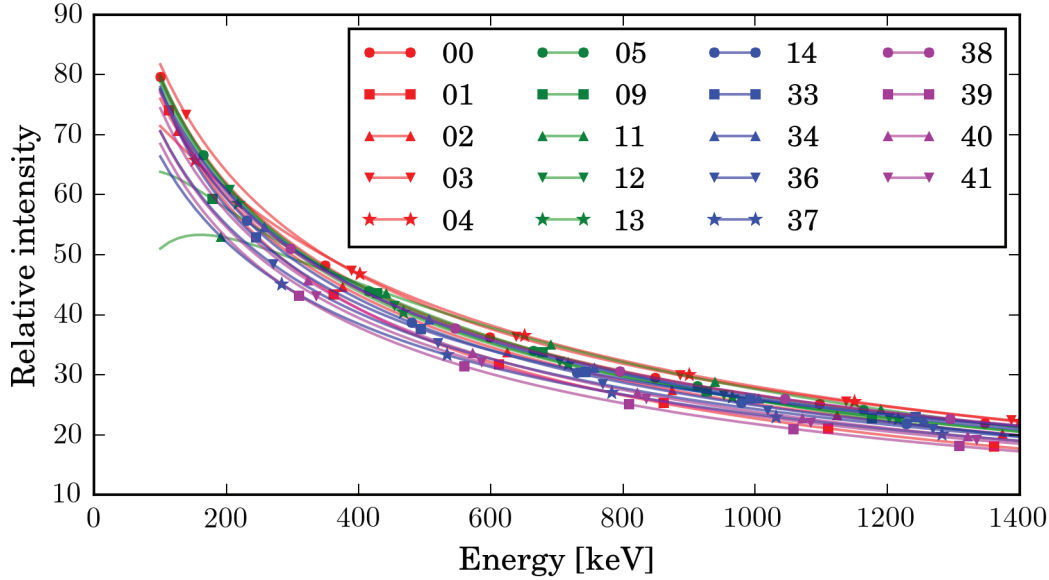
Figure 5.5: Relative efficiency curves obtained for each AGATA crystal used in this experiment.

5.2.2 Particle identification

To select prompt particle-γ coincidence events, the time gate shown in Fig. 5.6, was applied on the spectrum of the AGATA timestamp as a function of VAMOS time. The VAMOS time is from the time of detection of a particle in the MWP detector. Charged particle identification in the VAMOS spectrometer was performed using the dependence of energy loss as a function of total particle energy on the recoiling isotope, presented in Fig. 1 in Paper 4, where nickel, cobalt, iron and manganese ions are marked. The isotopes were further selected from the mass-to-charge ratio as a function of mass number. In Fig. 5.7 the gates on ^{64}Ni, ^{62}Fe, ^{63}Co and ^{59}Mn are marked. Slightly different gates on energies and masses were applied for the data taken before and after the change of magnetic field, Bρ. Further, distributions of masses for iron, cobalt and manganese isotopes are presented in Fig. 2 in Paper 4.

The velocity distribution of the particles after passing through the degrader, measured in VAMOS, yielded the mean β velocity of 0.109(5) for ^{64}Ni isotopes. Since the γ spectra were Doppler corrected for the particle velocity after the degrader, the mean energy of the shifted component detected in backwards angles (145° − 180°) is lower than the unshifted component.

Figure 5.6: A time gate for prompt particle-γ coincidences was applied on the AGATA timestamp as a function of VAMOS time.
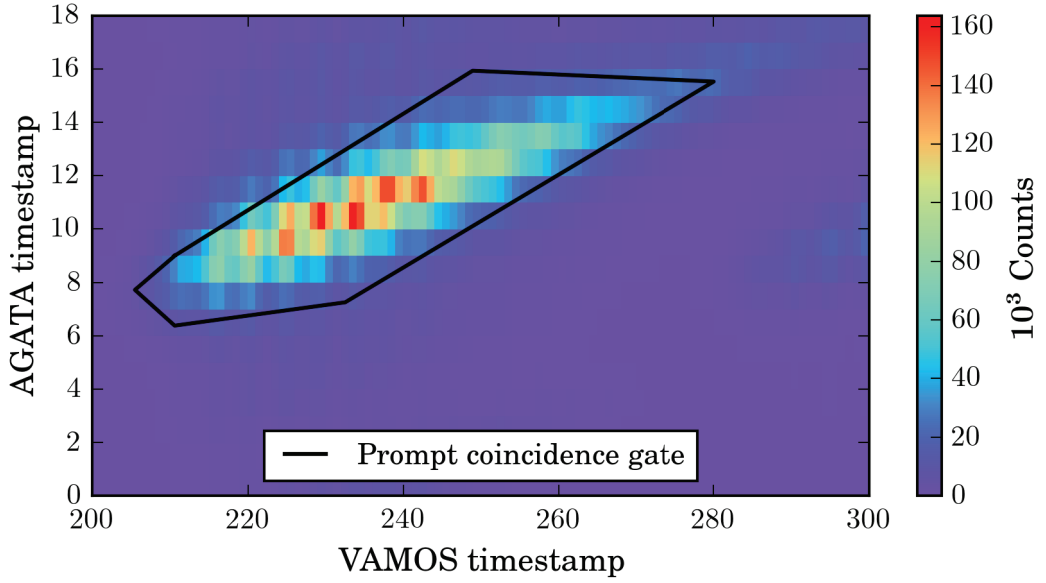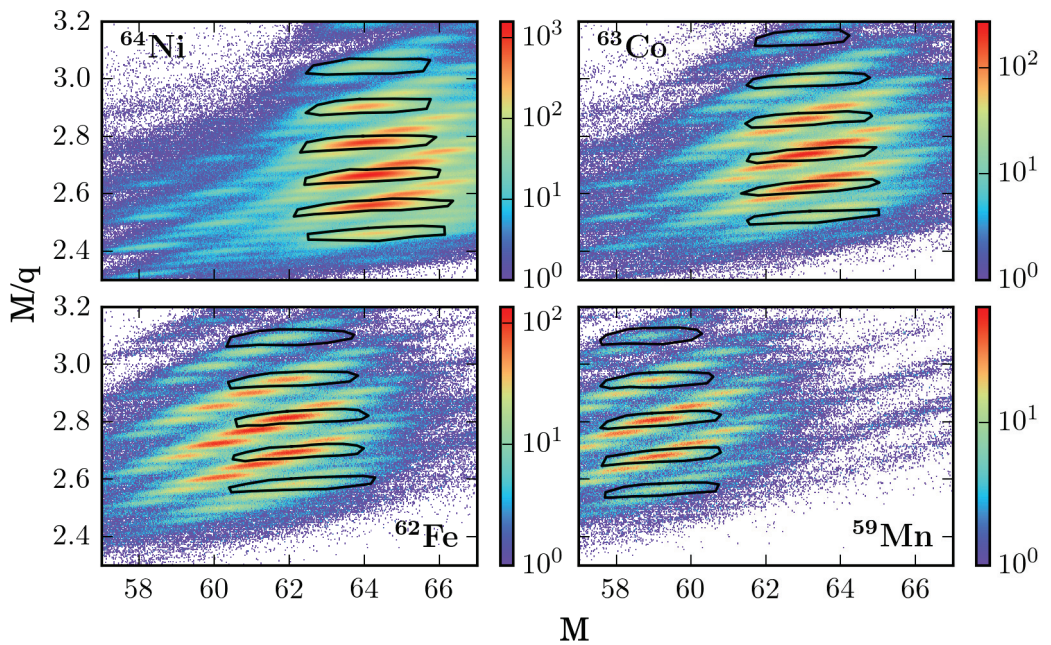

Figure 5.7: The mass-to-charge ratio as a function of mass number obtained after Z identification.

5.2.3 Lifetime extraction

Two approaches to extract lifetimes were used in this analysis. In the first approach, decay curves were fitted to exponential functions in a χ^2 minimization. The second was based on the differential decay curve method described in Chapter 2 and spline interpolation of the decay curve.

Exponential fit

This approach was used to obtain the results presented in Paper 4. Decay curves for the level of interest, R, and possibly an observed feeder, $R_{\text{feed.}}$ were constructed according to Eq. (5.2),

$$
\begin{aligned}
R^{(\text{exp})} &= \frac{I_u^{(\text{exp})}}{I_s^{(\text{exp})} + I_u^{(\text{exp})}} \\[2mm]
R_{\text{feed.}}^{(\text{exp})} &= \frac{1}{\epsilon_{\text{rel.}}^{(\text{exp})}} \frac{I_{u,\text{feed.}}^{(\text{exp})}}{I_s^{(\text{exp})} + I_u^{(\text{exp})}}
\end{aligned}
\tag{5.2}
$$

where $I_s^{(\text{exp})}$ and $I_u^{(\text{exp})}$ are the measured shifted and unshifted components, respectively, of the level of interest and $I_{u,\text{feed.}}^{(\text{exp})}$ is the unshifted component of the observed feeder. $\epsilon_{\text{rel.}}^{(\text{exp})}$ is the γ efficiency for the feeder peak relative to the level of interest.

Lifetimes were fitted to the observed γ decays, by solving the coupled linear differential equations arising from the decay of the level of interest and its feeders. The model for the level schemes used in this work consists of the level of interest, possibly a seen feeder and an *unseen feeder*, which is a virtual level approximating the feeding to the level of interest from other levels. Given the proportion of decays coming from the feeders, $N_{0,\text{feed.}}$ and $N_{0,\text{unseen}}$, and the lifetimes, τ, $\tau_{\text{feed.}}$ and τ_{unseen}, the fitted decay curves are

$$
\begin{aligned}
R(t) =\;& e^{-t/\tau} + N_{0,\text{feed.}} \tau_{\text{feed.}} \frac{e^{-t/\tau_{\text{feed.}}} - e^{-t/\tau}}{\tau_{\text{feed.}} - \tau} \\[2mm]
& + N_{0,\text{unseen}} \tau_{\text{unseen}} \frac{e^{-t/\tau_{\text{unseen}}} - e^{-t/\tau}}{\tau_{\text{unseen}} - \tau} \\[2mm]
F(t) =\;& 1 - R(t) \\[2mm]
R_{\text{feed.}}(t) =\;& N_{0,\text{feed.}} e^{-t/\tau_{\text{feed.}}},
\end{aligned}
\tag{5.3}
$$

where F is the flight curve. Experimental data was obtained for $N_{\text{dist}} = 6$ different distances, $d_n^{(\text{exp})}$, of the degrader. The corresponding time-of-flight to the degrader is

$$t_n^{(\text{exp})} = \frac{d_n^{(\text{exp})} - d_{\text{off.}}^{(\text{exp})}}{v^{(\text{exp})}}, \tag{5.4}$$

where $v^{(\text{exp})}$ is the speed of the particles before the degrader. $v^{(\text{exp})}$ was obtained from the shifts of the $2_1^+ \to 0_1^+$ γ transition in ^{64}Ni. The velocities of the other isotopes studied in this experiment were estimated from the calculated energy loss in the degrader, using SRIM [45]. The velocities differed by up to about 3% from the value obtained for ^{64}Ni. To verify that the velocities were correct, the spectra were Doppler corrected for the velocities before the degrader, resulting in sharp peaks corresponding to the decay before the degrader. The offset $d_{\text{off.}}^{(\text{exp})}$ was not measured during the experiment, therefore, a value for the offset was obtained from the well-constrained fit of the lifetime of the 2_1^+ state in ^{64}Ni, resulting in $d_{\text{off.}}^{(64\text{Ni})} = -16.50 \pm 0.69$ μm.

The intensities needed to be normalized to allow for a direct comparison between experimental intensities for different distances. This is done by fitting normalization constants $I_{s+u,n}$, one for each distance of the degrader. By using both the shifted and unshifted component from the level of interest, the normalization constants, $I_{s+u,n}$, are constrained by the total number of detected γ decays from this level, $I_{s,n}^{(\text{exp})} + I_{u,n}^{(\text{exp})}$. The lifetimes that best describe the data are found using a non-linear least-squares minimization,

$$\chi^2\left(\tau, \tau_{\text{feed.}}, \tau_{\text{unseen}}, N_{0,\text{feed.}}, N_{0,\text{unseen}}, \vec{I}_{s+u}, v, \epsilon_{\text{rel.}}, d_{\text{off.}}, \vec{d}\right) =$$

$$\sum_{n=1}^{N_{\text{dist}}} \left[\left(\frac{I_{u,n}^{(\text{exp})} - I_{s+u,n}R(t_n)}{\sigma_{I_{u,n}^{(\text{exp})}}}\right)^2 + \left(\frac{I_{s,n}^{(\text{exp})} - I_{s+u,n}F(t_n)}{\sigma_{I_{s,n}^{(\text{exp})}}}\right)^2 \right.$$

$$\left. + \left(\frac{I_{u,n,\text{feed.}}^{(\text{exp})} - \epsilon_{\text{rel.}}I_{s+u,n}R_{\text{feed.}}(t_n)}{\sigma_{I_{u,n,\text{feed.}}^{(\text{exp})}}}\right)^2 \right] + \left(\frac{v^{(\text{exp})} - v}{\sigma_{v^{(\text{exp})}}}\right)^2 \tag{5.5}$$

$$+ \left(\frac{\epsilon_{\text{rel.}}^{(\text{exp})} - \epsilon_{\text{rel.}}}{\sigma_{\epsilon_{\text{rel.}}^{(\text{exp})}}}\right)^2 + \left(\frac{d_{\text{off.}}^{(64\text{Ni})} - d_{\text{off.}}}{\sigma_{d_{\text{off.}}^{(64\text{Ni})}}}\right)^2 + \sum_{n=1}^{N_{\text{dist}}} \left(\frac{d_n^{(\text{exp})} - d_n}{\sigma_{d_n^{(\text{exp})}}}\right)^2,$$

where $t_n = (d_n - d_{\text{off.}})/v$. d_i are the fitted distances, v the velocity and $I_{s+u,i}$ the fitted normalizations for the distances. By fitting the velocity, distances, distance offset, γ efficiency and normalizations, the systematical uncertainties from these quantities were correctly taken into account in the fitting. Thus, the uncertainties in the obtained lifetimes incorporate all of these sources of experimental uncertainty. This is a frequently used method to account for *systematical uncertainties* in the experimental data, for example induced correlations caused by the normalization. This method also makes it possible to determine how much the different sources of experimental uncertainties influence the values and uncertainties of the obtained lifetimes.

For the purpose of the error analysis, correlations between e.g. the velocity of the particles and the lifetimes can be obtained. The covariance matrix, C, for the parameters was extracted from the Hessian matrix, H, defined in Eq. (5.6).

$$H_{ij} = \frac{\partial^2 \chi^2(\tilde{\boldsymbol{\alpha}})}{\partial \alpha_i \partial \alpha_j}. \tag{5.6}$$

Here $\vec{\alpha}$ are the model parameters, consisting of τ_i, $N_{0,i}$, $I_{s+u,i}$, v, $\epsilon_{\text{rel.}}$, $d_{\text{off.}}$ and d_i. The relation between the Hessian and the covariance matrix is given in Eq. (5.7) [58]

$$C = 2H^{-1}. \tag{5.7}$$

The *statistical uncertainties* of the fitting parameters, $\tilde{\boldsymbol{\alpha}}$ are obtained from the diagonal of the covariance matrix, $\sigma_{\alpha_n} = \sqrt{C_{nn}}$. As explained in Ref. [58], a good approximation of H is $H \approx 2J^T J$ where $J_{ni} = \frac{\partial r_n}{\partial \alpha_i}$ and r_n^2 is the nth term in the chi-squared function in Eq. (5.5). In this analysis, the Jacobian elements J_{ni} were calculated using finite differences. The number of *degrees of freedom* is $N_{\text{dof}} = N_{\text{res}} - N_{\tilde{\alpha}}$. In a correct model it is expected that $\chi^2(\vec{\alpha}_*)/N_{\text{dof}} = 1 \pm \sqrt{2/N_{\text{dof}}}$, where $\vec{\alpha}_*$ are the obtained optimal parameters.

The DDCM approach

The extraction of lifetimes from the method described above were compared to the results obtained using the conventional DDCM method, in the program `thePlunger`, developed by Joa Ljungvall [59]. In this method the decay curves are fitted using splines to derive the derivatives [21]. The input to the program consists of the number of detected γ photons from

the state of interest and from the feeding states, for each distance, normalization constants, the velocity before the degrader, relative γ efficiency and angular correlation coefficients. The program allows to include the intensity and lifetime of assumed unseen feeding

5.3 Results

^{64}Ni

To test the reliability of the analysis, first the method was applied to the well known lifetime of the first 2^+ in ^{64}Ni [60]. The spectrum for the shortest distance, gated on ^{64}Ni particles is shown in Fig. 5.8. The shifted and unshifted component of the $2_1^+ \rightarrow 0_1^+$ transition at 1346 keV, the $4_1^+ \rightarrow 2_1^+$ transition at 1264 keV, the $2_2^+ \rightarrow 2_1^+$ transition at 931 keV, the $4_2^+ \rightarrow 2_1^+$ transition at 1820 keV (only shifted component) and the $5_1^- \rightarrow 4_1^+$ transition at 1239 keV are visible in the presented spectrum. Since only the shifted component of the $4_2^+ \rightarrow 2_1^+$ transition is present in the γ-ray spectrum, the lifetime of this state is clearly too short to affect the feeding of the 2_1^+ state. For the shortest distance the unshifted component of the $4_1^+ \rightarrow 2_1^+$, the $2_2^+ \rightarrow 2_1^+$ and the $5_1^- \rightarrow 4_1^+$ transitions are weak while they increase in the spectra obtained for longer distances.
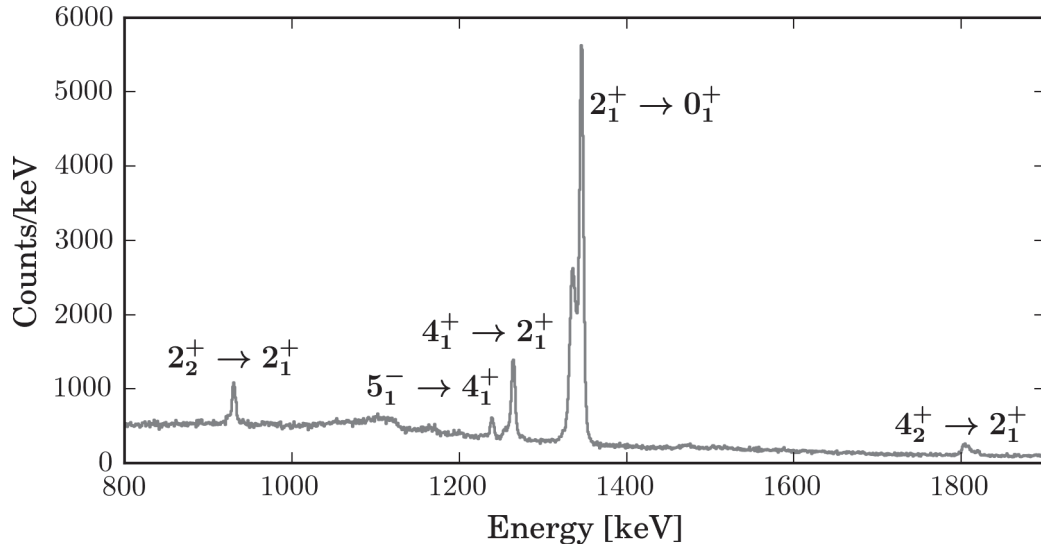

Figure 5.8: The γ spectrum for the shortest distance, gated on ^{64}Ni particles.

The transitions presented in Fig. 5.9 were fitted to the sum of two

Gaussian distributions. However, GEANT4 [61] simulations of the peak shape showed a left-hand side tail of the unshifted peak resulting from the emission of γ photons during the retardation of the particles in the degrader. This tail contained about 10% of the total counts in the peak and was taken into account by subtracting 10% of the counts in the shifted component and adding it to the unshifted component. GEANT4 simulations of the total γ spectrum for the shortest distance is shown in Fig. 5.10. Lifetimes for the included levels were taken from known values [60] and the intensities of the transitions used in the simulation were chosen so that the experimental data was reproduced.
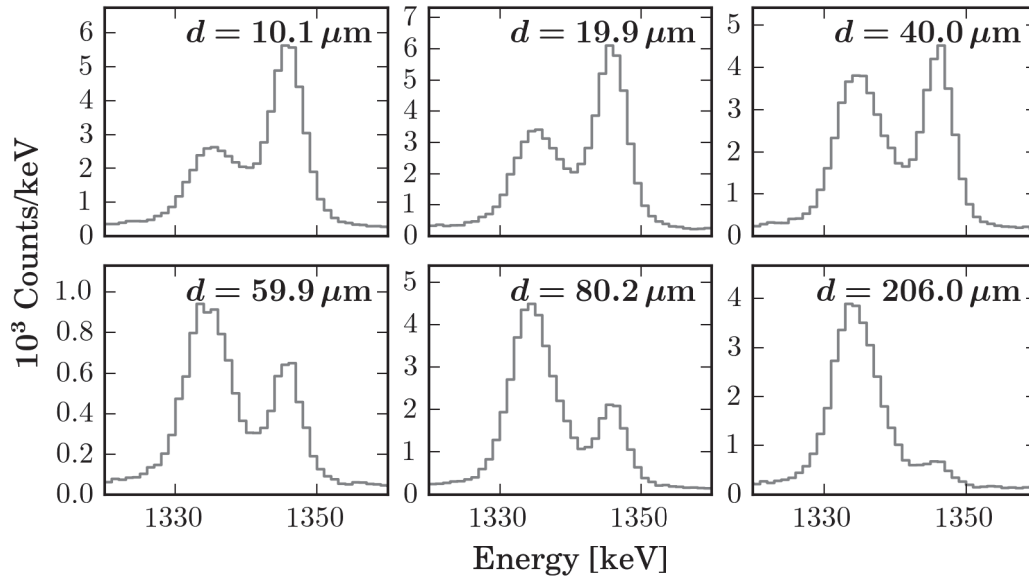
Figure 5.9: The shifted and unshifted component of the γ peaks were fitted simultaneous assuming Gaussian shapes and constant background.

For the $2_1^+ \rightarrow 0_1^+$ transition the statistics allowed to fit the width of the peaks in the fit, resulting in an average width of 5.4 and 7.3 keV for unshifted and shifted component, respectively. For the feeding $4_1^+ \rightarrow 2_1^+$ transition they were kept fixed at 4.7 keV and 6.1 keV for unshifted and shifted components, respectively. The widths of the $2_2^+ \rightarrow 2_1^+$ transition were fixed to 4.6 and 6.0 keV for unshifted and shifted component, respectively. Tab. 5.1 presents the number of counts in the peaks and the decay curves for the 2_1^+, 4_1^+ and 2_2^+ state in ^{64}Ni are shown in Fig. 5.11. Here all unseen feeding is assumed to be prompt. The exponential fitting approach resulted in $\tau_{2_1^+} = 1.537(76)$ ps and the result obtained with the thePlunger program was $\tau_{2_1^+} = 1.65(10)$ ps. This is in good agreement

Figure 5.10: Geant4 simulation of ^{64}Ni γ spectrum for distance 10 μm.

with the known lifetime of $1.57(5)$ ps [60].

Figure 5.11: Decay curves for the $2_1^+ \to 0_1^+$ (to the left), the $4_1^+ \to 2_1^+$ (in the middle) and the $2_2^+ \to 2_1^+$ (to the right) transitions in ^{64}Ni.

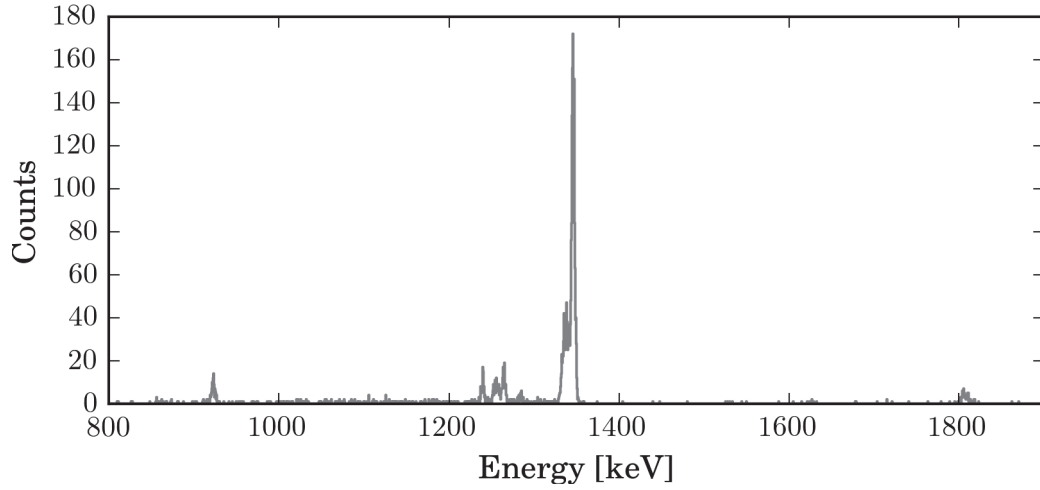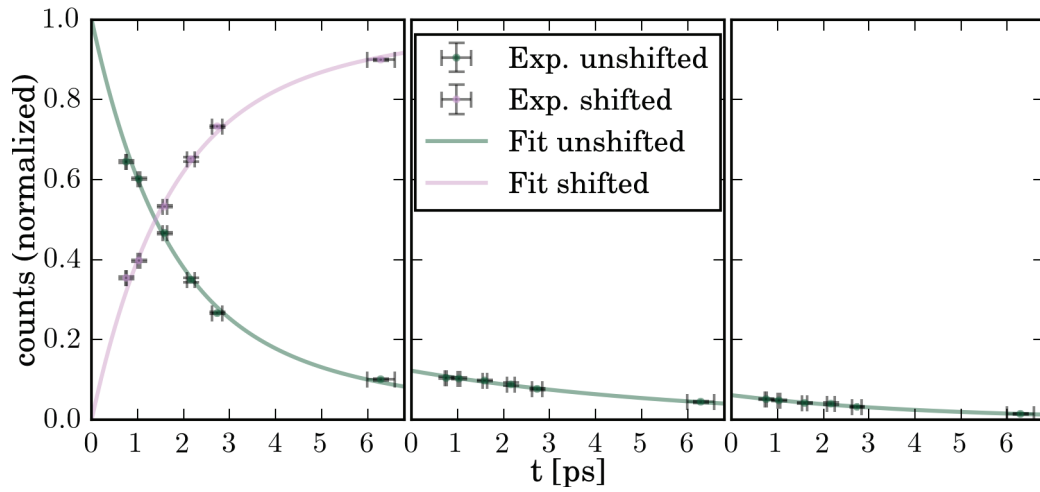| Distance (μm)	I_i	I_f	Counts shifted	Counts unshifted
10.08	2_1^+	0_1^+	18750(220)	34130(250)
10.08	4_1^+	2_1^+	–	5590(110)
10.08	2_2^+	2_1^+	–	2790(91)
19.94	2_1^+	0_1^+	23860(210)	36120(240)
19.94	4_1^+	2_1^+	–	6240(110)
19.94	2_2^+	2_1^+	–	2992(91)
39.98	2_1^+	0_1^+	28730(210)	25110(190)
39.98	4_1^+	2_1^+	–	5310(100)
39.98	2_2^+	2_1^+	–	2356(80)
59.89	2_1^+	0_1^+	6820(98)	3660(76)
59.89	4_1^+	2_1^+	–	937(44)
59.89	2_2^+	2_1^+	–	440(37)
80.25	2_1^+	0_1^+	32190(200)	11720(140)
80.25	4_1^+	2_1^+	–	3381(86)
80.25	2_2^+	2_1^+	–	1473(69)
206.00	2_1^+	0_1^+	28910(190)	3230(96)
206.00	4_1^+	2_1^+	–	1444(65)
206.00	2_2^+	2_1^+	–	500(55)

Table 5.1: The number of counts in the shifted and unshifted component of the γ transition in ^{64}Ni.

$^{60-64}$Fe

An additional check of the reliability in the results was performed using the spectra gated on ^{60}Fe, shown in Fig. 5.12a, to extract the well known lifetime of the 4_1^+ state ($\tau = 1.20(30)$ ps [62]). The fit of the decay curve (see Fig. 5.12b), resulted in $\tau_{4_1^+} = 1.20(30)$ ps with $\chi^2/N_{\mathrm{dof}} = 1.29$.

The γ-spectrum gated on ^{62}Fe is presented in Fig. 5.13, for the shortest distance. The $2_1^+ \rightarrow 0_1^+$ transition at 877 keV, the $4_1^+ \rightarrow 2_1^+$ transition at 1299 keV, the $6_1^+ \rightarrow 4_1^+$ transition at 1211 keV and the $5_1^- \rightarrow 4_1^+$ transition at 839 keV are visible in the spectrum. In Fig. 5 in Paper 4, the $4_1^+ \rightarrow 2_1^+$ transition at 1140 keV is presented for all distances and the number of counts in the $4_1^+ \rightarrow 2_1^+$ transition, the $5_1^- \rightarrow 4_1^+$ transition and the $6_1^+ \rightarrow 4_1^+$ transition are given in Tab. 5.2. From this data the fit of the decay curves results in $\tau_{4_1^+} = 0.79(19)$ ps with $\chi^2/N_{\mathrm{dof}} = 2.48$ and a long lived (> 16 ps) unseen feeder. Excluding the unseen feeder leads to $\tau_{4_1^+} = 1.58(14)$ ps with $\chi^2/N_{\mathrm{dof}} = 4.16$. The improvement of the fit when
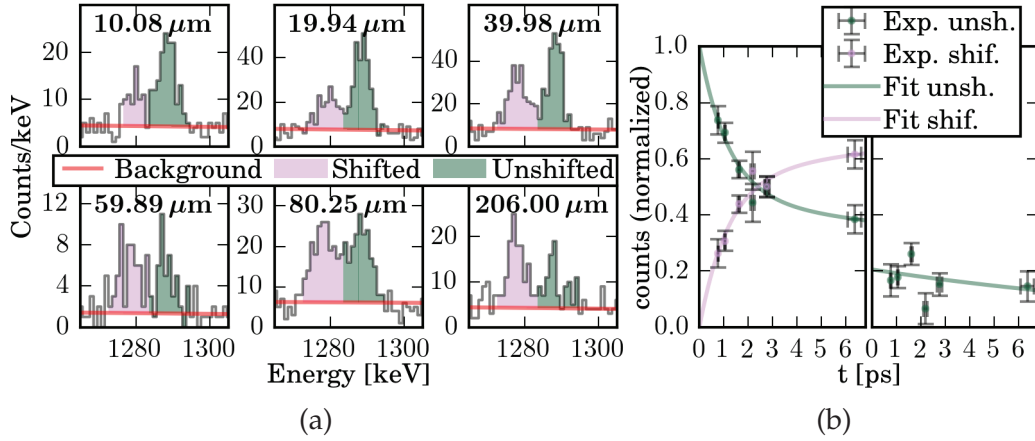
Figure 5.12: As a test of the reliability of the analysis, the spectra gated on ^{60}Fe (in a) were used to obtain the decay curves (in b) and extract the well known lifetime of the 4_1^+ [62].

the unseen feeding is included is further seen in the comparison between Fig. 5.14a and Fig. 5.14b where the fit to the decay curves of the $4_1^+ \to 2_1^+$, the $6_1^+ \to 4_1^+$ and the $5_1^- \to 4_1^+$ transitions are presented with and without unseen feeding, respectively. In particular the last data point is not well reproduced by the fit without slow unseen feeding.
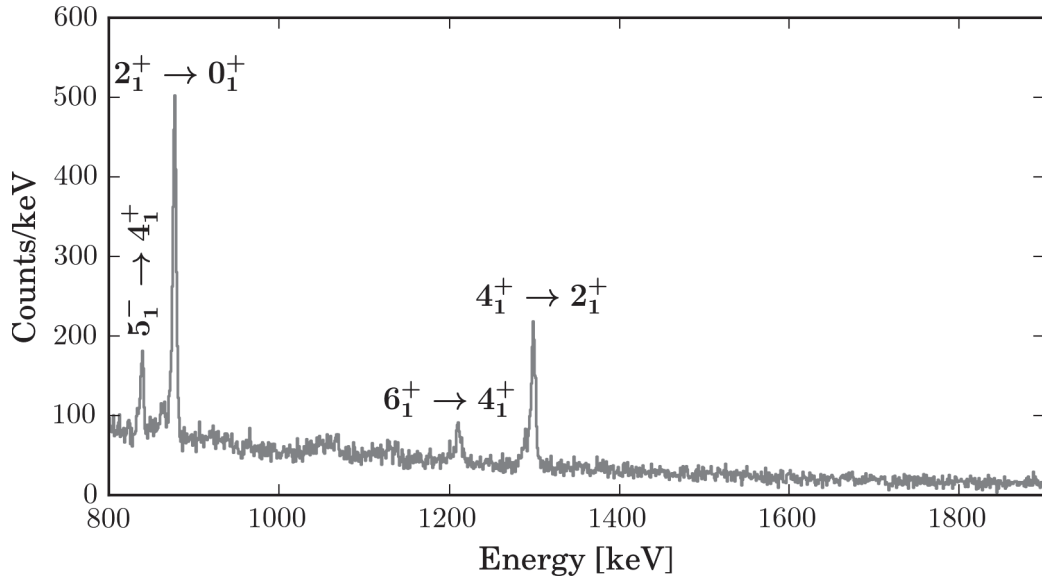
Figure 5.13: The γ-spectrum gated on ^{62}Fe, for the shortest distance.

It was seen that the assumption of a slow unseen feeder was needed

Distance (μm)	I_i	I_f	Counts shifted	Counts unshifted
10.08	4^+	2^+	324(19)	1112(34)
10.08	6^+	4^+	–	357(19)
10.08	5^-	4^+	–	505(22)
19.94	4^+	2^+	437(22)	1357(37)
19.94	6^+	4^+	–	412(20)
19.94	5^-	4^+	–	560(24)
39.98	4^+	2^+	388(20)	963(31)
39.98	6^+	4^+	–	368(19)
39.98	5^-	4^+	–	434(21)
59.89	4^+	2^+	126(11)	177(14)
59.89	6^+	4^+	–	67.4(82)
59.89	5^-	4^+	–	104(10)
80.25	4^+	2^+	412(21)	636(26)
80.25	6^+	4^+	–	238(15)
80.25	5^-	4^+	–	350(19)
206.00	4^+	2^+	405(20)	418(21)
206.00	6^+	4^+	–	105(10)
206.00	5^-	4^+	–	246(16)

Table 5.2: The number of counts in the shifted and unshifted component of the γ transitions in ^{62}Fe.

Figure 5.14: In a), the decay curves for the $4_1^+ \rightarrow 2_1^+$ (to the left), the $6_1^+ \rightarrow 4_1^+$ (in the middle) and the $5_1^- \rightarrow 4_1^+$ (to the right) transitions in ^{62}Fe, used to extract the lifetime of the 4_1^+ state. In b), the fit to the decay curves assuming no unseen feeding. In particular the last data point is not well reproduced by the fit without unseen feeding.

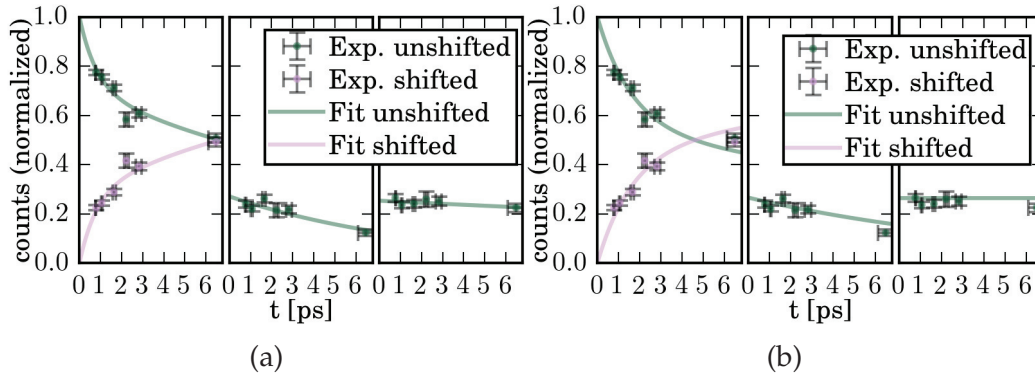to well reproduce the data. In Fig. 5.15a the values of the $\tau_{4_1^+}$ and the corresponding χ^2/N_{dof} are presented as a function of the lifetime of the unseen feeding. It is seen that the minimum value is shallow and all longer lifetimes are possible solutions. Applying the $\chi^2_{min} + 1$ limit, a lower limit of 16 ps could then be obtained. Furthermore, the sensitivity of the lifetime to each distance used in the analysis was investigated by fitting the decay curves excluding each distance, one by one. Lifetimes as a function of distance excluded from the fit are presented in Fig. 5.15b.

<table>
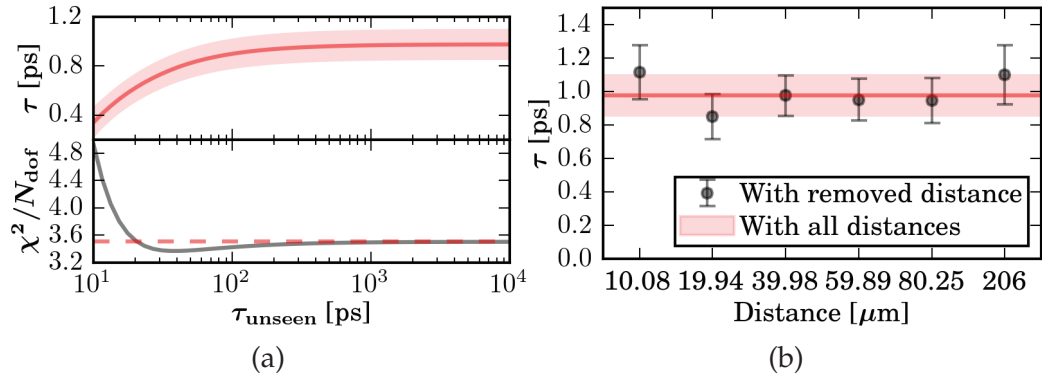<tr><td>(a)</td><td>(b)</td></tr>
</table>

Figure 5.15: In a), the lifetime of the 4_1^+ state and the corresponding χ^2/N_{dof} as a function of lifetime of the unseen feeding. In b), the extracted lifetimes as a function of distance excluded in the fit, performed as a test of the sensitivity of the lifetime to each distance.

A source of uncertainty arose from the γ transition from the $9^- \to 7^-$ transition located at 1297 keV γ energy, that may be hidden within the intensity of the $4_1^+ \to 2_1^+$ transition at 1299 keV, leading to a broadening of the width of the peak. Comparing the width of this peak with the width of the $2_1^+ \to 0_1^+$ transition in ^{64}Ni at similar energy, showed, however, no divergences. The 2.4(8)% intensity of the $9^- \to 7^-$ transition relative to the $4_1^+ \to 2_1^+$ transition, found in Ref. [63] was therefore adopted as the error caused by this. The correlation between the parameters in the χ^2 minimization is presented in Fig. 5.16. It is seen that the lifetime of the 4^+ state is strongly correlated with the population, $N_{0,v}$, and the lifetime, τ_v, of the unseen feeder, hence the error in the obtained τ_{4^+} comes predominantly from the lack of information about the unseen feeding.

Also the γ spectra gated on ^{64}Fe are shown in Fig. 5 in Paper 4. Here the lifetime of the 4_1^+ state was obtained from the shift of the $4_1^+ \to 2_1^+$ transition at 1017 keV. Feeding from the $6_1^+ \to 4_1^+$ transition at 1079 keV and the $5_1^- \to 4_1^+$ transition at 1078 keV observed in the spectrum were
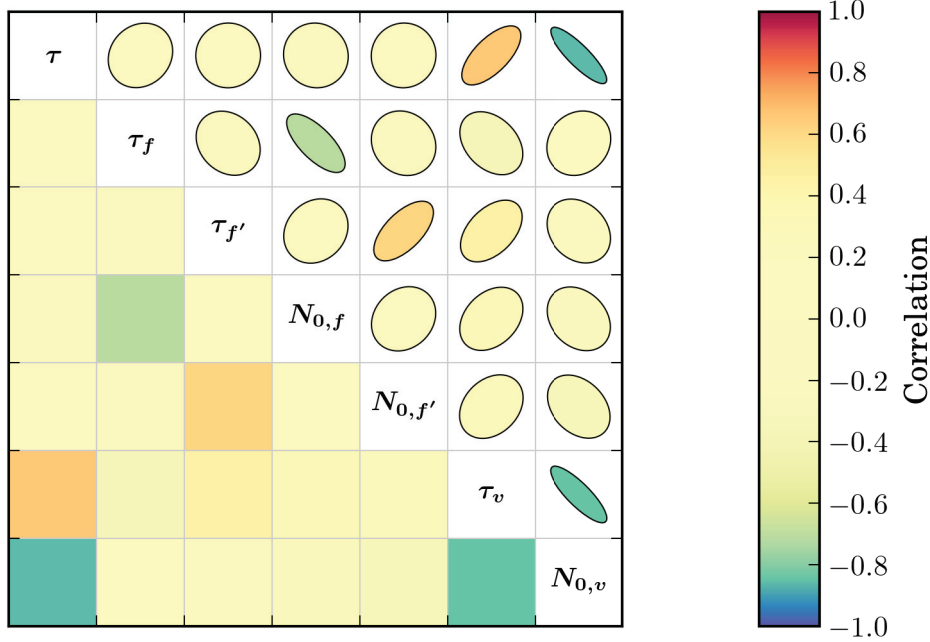
Figure 5.16: Correlation matrices for the parameters in the χ^2 minimization.

included in the fit, resulting in $\tau_{4_1^+} = 0.20(69)$ ps. However, 0.20 ps is below the level of sensitivity for this experiment. Since the inclusion of unseen feeding lowers the lifetime, a safe upper limit of the $\tau_{4_1^+}$ could be obtained assuming no delayed unseen feeding. From this fit the upper limit of 1.6 ps was extracted. In Fig. 7 in Paper 4 the $B(E2; 4_1^+ \rightarrow 2_1^+)$ values obtained for ^{62,64}Fe in this experiment are presented together with shell model calculations and beyond mean field calculations. The results confirm the observation in Ref. [56] of an increased collectivity when going from ^{62}Fe to ^{64}Fe. As further discussed in Paper 4, this is in agreement with the interpretation of a decreased sub-shell gap between the $2\nu p_{1/2}$ and $1\nu g_{9/2}$ orbital.

^{61,63}Co

The γ spectra gated on ^{63}Co, seen in Fig. 5.17a and in Fig. 5 in Paper 4 shows the $(9/2)_1^- \rightarrow (7/2)_1^-$ transition at 1383 keV γ energy and the $(11/2)_1^- \rightarrow (7/2)_1^-$ transition at 1672 keV γ energy, respectively. Fig. 5.17b presents the best fit of the decay curve with an unseen feeding in the order of 18 ps, resulting in $\tau_{(9/2)_1^-} = 0.24(8)$ ps with $\chi^2/N_{\text{dof}} = 4.39$.

As already mentioned, 0.24 ps is below the sensitive region for this RDDS measurement. The rapid change in the decay curve fit at about 0.5 ps, seen in Fig. 5.17b, implies that distances below $10\,\mu m$ are needed to represent such short lifetimes. A fit of the decay curve of the $(11/2)_1^- \to (7/2)_1^-$ transition presented in Fig. 6 in Paper 4, results in $\tau_{(11/2)_1^-} = 0.54(23)$ ps, which is consistent with the result found in Ref. [64].
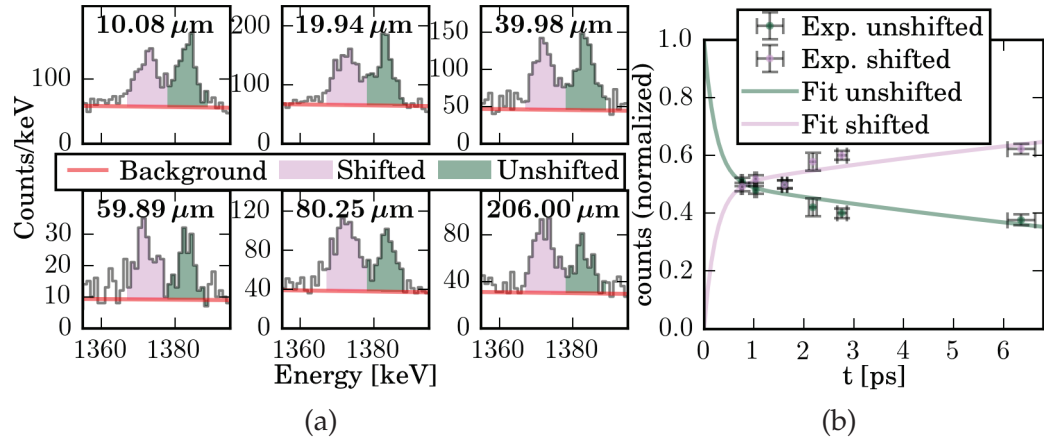
Figure 5.17: In a), the $(9/2)_1^- \to (7/2)_1^-$ transition at 1383 keV γ energy in ^{63}Co. In b), the decay curves used to extract the lifetime of the $(9/2)_1^-$ state in ^{63}Co.

In ^{61}Co, the $(11/2)_1^- \to (9/2)_1^-$ transition at 1664 keV (see Fig. 5 in Paper 4), was used to investigate the lifetime of the $(11/2)_1^-$ state. The feeding observed from $(13/2)_1^- \to (11/2)_1^-$ was included in the fit. Although the statistics was not sufficient to extract a precise value of the lifetime, an upper limit of 2 ps could be deduced. The $B(E2; 11/2_1^- \to 7/2_1^-)$ in ^{61,63}Co obtained in this work, presented in Fig. 8 in Paper 4 supports the interpretation of the $7/2^-$ proton hole in cobalt coupled to the 2^+ in the corresponding nickel isotope.

^{59}Mn

The $(11/2)_1^- \to (7/2)_1^-$ transition [65] at 1189 keV γ energy in ^{59}Mn, shown in Fig. 5 in Paper 4 was used to fit the lifetime of the $(11/2)_1^-$ state. The fit with a long lived unseen feeder, displayed in Fig. 6 in Paper 4 resulted in $\tau_{(11/2)_1^-} = 2.65(30)$ ps with $\chi^2/N_{\rm dof} = 0.59$. Comparing this result to the $(11/2)_1^- \to (7/2)_1^-$ transition in ^{55}Mn [66], there are no experimental signs of increased collectivity for increasing neutron number.

^{65}Ni

Fig. 5.18a shows the spectra of the $(11/2)_1^+ \rightarrow (9/2)_1^+$ transition [67] at 1169 keV γ energy in ^{65}Ni. The exponential fit resulted in $\tau_{(11/2)_1^+} = 0.83(13)$ ps with $\chi^2/N_{\text{dof}} = 2.04$ (see Fig. 5.18b). The corresponding transition has previously been investigated in ^{63}Ni [68] resulting in 5.2(8) ps for the γ line of 892 keV and in ^{61}Ni [69] resulting in 0.87^{+30}_{-15} ps for the γ line of 1177 keV. The $(9/2)_1^+$ state in these isotopes is interpreted as the coupling of a $g_{9/2}$ neutron to the $A - 1$ core. Such a coupling has been observed in several nuclei in the $A \approx 60$ region [68]. Assuming a simple quadrupole-quadrupole interaction between the core and the neutron, a $\Delta J = 1$ or 2 band is built upon the $(9/2)^+$ state. In the case of the ^{61,63,65}Ni isotopes, it is a strongly coupled $\Delta J = 1$ band due to the positive quadrupole moment of the 2_1^+ state in the $A - 1$ core [70, 71].
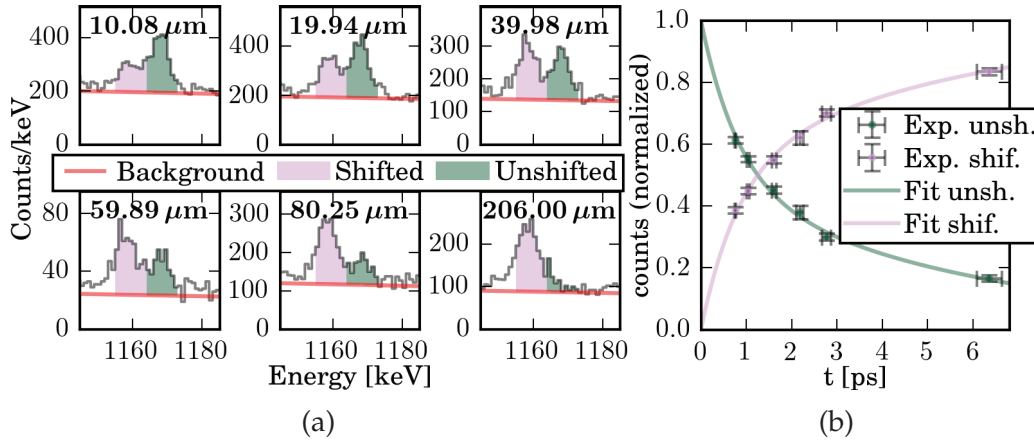

Figure 5.18: The spectra of ^{65}Ni (in a) and the decay curves (in b)), used to extract the lifetime from the $(11/2)_1^+ \rightarrow (9/2)_1^+$ transition at 1169 keV γ energy.

Chapter 6

Bragg detectors

A common problem with radioactive beam experiments is the beam contamination. In the Coulomb excitation experiment presented in Chapter 3 the laser ionization scheme was used to select ^{140}Sm from the cocktail of fragments produced in the primary target. However, in many radioactive beam experiments, where ions cannot be selected as precisely as for the ^{140}Sm case, the yield of unwanted species may be high compared to the yield of the desired ions. After applying electromagnetic filters the problem of isobaric contamination remains. In such cases a Bragg-Curve detector used for heavy ion charge identification is an approach to identify the beam components. A Bragg detector used in Coulomb excitation experiments can also provide a direct measurement of the energy loss of the beam in the target. In this way the uncertainty from theoretical approximations in the calculations of the energy loss can be avoided.

In this chapter, the assembling and testing of a Bragg detector for heavy ion identification in Coulomb excitation and transfer reactions is described. The work was performed at Oak Ridge National Laboratory, Tennessee, USA. One of the benefits of the detector tested in this project is its small size, allowing for easier transportation to other laboratories, such as Argonne National Laboratory, USA, where it may be used at the Californium Rare Isotope Breeder Upgrade (CARIBU) facility. The chapter begins with an introduction to Bragg detectors in Section 6.1, followed by a description of the assembling of the detector in Section 6.2, the testing of the DAQ in Section 6.3 and the calculations and simulations of the detector response in Section 6.4. Finally, the test experiments and analysis are described in Sections 6.5 and 6.6 respectively.

6.1   Bragg detectors

The energy loss of charged particles in matter is governed by the Bethe-Bloch formula, in Eq. (6.1) [9],

$$\frac{dE}{dx} = -\left(\frac{e^2}{4\pi\epsilon_0}\right)^2 \frac{4\pi z^2 N_0 Z \rho}{mc^2\beta^2 A} \left[ln\left(\frac{2mc^2\beta^2}{I}\right) - ln(1-\beta^2) - \beta^2\right], \quad (6.1)$$

where β is the velocity of the particle, c is the speed of light in vacuum and ze is the electric charge of the particle. Z is the atomic number of the target, A is the atomic number, ρ is the density of the target and m is the electron mass, N_0 is Avogadros' number and I is the mean excitation energy of the atomic electrons.

The energy loss as a function of the penetrating distance of the particles in matter, is called Bragg curve. When $\beta \rightarrow 0$, the energy loss reaches its maximum amplitude, resulting in the characteristic Bragg peak, as seen in Fig. 6.1. The amplitude of the Bragg peak is approximately proportional to the nuclear charge, Z, thus the nuclear charge can be obtained by integration of an electronic signal that reflects the shape of the Bragg curve. The initial particle energy is given by the integral over the total range of the Bragg curve. To obtain a Bragg peak 1A MeV minimum energy of the particle is needed. However, also for lower energies the shape of the curve contains information about the energy and Z [72].
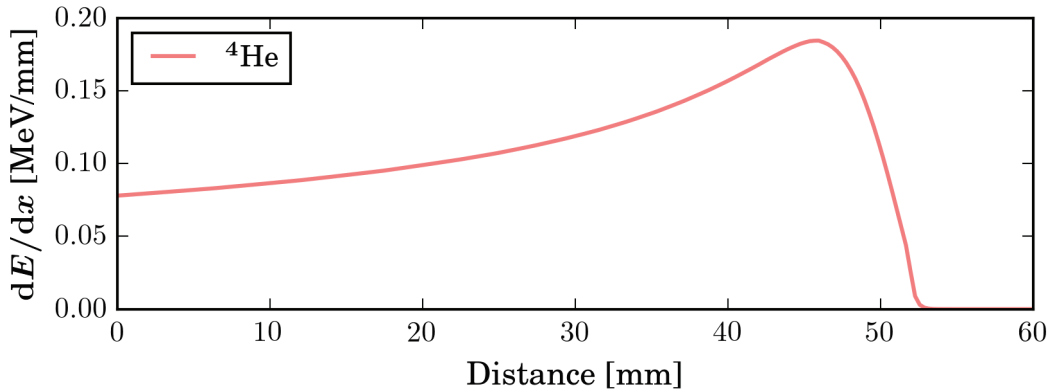
Figure 6.1: The energy loss as a function of penetrating distance of particles in matter is called Bragg curve. When $\beta \rightarrow 0$, the energy loss reaches its maximum amplitude, resulting in a characteristic Bragg peak. The amplitude is approximately proportional to the nuclear charge.

A Bragg detector is an ionization chamber with the electric field applied parallel to the particle trajectory [73]. This geometry allows for

a continuous readout, giving the range of the particles [74]. Furthermore, the Z information of the curve is independent of the range of the particles. The Z of the particle could be obtained with analog electronics. For example, using two shaping amplifiers with one long and one short integration time constants. The long signal is proportional to the total energy loss and the short one is proportional to the nuclear charge of the ions and gives the energy loss at the Bragg-peak maximum [75]. A schematic drawing of the Bragg detector is shown in Fig. 6.2. Electrons coming from the ionization process travel to a Frisch grid that prevents the movements of the electrons to induce a current in the anode until they have passed the grid. The resistors for a voltage divider serve to keep the field homogeneous. In a time interval, Δt, the electrons move from the grid to the anode. The distance between the grid and the anode has to be short to properly reproduce the full Bragg curve but long enough to achieve sufficient screening efficiency [76].
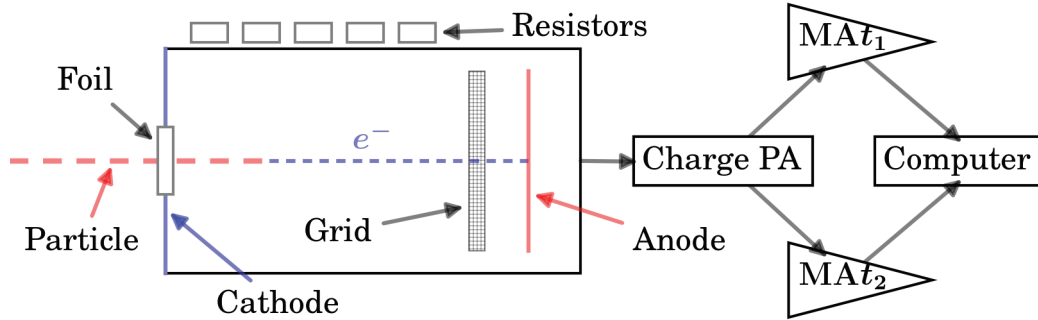
Figure 6.2: Schematic drawing of the Bragg detector using analog electronics. Charged particles ionize the gas and the free electrons drift in the electric field towards the anode. The grid before the anode prevents the movements of the electrons to induce a current in the anode until they have passed the grid. After the pre-amplifier (*PA*), the pulse-shaping is done using two main amplifiers (*MA*) with different time constants. The resistors serve to keep the field homogeneous.

The electron charge collected by the anode is proportional to the specific ionization along the track, $\frac{\Delta Q}{\Delta x}$, given in Eq. (6.2).

$$\frac{\Delta Q}{\Delta t} = \frac{\Delta Q}{\Delta x} \cdot V_D \qquad (6.2)$$

Here V_D is the drift velocity that is assumed to be constant in an homogeneous electric field [76].

6.2   Assembling of the Bragg detector

The parts of the unassembled Bragg detector at ORNL are seen in Fig. 6.3.

Figure 6.3: The unassembled Bragg detector.

To minimize the energy loss in the entrance foil of the detector, a window of 500 nm thick and 25 mm^2 silicon nitride on a 100 mm^2 silicon frame was made. The advantages of this window were the uniformity, the thin size and the capability to resist the pressure up to 0.5 atm. The distance between the window and the anode was 132.2 mm while the space between the grid and anode was 4.8 mm. Due to its fast drift velocity and non-flammable properties CF_4 was chosen as filling gas at a pressure between $150 - 200$ Torr. The detector mounted in to the beam line at ORNL, is seen in Fig. 6.4. A linear feature was made to mount the target.
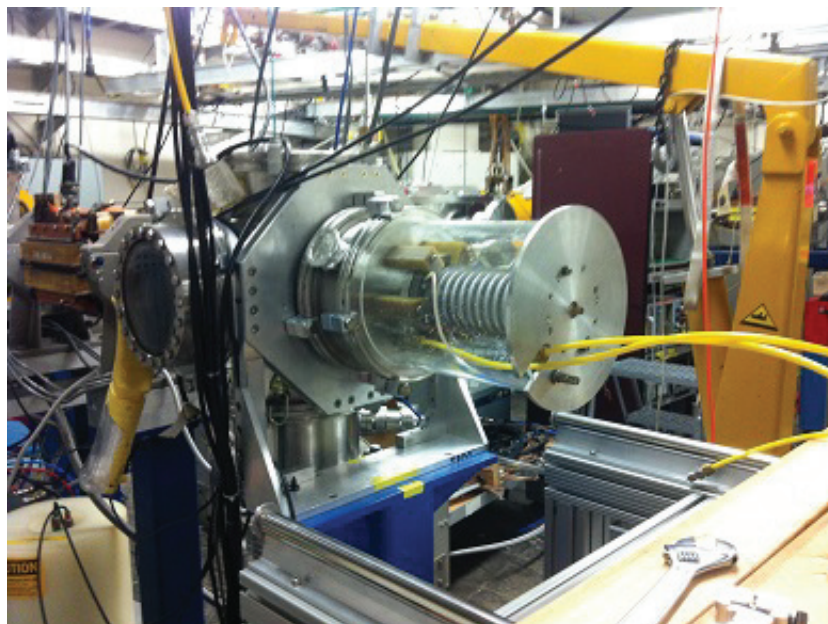
Figure 6.4: The Bragg detector assembled and mounted into the test beam line at ORNL. A linear feature used to mount the target is shown on the left-hand side.

6.3 Testing of DAQ

Three different approaches for the digitization of the signal for future experiments were tested. The first one was performed using a Multichannel Analyzer (MCA8000A) from the Amptek company, allowing to sort the heights from a shaped amplified signal, the second one using CAEN digitizers (DT5740C and DT7520A) and in the third one the LabView software was used to save the signal from an Agilent (DSO7104A) oscilloscope. The advantage of the MCA system is that the energy signal is directly obtained. On the other hand, the CAEN instruments are capable of providing the full Bragg curve, which could also be obtained using the oscilloscope as digitizer, but with insufficient resolution. The testing procedures are described in steps below.

- Approach 1. The signal from an ORTEC pulse generator was divided and coupled to a DSO7104A oscilloscope and an ORTEC amplifier. Then the shaped signal from the shaper was connected to the oscilloscope and the width of the shaped signal was set to 10 μs and the height was 4 V. The output from the shaper was coupled to the MCA8000A and from the MCA to the PC. To display the signal,

the `Amptek ADMCA Analog and digital acquisition` software was used. The frequency was limited to 2 particles per second, because a too high frequency resulted in a very noisy spectrum.

- Approach 2. The output from the pulse generator was connected to the CAEN digitizer and from the CAEN digitizer to the PC. Here the sampling frequency of the digitizer was 62.5 MS/s and the CAEN SCOPE software was used to study and save the traces of the signal.

- Approach 3. The output from the oscilloscope was connected directly to the PC and controlled by a LabView program, shown in Appendix B. This program displays the spectrum and updates it with a sampling frequency of 10 MS/s to get a continuous spectrum and saves the data to text files. Furthermore, it is possible to set and control the trigger slope and trigger level.

The spectra obtained using approach 2 and 3 are shown in Fig. 6.5
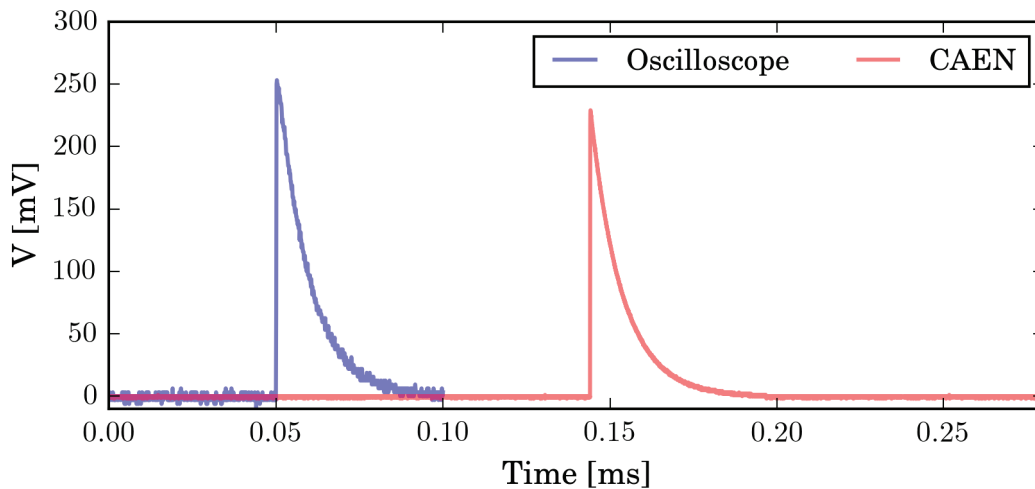

Figure 6.5: Example of the pulse shape obtained with the CAEN digitizer and the oscilloscope. The higher sampling frequency and greater number of FADC bits of the CAEN modules resulted in a significantly cleaner signal.

6.4 Calculations

To predict the response of the Bragg detector, energy losses of various ions in the silicon nitride window and the CF_4 gas at different beam energies

and gas pressures were calculated, using the SRIM code. Energy losses per nucleon for ^{74}Ge, ^{120}Sn, ^{152}Sm and ^{238}U in 500 nm silicon nitride as a function of beam energy per nucleon are shown in Fig. 6.6. The
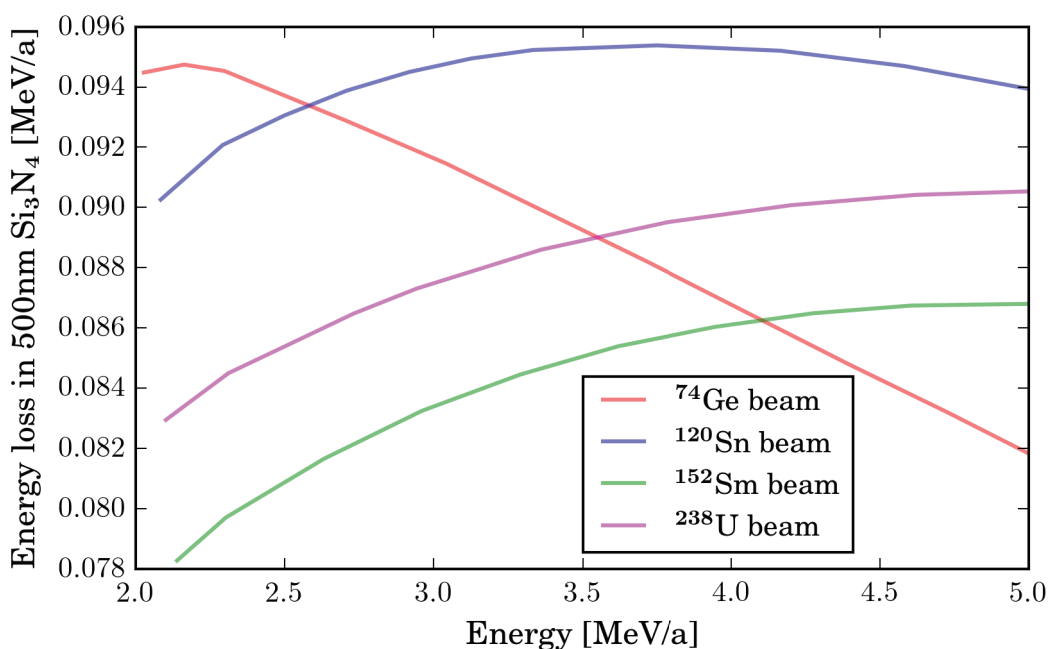
Figure 6.6: Energy losses per nucleon for ^{74}Ge, ^{120}Sn, ^{152}Sm and ^{238}U in 500 nm silicon nitride as a function of beam energy. For ^{74}Ge, ^{120}Sn the maximum energy loss is reached at 2.2A MeV and 3.7A MeV respectively.

maximum energy loss for ^{74}Ge and ^{120}Sn is reached at 2.2A MeV and 3.7A MeV respectively. For the heavier ions the peak is reached for energies larger than 5A MeV.

For ions traveling in matter, the mean distance that the ions travel along a straight axis before stopping, is called projected range. The projected range for ^{74}Ge, ^{120}Sn, ^{152}Sm and ^{238}U going though the window and entering the filling gas, is shown in Fig. 6.7, for the operating gas pressure of 100, 150 and 200 Torr. To obtain the Bragg peak, the ions have to be fully stopped within the detector. Therefore the detector length of 13.2 cm sets a limit on the beam energy. The lighter the beam is, the higher energy per nucleon can be used, for a fixed gas pressure.

While using the Bragg detector for charged particle identification, the possibility of separating two nuclei with neighboring proton number is crucial. Therefore the energy losses for ^{10}Be, ^{10}B, ^{59}Ni, ^{59}Co, ^{238}U and ^{238}Pu in CF_4 gas, calculated using the SRIM code were compared and are presented in Fig. 6.8, as a function of distance traveled in the detector. It
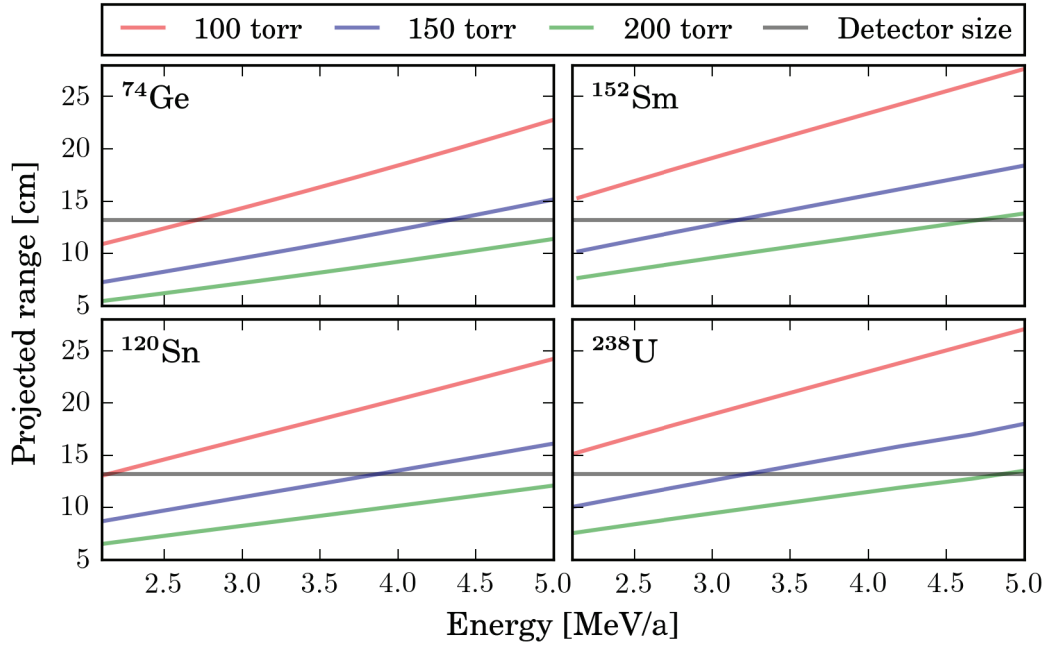
Figure 6.7: The projected range for ^{74}Ge, ^{120}Sn, ^{152}Sm and ^{238}U for operating gas pressure of 100, 150 and 200 Torr. The black line shows the dimension limit of the Bragg detector. The lighter the beam is, the higher energy per nucleon, for the same gas pressure can be used.

is seen that the separation is smaller with increasing Z, from ^{10}Be-^{10}B to ^{59}Ni-^{59}Co. The unexpectedly good separation between the heaviest nuclei is likely due to bad accuracy in the SRIM calculations for heavy ions.
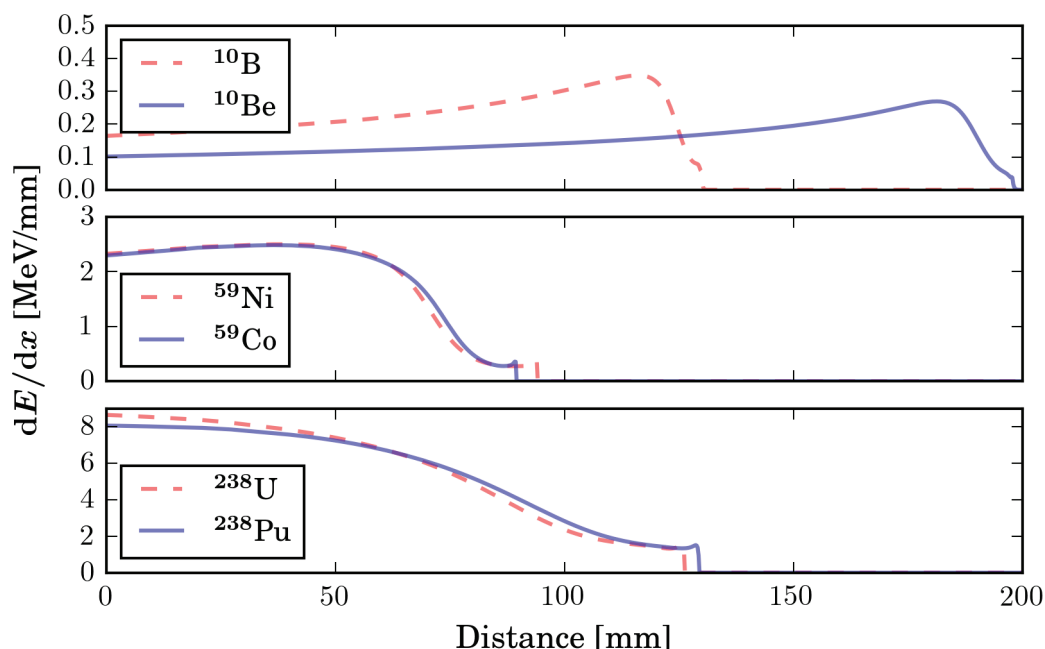
Figure 6.8: Energy loss of ^{10}Be, ^{10}B, ^{59}Ni, ^{59}Co,^{238}U and ^{238}Pu, as a function of distance in CF_4 gas, from the SRIM code calculations. It is seen that the separation becomes worse with increasing Z number, from ^{10}Be-^{10}B to ^{59}Ni-^{59}Co. The unexpectedly good separation between the heavier nucleus is likely due to bad accuracy in the SRIM calculations for heavy ions.

6.5 Test experiment

The first test of the Bragg detector was performed at Oak Ridge National Laboratory, USA, using a ^{244}Cm α source, followed by an in-beam run. The simulated Bragg Curve for α particles with an energy of 6 MeV in CF_4 gas at 150 Torr, is seen in Fig. 6.1. A voltage of 2060 V was applied to the Bragg detector.

In the stable beam test of the Bragg detector, ^{63}Cu beam of 100 MeV energy was used on three different targets:

1. $1.55 mg/cm^2$ ^{208}Pb+$40\mu g/cm^2$ ^{12}C

2. $6\mu g/cm^2$ ^{27}Al+$1mg/cm^2$ ^{208}Pb+$40\mu g/cm^2$ ^{12}C

3. $1189\mu g/cm^2$ ^{12}C

This experiment allowed to measure the target thicknesses, using the traces from the Bragg detector. For the calibration purpose ^{63}Cu beam

with energy of 67.0, 82.7 and 100 MeV were used without any target. The count rate was about 800 counts per second.

6.6 Data analysis

The traces from a typical event detected in the Bragg detector is shown in Fig. 6.9. The total energy was obtained by integrating the area under the
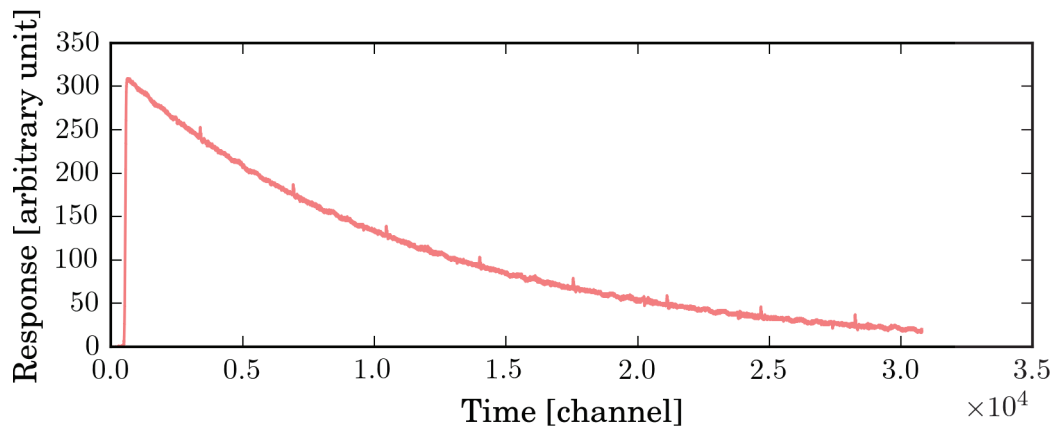
Figure 6.9: The traces from a typical event detected in the Bragg detector

peak, while the energy loss is proportional to the peak amplitude. A linear energy calibration was performed using the data taken without using the target, as shown in Fig. 6.10. Total energy spectra from the test of the Bragg
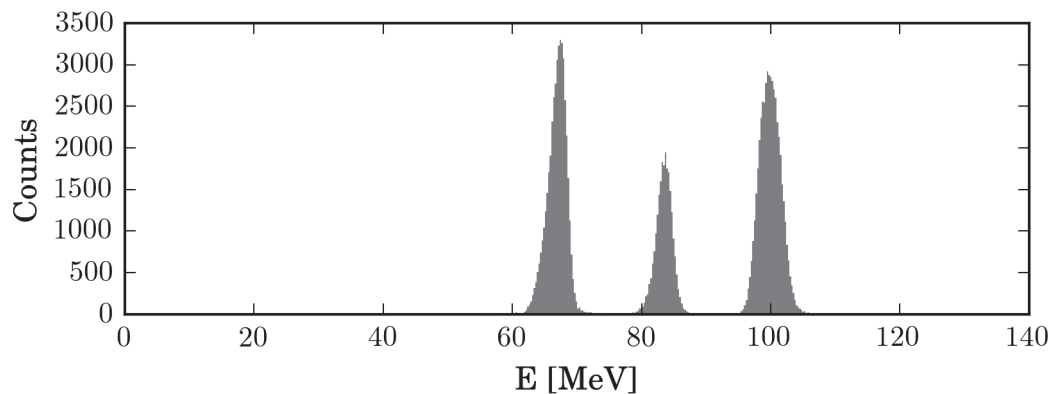
Figure 6.10: Linear energy calibration from the data acquired without the target foil.

detector using ^{63}Cu beam on three different targets are shown in Fig. 6.11.
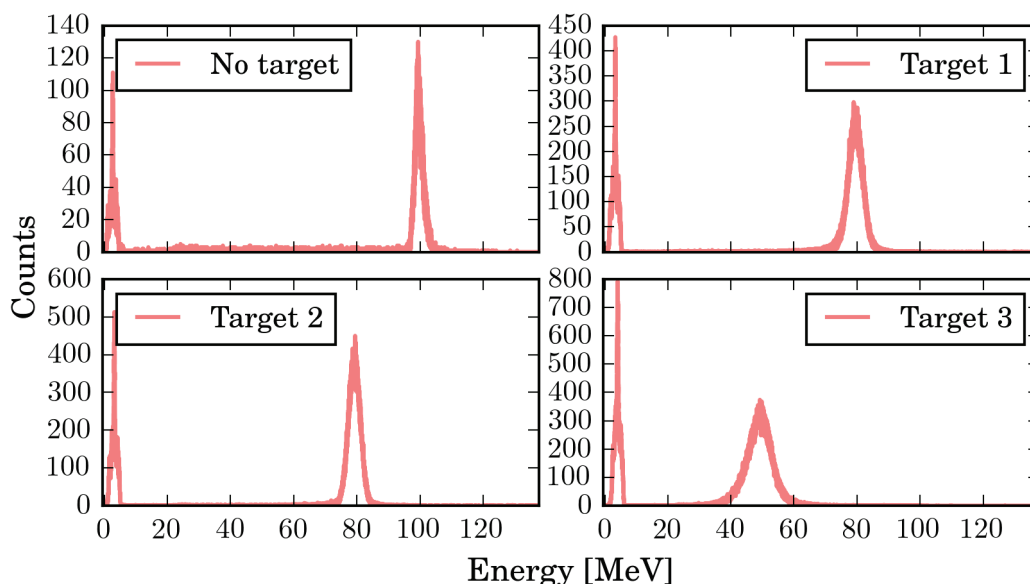
Figure 6.11: Total energy spectra from the test of the Bragg detector using a ^{63}Cu beam on three different targets, compared to the spectrum obtained without target.

For target number 1 and 3 the energy loss from SRIM calculations are less than 1% higher than the measured values, while calculated values for target 2 are 30% higher than the measurement. The result for target 2 may be due to the uncertainty in the SRIM calculations or incorrect specification of the target thickness.

The particle identification plot (PID), with the energy loss, dE, obtained by measuring the amplitude of the traces from the Bragg detector, versus the total energy, E, is shown in Fig. 6.12. By projecting the spectra in the direction shown, the main peak from ^{63}Cu can be separated from the contaminant. The contaminant seen in this experiment has a lower Z and its origin is unknown.
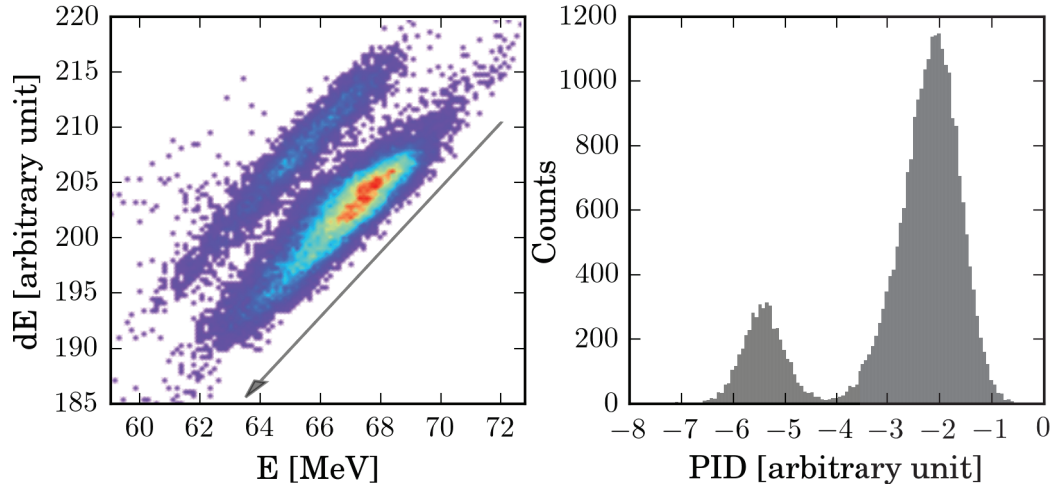
Figure 6.12: The particle identification plot (PID), with the energy loss, dE, vs total energy, E. By projecting the spectra along the direction of the arrow, the main peak from ^{63}Cu can be separated from the contaminant.

6.7 Future application

^{12}C+^{12}C $\rightarrow$ ^{23}Na+p reaction

A possible future application for the Bragg detector is the cross section measurement of the ^{12}C+^{12}C $\rightarrow$ ^{23}Na+p reaction, important from the astrophysical point of view. With ^{12}C beam and CH_4 filled gas detector, the Bragg Curve for a produced ^{23}Na would be clearly distinguishable from the Bragg curve of ^{12}C. Here, the digitizing of the signal becomes important.

Simulations of the reaction and the detector response were performed, using SRIM and MATLAB programs. Starting with a ^{12}C beam of 30 MeV energy, the remaining energy at a distance, d from the entrance of the detector was computed. Relativistic two-body reaction kinematic was used to obtain the energy of ^{23}Na, assuming a center of mass angle of 30°. The stopping power for ^{23}Na as a function of distance from the entrance of the gas detector, for various reaction locations is shown in Fig. 6.13 together with the stopping power for ^{12}C. It is seen that ^{23}Na and ^{12}C are clearly distinguishable.

The detection of ^{23}Na (or ^{22}Ne from the ^{12}C+^{12}C $\rightarrow$ ^{22}Ne+^{2}He reaction) needs to be separated from pileup events in the detector. This may be done using the angular dependence of the detected particle energy. The PACE4 [77] Monte Carlo simulations were used to simulate ^{12}C+^{12}C
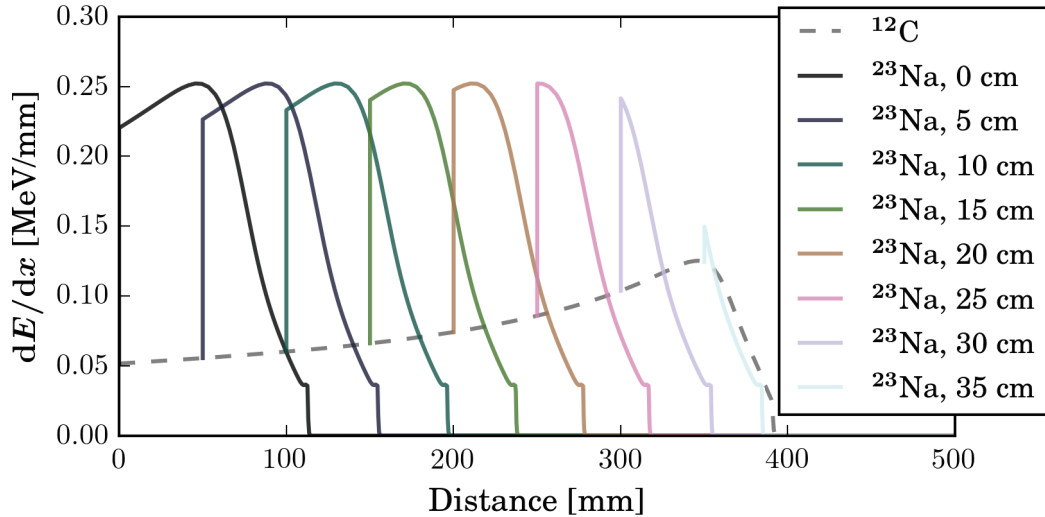
Figure 6.13: The stopping power for ^{23}Na as a function of distance from the entrance of the gas detector, for various reaction locations, together with the stopping power from the SRIM simulations. It is seen that ^{23}Na and ^{12}C are clearly distinguishable.

reaction, and in Fig. 6.14 the particle energy is shown as a function of scattering angle.

The performance of the Bragg detector is promising and a proposal has been approved by the ANL PAC to determine the feasibility of absolute cross-section measurements at CARIBU by measuring the beam composition of a few select beams with the new EBIS source. With the old ECR source the RIBs are heavily contaminated and the beam composition varies depending on the previous history of the source. The proposed experiment aims to accurately measure the beam composition, including isomeric components and to establish the precision with which this can be done in an experiment.
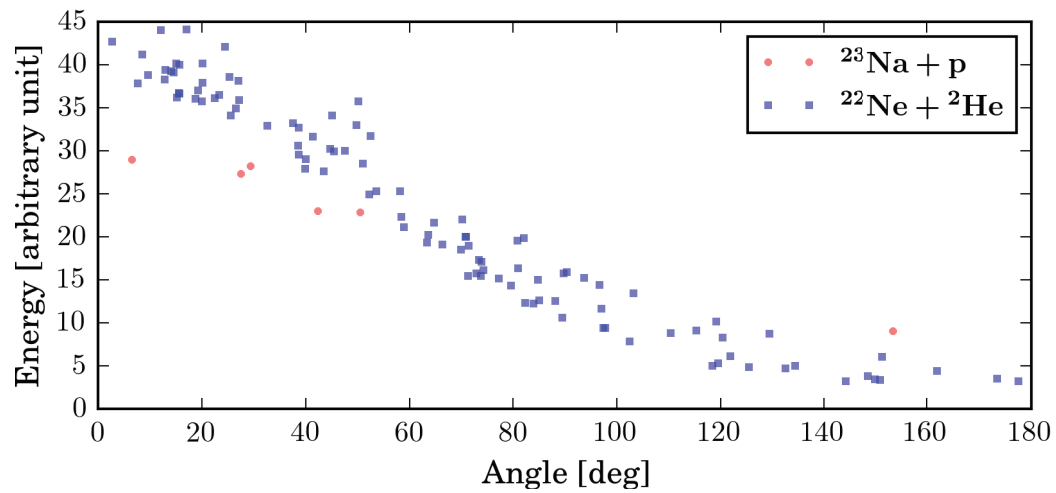
Figure 6.14: PACE4 Monte Carlo calculations applied to simulate the ^{12}C+^{12}C reaction. The particle energy is shown as a function of scattering angle. The angular dependence can be used to distinguish ^{23}Na and ^{22}Ne nuclei from pileups in the Bragg detector.

Chapter 7

Papers

The following papers are included in this thesis:

1. M. Klintefjord, K. Hadyńska-Klęk, J. Samorajczyk, A. Görgen, C. Droste, J. Srebrny, T. Abraham, F.L. Bello Garrote, F. Giacoppo, E. Grodner, P. Hoff, M. Kisieliński, M. Komorowska, W. Korten, M. Kowalczyk, J. Kownacki, A.C Larsen, T. Marchlewski, P. Napiorkowski, T. Renstrøm, B.Siebeck, S. Siem, R. Szenborn, A. Tucholski, P. Thöle, T. Tornyi, G.M. Tveten, M. Zielińska and the MINIBALL and ISOLDE collaborations *Spectroscopy of lowlying states in* ^{140}Sm Acta Phys. Pol. B 46, 607 (2015)

2. J. Samorajczyk, M. Klintefjord, C. Droste, A. Görgen, T. Marchlewski, J. Srebrny, T. Abraham, F. L. B. Garrote, E. Grodner, K. Hadyńska-Klęk, M. Kisieliński, M. Komorowska, M. Kowalczyk, J. Kownacki, P. Napiorkowski, R. Szenborn, A. Stolarz, A. Tucholski, and G. M. Tveten *Revised spin values of the* 991 *keV and* 1599 *keV levels in* ^{140}Sm, Phys. Rev. C 92, 044322 (2015).

3. M. Klintefjord, Hadyńska-Klęk, A. Görgen, C. Bauer, F.L. Bello Garrote, S. Bönig, B. Bounthong, A. Damyanova, J.-P. Delaroche, V. Fedosseev, D.A. Fink, F. Giacoppo, M. Girod, P. Hoff, N. Imai, W. Korten, A.C. Larsen, J. Libert, R. Lutter, B.A. Marsh, P.L. Molkanov, H. Naïdja, P. Napiorkowski, F. Nowacki, J. Pakarinen, E. Rapisarda, P. Reiter, T. Renstrøm, S. Rothe, M.D. Seliverstov, B. Siebeck, S. Siem, J. Srebrny, T. Stora, P. Thöle, T.G. Tornyi, G.M. Tveten, P. Van Duppen, M.J Vermeulen, D. Voulot, N. Warr, F. Wenander, H. De Witte, and M. Zielińska *The structure of low-lying states in* ^{140}Sm *studied by Coulomb excitation* Phys. Rev. C 93, 054303 (2016)

4. M. Klintefjord, J. Ljungvall, A. Görgen, F.L. Bello Garrote, A. Blazhev, E. Clemént, G. de France, J.-P. Delaroche, P. Désesquelles, A. Dewald, D. Doherty, C. Fransen, A. Gengelbach, G. Georgiev, M. Girod, A. Goasduff, A. Gottardo, K. Hadyńska-Klęk, S. Kaim, T. Konstantinopoulos, A. Korichi, W. Korten, A. Lemasson, S.M. Lenzi, A. Lopez-Martens, C. Michelagnoli, A. Navin, J. Nyberg, R. Perez, M. Rejmund, S. Roccia, E. Sahin, I. Stefan, A.E. Stuchbery, and M. Zielińska *Measurement of lifetimes in $^{62,64}Fe$, $^{61,63}Co$ and ^{59}Mn* In preparation.

7.1 Brief introduction to the papers

Paper 1 and 2:

The spin and parity of the excited states at 991 keV and 1599 keV excitation energy in ^{140}Sm were investigated in a study of the β decay from ^{140}Eu produced in the ^{112}Cd(^{32}S,p3n) reaction at 155 MeV, at the Heavy Ion Laboratory, Warsaw, Poland. The $\gamma - \gamma$ angular correlation method was applied, resulting in the revised spin assignment of the states at 991 keV and 1599 keV excitation energy, to 2^+ and $0^{(+)}$, respectively. These new findings, together with preliminary results of the Coulomb excitation experiment of ^{140}Sm performed at ISOLDE, CERN, Geneva, Switzerland are presented in Paper 1 and the details of the angular correlation analysis is given in Paper 2.

The author of this thesis was the main responsible for the analysis presented in and the writing of Paper 1. The author performed the analysis described in Paper 2, in collaboration with *J. Samorajczyk*, participated in the preparation and performing of the experiment and contributed to the writing of the paper.

Paper 3:

This paper describes the Coulomb excitation experiment of ^{140}Sm on ^{94}Mo target, performed at CERN-ISOLDE, Geneva, Switzerland. Transition strengths and quadrupole moments are extracted for low-lying excited states in ^{140}Sm. The results indicating a weak quadrupole deformation with maximum triaxiality and significant γ softness, are compared to and well reproduced by shell model and beyond mean filed calculation. The nucleus also exhibits several features expected at the E(5) critical point symmetry.

The author of this thesis performed the analysis presented in the paper and is the main author of the paper.

Paper 4:

In this paper the recoil distance Doppler shift experiment performed at Ganil, Caen, France, using ^{238}U beam on ^{64}Ni target with the purpose of studying the lifetime of excited states in the ≈ 60 region, is presented. The lifetime of the 4_1^+ state in ^{62}Fe, the $11/2_1^-$ state in ^{63}Co and $11/2_1^-$ state in ^{59}Mn were extracted. In addition, upper limits of the 4_1^+ state in ^{64}Fe and the $11/2_1^-$ state in ^{61}Co were obtained. The experimental results are compared to shell model and beyond mean filed caluclation.

The author of this thesis participated in the preparation and running of the experiment, performed the analysis and is the main author of the paper.

Appendices

Appendix A

GOSIA minimization input files

```
OP,FILE
4,3,1    ! OUTPUT: OP,CORR, INPUT: OP,MAP, OP,MINI, OP,
   ↪ ERRO[diagonal,corr]
140Sm.cor
7,3,1    ! OUTPUT: OP,MAP, INPUT: OP,MINI, OP,ERRO[
   ↪ diagonal,corr]
140Sm.map
8,3,1 ! OUTPUT: OP,GDET (if first value in OP,GDET is
   ↪ negative) INPUT: OP,RAW
140Sm_94Mo.raw
9,3,1 ! OUTPUT: OP,GDET (GE detector information (
   ↪ solid angle attenuation factors)), INPUT: OP,
   ↪ YIEL, OP,INTI, OP,MAP, OP,MINI, OP,ERRO[diagonal
   ↪ ,corr]
140Sm_94Mo.gdt
11,3,2    ! OUTPUT: OP,MINI, INPUT: OP,ERRO[diagonal,
   ↪ corr]
crf.dat
12,3,1    ! OUTPUT: OP,MINI, INPUT: OP,ERRO[diagonal,
   ↪ corr]
140Sm.bst
14,3,1
internal_mini.14
22,3,1    ! output file
140Sm_mini.out
0,0,0
OP,TITL
```

```
Automatically generated file
OP,GOSI ! GOSIA − Information about the nucleus ,same
    ↪ syntax as OP,COUL
LEVE ! Level scheme for this nucleus
1 ,1 ,0 ,0
2 ,1 ,2 ,0.531
3 ,1 ,4 ,1.246  !4 ,1 ,6 ,2.082
4 ,1 ,2 ,0.990  !7 ,1 ,2 ,1.599
0 ,0 ,0 ,0
ME    ! Matrix elements
2 ,0 ,0 ,0 ,0
1 ,2 ,1.1103221725969883 ,0.0001 ,2  ! 0_1+ −> 2_1+ E2 ,
    ↪ Spectroscopic data
1 ,4 ,1.0000000000000001E−005 ,0.00001 ,2  ! 0_1+ −> 2_2+
    ↪ E2
2 ,2 ,4.2814786346808464E−002 ,−5 ,5  ! 2_1+ QM
2 ,3 ,1.6314480213705642 ,0.00001 ,5  ! 2_1+ −> 4_1+ E2
2 ,4 ,1.3299578486891102 ,0.00001 ,5  ! 2_1+ −> 2_2+ E2
    ↪ !3 ,−3 ,.0414 ,2 ,2  !3 ,−4 ,1.6792 ,2 ,3
7 ,0 ,0 ,0 ,0
2 ,4 ,0.10000000000000001 ,0.00001 ,0.1  ! 2_1+ −> 2_2+ M1
0 ,0 ,0 ,0 ,0
EXPT ! Experimental parameters
5 ,62 ,140 ! Number of experiments ,nucleus−Z, nucleus−A
−42 ,94 ,350 ,26.1 ,3 ,1 ,0 ,0 ,360 ,1 ,1
−42 ,94 ,350 ,29.5 ,3 ,1 ,0 ,0 ,360 ,1 ,1  ! Zn ,An ,Ep ,th_lab ,Mc,
    ↪ Ma ,IAX ,phi1 ,phi2 ,IKIN ,LN
−42 ,94 ,350 ,33.4 ,3 ,1 ,0 ,0 ,360 ,1 ,1  ! Zn<0 means
    ↪ projectile excited ,otherwise target
−42 ,94 ,350 ,38.2 ,3 ,1 ,0 ,0 ,360 ,1 ,1 ! Ep beam energy after
    ↪ losses ,in MeV
−42 ,94 ,350 ,40.9 ,3 ,1 ,0 ,0 ,360 ,1 ,1
CONT
EFF ,5
1  0
2  0
3  0
4  0
5  0
SMR,
SPL ,1.
```

```
WRN,3 .
PRT,
2 ,0
4 ,0
5 ,1
13  0
14  0
16  0
5  1
12  0
18  1
0 ,0
END,                           ! The blank  line  below  is
   ↪ neccessary

OP,YIEL ! Yields
1  ! IFLAG,1 = correct  angular  distribution  of gammas
   ↪ due  to  finite  distance  traveled  by  decaying
   ↪ nucleus ,0 = no correction
11,1 ! N1,N2: number  of energies  and  multipolarities
   ↪ to  define  internal  conversion  coefficients ,N1 <
   ↪ 0 means  take  values  from OP,BRIC−calculation
0.056 ,0.103 ,0.165 ,0.2 ,0.25 ,0.3 ,0.35 ,0.45 ,0.65 ,1.0 ,1.3
   ↪ ! N1 energy  mesh  points  in MeV
2  ! I1 ,This  and  the  next  line  repeated  N2 times ,I1 =
   ↪ multipolarity
21.4 ,2.1 ,0.4 ,0.209 , 0.1001 , 0.0562 , 0.0352 , 0.0171 ,
   ↪ 0.0066 , 0.0025 , 0.00141 ! Internal  conversion
   ↪ coefficients  for  I1 ,at  energies  specified  above
21,21,21,21,21 ! Number  of detectors  for  each
   ↪ experiment ,minus  means  same  setup  as  previous
1, 2, 3, 4, 5, 6, 7, 8, 9, 10, 11, 12, 13, 14, 15, 16,
   ↪  17, 18, 19, 20, 21 ! Physical  detector  IDs used
   ↪  for  this  experiment
108.5 ,126.6 ,134.0 , 60.1 , 71.4 , 44.1 , 65.7 , 38.5 ,
   ↪ 57.2 ,111.2 ,126.2 ,137.9 , 42.4 , 67.5 ,
   ↪ 49.0 ,123.5 ,132.1 ,106.4 , 43.2 , 69.3 , 52.6 ! theta
   ↪ −values  for  the  detectors
133.7 ,157.0 ,122.2 , 58.9 , 31.6 , 30.4 ,117.7 ,
   ↪ 120.0 ,147.4 , 36.8 , 63.1 , 29.4 ,
   ↪ 242.0 ,228.5 ,204.6 , 339.9 , 307.4 , 316.8 , 341.0 ,
```

```
↪ 330.9, 306.0 ! phi−values for the detectors
1, 2, 3, 4, 5, 6, 7, 8, 9, 10, 11, 12, 13, 14, 15, 16,
    ↪  17, 18, 19, 20, 21
108.5,126.6,134.0, 60.1, 71.4, 44.1, 65.7, 38.5,
    ↪ 57.2,111.2,126.2,137.9, 42.4, 67.5,
    ↪ 49.0,123.5,132.1,106.4, 43.2, 69.3, 52.6
133.7,157.0,122.2, 58.9, 31.6, 30.4,117.7,
    ↪ 120.0,147.4, 36.8, 63.1, 29.4,
    ↪ 242.0,228.5,204.6, 339.9, 307.4, 316.8, 341.0,
    ↪ 330.9, 306.0
1, 2, 3, 4, 5, 6, 7, 8, 9, 10, 11, 12, 13, 14, 15, 16,
    ↪  17, 18, 19, 20, 21
108.5,126.6,134.0, 60.1, 71.4, 44.1, 65.7, 38.5,
    ↪ 57.2,111.2,126.2,137.9, 42.4, 67.5,
    ↪ 49.0,123.5,132.1,106.4, 43.2, 69.3, 52.6
133.7,157.0,122.2, 58.9, 31.6, 30.4,117.7,
    ↪ 120.0,147.4, 36.8, 63.1, 29.4,
    ↪ 242.0,228.5,204.6, 339.9, 307.4, 316.8, 341.0,
    ↪ 330.9, 306.0
1, 2, 3, 4, 5, 6, 7, 8, 9, 10, 11, 12, 13, 14, 15, 16,
    ↪  17, 18, 19, 20, 21
108.5,126.6,134.0, 60.1, 71.4, 44.1, 65.7, 38.5,
    ↪ 57.2,111.2,126.2,137.9, 42.4, 67.5,
    ↪ 49.0,123.5,132.1,106.4, 43.2, 69.3, 52.6
133.7,157.0,122.2, 58.9, 31.6, 30.4,117.7,
    ↪ 120.0,147.4, 36.8, 63.1, 29.4,
    ↪ 242.0,228.5,204.6, 339.9, 307.4, 316.8, 341.0,
    ↪ 330.9, 306.0
1, 2, 3, 4, 5, 6, 7, 8, 9, 10, 11, 12, 13, 14, 15, 16,
    ↪  17, 18, 19, 20, 21
108.5,126.6,134.0, 60.1, 71.4, 44.1, 65.7, 38.5,
    ↪ 57.2,111.2,126.2,137.9, 42.4, 67.5,
    ↪ 49.0,123.5,132.1,106.4, 43.2, 69.3, 52.6
133.7,157.0,122.2, 58.9, 31.6, 30.4,117.7,
    ↪ 120.0,147.4, 36.8, 63.1, 29.4,
    ↪ 242.0,228.5,204.6, 339.9, 307.4, 316.8, 341.0,
    ↪ 330.9, 306.0
2,1 ! NS1,NS2: The transition from the state with
    ↪ index NS1 to the state with index NS2 is used
    ↪ for normalization
```

```
1 ! Number of data−sets for experiment 1,equal to
   ↪ number of detectors ,unless detector clusters
   ↪ were specified in OP,RAW. This and the rest of
   ↪ the input is only needed if OP,GOSI was
   ↪ previously specified . If OP,COUL was specified
   ↪ earlier ,then this and the rest is not needed .
1000.0 ! Upper limits for the detectors
328.6 ! Relative normalization factors for detectors
1 ! The three lines above repeated for each experiment
1000.0
256.4
1
1000.0
186.1
1
1000.0
116.3
1
1000.0
98.6
4 ! NTAP,must be 3 if OP,CORR is used ,and must be 4 if
   ↪  OP,ERRO or OP,MINI is used
0 ,0
0 ,0
0 ,0
1 ,1
2 ,1 ,2 ,1.111501834181912507e+00 ,3.028487362382849268e
   ↪ −02
OP,REST
0 ,0
OP,RAW ! Raw,uncorrected gamma yields ,i .e. yields not
   ↪ corrected for detector efficiencies . Also ,yields
   ↪  from several detectors can be summed to a
   ↪ cluster yield .
1 ! Index of experiment to consider
4.5317 ,−0.2219 ,−0.05166 ,0 ,0 ,0 ,0 ,0   ! −114.43847765677,
   ↪  77.4777358306356, −19.3895913343855,
   ↪ 2.13070402056655, −0.08736, 0, 0−999 or 4.5317,
   ↪ −0.2219, −0.05166 ,0 ,0 ,0 ,0 ,0... 0.0, 0.0, 0.0,
   ↪ 0.0, 0.0, 0.0, 1.0, 1.0
```

```
4.5317,−0.2219,−0.05166,0,0,0,0,0  ! Efficieny
  ↪ parameters for logical detector 1 (logical
  ↪ detectors defined in OP,YIEL),as defined in
  ↪ GREMLIN. The values are a0,a1,a2,a3,f,N,b,c (see
  ↪  page 281)
4.5317,−0.2219,−0.05166,0,0,0,0,0
4.5317,−0.2219,−0.05166,0,0,0,0,0
4.5317,−0.2219,−0.05166,0,0,0,0,0
4.5317,−0.2219,−0.05166,0,0,0,0,0
4.5317,−0.2219,−0.05166,0,0,0,0,0
4.5317,−0.2219,−0.05166,0,0,0,0,0
4.5317,−0.2219,−0.05166,0,0,0,0,0
4.5317,−0.2219,−0.05166,0,0,0,0,0
4.5317,−0.2219,−0.05166,0,0,0,0,0
4.5317,−0.2219,−0.05166,0,0,0,0,0
4.5317,−0.2219,−0.05166,0,0,0,0,0
4.5317,−0.2219,−0.05166,0,0,0,0,0
4.5317,−0.2219,−0.05166,0,0,0,0,0
4.5317,−0.2219,−0.05166,0,0,0,0,0
4.5317,−0.2219,−0.05166,0,0,0,0,0
4.5317,−0.2219,−0.05166,0,0,0,0,0
4.5317,−0.2219,−0.05166,0,0,0,0,0
4.5317,−0.2219,−0.05166,0,0,0,0,0
1 ! Number of clusters
21 ! Number of gamma detectors for cluster 1
1,2,3,4,5,6,7,8,9,10,11,12,13,14,15,16,17,18,19,20,21
  ↪ ! List of gamma detectors for cluster 1
2 ! Next experiment,same syntax as for the first
  ↪ experiment
4.5317,−0.2219,−0.05166,0,0,0,0,0  ! −114.43847765677,
  ↪  77.4777358306356, −19.3895913343855,
  ↪ 2.13070402056655, −0.08736, 0, 0−999 or 4.5317,
  ↪ −0.2219, −0.05166,0,0,0,0,0... 0.0, 0.0, 0.0,
  ↪ 0.0, 0.0, 1.0, 1.0
4.5317,−0.2219,−0.05166,0,0,0,0,0  ! Efficieny
  ↪ parameters for logical detector 1 (logical
  ↪ detectors defined in OP,YIEL),as defined in
  ↪ GREMLIN. The values are a0,a1,a2,a3,f,N,b,c (see
  ↪  page 281)
4.5317,−0.2219,−0.05166,0,0,0,0,0
```

```
4.5317,−0.2219,−0.05166,0,0,0,0,0
4.5317,−0.2219,−0.05166,0,0,0,0,0
4.5317,−0.2219,−0.05166,0,0,0,0,0
4.5317,−0.2219,−0.05166,0,0,0,0,0
4.5317,−0.2219,−0.05166,0,0,0,0,0
4.5317,−0.2219,−0.05166,0,0,0,0,0
4.5317,−0.2219,−0.05166,0,0,0,0,0
4.5317,−0.2219,−0.05166,0,0,0,0,0
4.5317,−0.2219,−0.05166,0,0,0,0,0
4.5317,−0.2219,−0.05166,0,0,0,0,0
4.5317,−0.2219,−0.05166,0,0,0,0,0
4.5317,−0.2219,−0.05166,0,0,0,0,0
4.5317,−0.2219,−0.05166,0,0,0,0,0
4.5317,−0.2219,−0.05166,0,0,0,0,0
4.5317,−0.2219,−0.05166,0,0,0,0,0
4.5317,−0.2219,−0.05166,0,0,0,0,0
4.5317,−0.2219,−0.05166,0,0,0,0,0
4.5317,−0.2219,−0.05166,0,0,0,0,0
1
21
1,2,3,4,5,6,7,8,9,10,11,12,13,14,15,16,17,18,19,20,21
3
4.5317,−0.2219,−0.05166,0,0,0,0,0   ! −114.43847765677,
   ↪   77.4777358306356,  −19.3895913343855,
   ↪  2.13070402056655,  −0.08736, 0, 0−999 or 4.5317,
   ↪   −0.2219,  −0.05166,0,0,0,0,0... 0.0, 0.0, 0.0,
   ↪  0.0, 0.0, 1.0, 1.0
4.5317,−0.2219,−0.05166,0,0,0,0,0   ! Efficieny
   ↪  parameters for logical detector 1 (logical
   ↪  detectors defined in OP,YIEL),as defined in
   ↪  GREMLIN. The values are a0,a1,a2,a3,f,N,b,c (see
   ↪   page 281)
4.5317,−0.2219,−0.05166,0,0,0,0,0
4.5317,−0.2219,−0.05166,0,0,0,0,0
4.5317,−0.2219,−0.05166,0,0,0,0,0
4.5317,−0.2219,−0.05166,0,0,0,0,0
4.5317,−0.2219,−0.05166,0,0,0,0,0
4.5317,−0.2219,−0.05166,0,0,0,0,0
4.5317,−0.2219,−0.05166,0,0,0,0,0
4.5317,−0.2219,−0.05166,0,0,0,0,0
4.5317,−0.2219,−0.05166,0,0,0,0,0
```

```
4.5317,−0.2219,−0.05166,0,0,0,0,0
4.5317,−0.2219,−0.05166,0,0,0,0,0
4.5317,−0.2219,−0.05166,0,0,0,0,0
4.5317,−0.2219,−0.05166,0,0,0,0,0
4.5317,−0.2219,−0.05166,0,0,0,0,0
4.5317,−0.2219,−0.05166,0,0,0,0,0
4.5317,−0.2219,−0.05166,0,0,0,0,0
4.5317,−0.2219,−0.05166,0,0,0,0,0
4.5317,−0.2219,−0.05166,0,0,0,0,0
4.5317,−0.2219,−0.05166,0,0,0,0,0
1
21
1,2,3,4,5,6,7,8,9,10,11,12,13,14,15,16,17,18,19,20,21
4
4.5317,−0.2219,−0.05166,0,0,0,0,0   ! −114.43847765677,
   ↪   77.4777358306356,  −19.3895913343855,
   ↪  2.13070402056655,  −0.08736, 0, 0−999 or 4.5317,
   ↪  −0.2219,  −0.05166,0,0,0,0,0... 0.0,  0.0,  0.0,
   ↪  0.0,  0.0,  1.0,  1.0
4.5317,−0.2219,−0.05166,0,0,0,0,0   ! Efficieny
   ↪ parameters for logical detector 1 (logical
   ↪ detectors defined in OP,YIEL),as defined in
   ↪ GREMLIN. The values are a0,a1,a2,a3,f,N,b,c (see
   ↪  page 281)
4.5317,−0.2219,−0.05166,0,0,0,0,0
4.5317,−0.2219,−0.05166,0,0,0,0,0
4.5317,−0.2219,−0.05166,0,0,0,0,0
4.5317,−0.2219,−0.05166,0,0,0,0,0
4.5317,−0.2219,−0.05166,0,0,0,0,0
4.5317,−0.2219,−0.05166,0,0,0,0,0
4.5317,−0.2219,−0.05166,0,0,0,0,0
4.5317,−0.2219,−0.05166,0,0,0,0,0
4.5317,−0.2219,−0.05166,0,0,0,0,0
4.5317,−0.2219,−0.05166,0,0,0,0,0
4.5317,−0.2219,−0.05166,0,0,0,0,0
4.5317,−0.2219,−0.05166,0,0,0,0,0
4.5317,−0.2219,−0.05166,0,0,0,0,0
4.5317,−0.2219,−0.05166,0,0,0,0,0
4.5317,−0.2219,−0.05166,0,0,0,0,0
4.5317,−0.2219,−0.05166,0,0,0,0,0
4.5317,−0.2219,−0.05166,0,0,0,0,0
```

```
4.5317,−0.2219,−0.05166,0,0,0,0,0
4.5317,−0.2219,−0.05166,0,0,0,0,0
1
21
1,2,3,4,5,6,7,8,9,10,11,12,13,14,15,16,17,18,19,20,21
5 ! Index of experiment to consider
4.5317,−0.2219,−0.05166,0,0,0,0,0  ! −114.43847765677,
   ↪  77.4777358306356, −19.3895913343855,
   ↪ 2.13070402056655, −0.08736, 0, 0−999 or 4.5317,
   ↪ −0.2219, −0.05166,0,0,0,0,0... 0.0, 0.0, 0.0,
   ↪ 0.0, 0.0, 1.0, 1.0
4.5317,−0.2219,−0.05166,0,0,0,0,0  ! Efficieny
   ↪ parameters for logical detector 1 (logical
   ↪ detectors defined in OP,YIEL),as defined in
   ↪ GREMLIN. The values are a0,a1,a2,a3,f,N,b,c (see
   ↪  page 281)
4.5317,−0.2219,−0.05166,0,0,0,0,0
4.5317,−0.2219,−0.05166,0,0,0,0,0
4.5317,−0.2219,−0.05166,0,0,0,0,0
4.5317,−0.2219,−0.05166,0,0,0,0,0
4.5317,−0.2219,−0.05166,0,0,0,0,0
4.5317,−0.2219,−0.05166,0,0,0,0,0
4.5317,−0.2219,−0.05166,0,0,0,0,0
4.5317,−0.2219,−0.05166,0,0,0,0,0
4.5317,−0.2219,−0.05166,0,0,0,0,0
4.5317,−0.2219,−0.05166,0,0,0,0,0
4.5317,−0.2219,−0.05166,0,0,0,0,0
4.5317,−0.2219,−0.05166,0,0,0,0,0
4.5317,−0.2219,−0.05166,0,0,0,0,0
4.5317,−0.2219,−0.05166,0,0,0,0,0
4.5317,−0.2219,−0.05166,0,0,0,0,0
4.5317,−0.2219,−0.05166,0,0,0,0,0
4.5317,−0.2219,−0.05166,0,0,0,0,0
4.5317,−0.2219,−0.05166,0,0,0,0,0
4.5317,−0.2219,−0.05166,0,0,0,0,0
1 ! Number of clusters
21 ! Number of gamma detectors for cluster 1
1,2,3,4,5,6,7,8,9,10,11,12,13,14,15,16,17,18,19,20,21
   ↪ ! List of gamma detectors for cluster 1
0 ! 0 means no more experiments
```

```
OP,MINI ! IMODE,NPTL,CHILIM,CONV,TEST,LOCKF,NLOCK,IFBL
    ↪ ,LOCKS,DLOCK
2100 50 1e−5 1e−7 1.1 1 0 1 0 0.001 ! NPTL = max #
    ↪ steps ,CHILIM = convergence limit
OP,EXIT
```
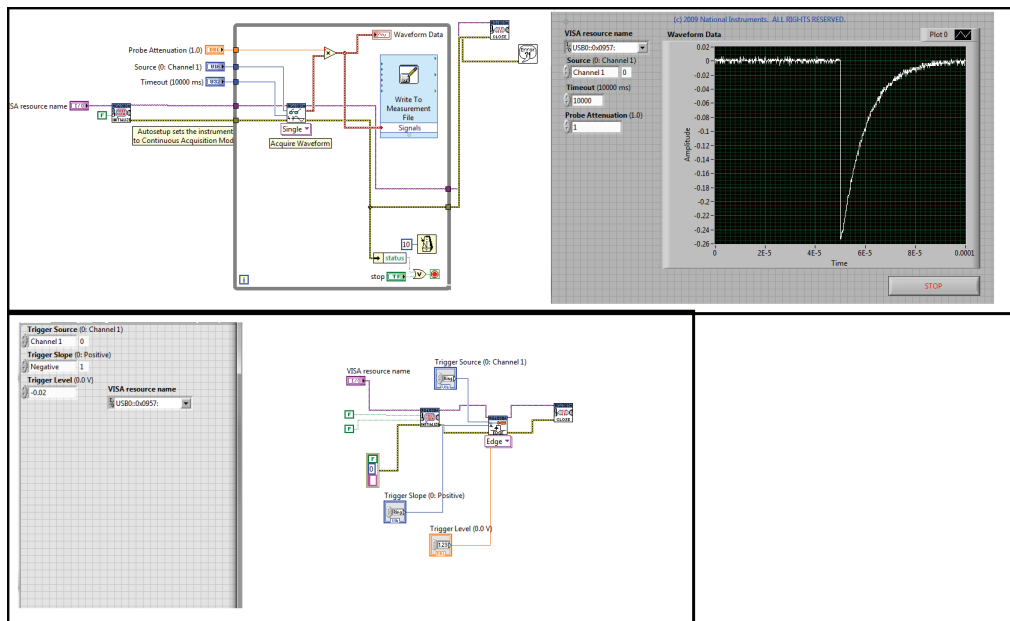
Appendix B

Labview program

Figure B.1: The program in the upper part displays the single spectra in the `single box`. The loop updates the spectrum with a sampling frequency of 10 MS/s to get a continuous spectrum. With the `Write to Measurement box` the spectra is saved to text files. The program in the lower part sets the trigger slope and trigger level.

Bibliography

[1] S. Hilaire and M. Girod, "Large-scale mean-field calculations from proton to neutron drip lines using the D1S Gogny force," *Eur. Phys. J. A* **33** no. 2, (2007) 237–241.

[2] A. Bohr and B. Mottelson, *Nuclear Structure, Volume I: Single-Particle Motion*. Nuclear Structure. World Scientific, 1998. `http://www.worldscientific.com/worldscibooks/10.1142/3530-vol1`.

[3] A. Bohr and B. Mottelson, *Nuclear Structure, Volume II: Nuclear Deformations*. Nuclear Structure. World Scientific, 1998. `http://www.worldscientific.com/worldscibooks/10.1142/3530-vol2`.

[4] K. Alder and A. Winther, *Electromagnetic excitation: theory of Coulomb excitation with heavy ions*. North-Holland Pub. Co., 1975.

[5] B. R. Mottelson, "Collective Motion in the Nucleus," *Rev. Mod. Phys.* **29** (Apr, 1957) 186–190.

[6] A. Davydov and G. Filippov, "Rotational states in even atomic nuclei," *Nucl. Phys.* **8** (1958) 237–249.

[7] L. Wilets and M. Jean, "Surface Oscillations in Even-Even Nuclei," *Phys. Rev.* **102** (May, 1956) 788–796.

[8] J. L. Wood and K. Heyde, "A focus on shape coexistence in nuclei," *J. Phys. G* **43** no. 2, (2016) 020402.

[9] K. Krane, *Introductory Nuclear Physics*. Wiley, 1987. `http://eu.wiley.com/WileyCDA/WileyTitle/productCd-047180553X.html`.

[10] B. Pritychenko, J. Choquette, M. Horoi, B. Karamy, and B. Singh, "An update of the B(E2) evaluation for $0_1^+ \rightarrow 2_1^+$ transitions in even–even nuclei near $N \sim Z \sim 28$," *At. Data. Nucl. Data Tables* **98** no. 4, (2012) 798 − 811.

[11] K. Langanke, J. Maruhn, and S. Koonin, *Computational Nuclear Physics 1: Nuclear Structure*. Computational Nuclear Physics. Springer Berlin Heidelberg, 1991.

[12] R. Machleidt, "High-precision, charge-dependent Bonn nucleon-nucleon potential," *Phys. Rev. C* **63** (Jan, 2001) 024001.

[13] J. Negele and E. Vogt, *Advances in Nuclear Physics*. No. v. 27 in Advances in Nuclear Physics.

[14] J. P. Elliott, "The interacting boson model of nuclear structure," *Rep. Prog. Phys.* **48** no. 2, (1985) 171.

[15] P. Ring and P. Schuck, *The Nuclear Many-Body Problem*. Springer-Verlag Berlin Heidelberg, 1980.

[16] J. Dechargé and D. Gogny, "Hartree-Fock-Bogolyubov calculations with the D1 effective interaction on spherical nuclei," *Phys. Rev. C* **21** (Apr, 1980) 1568–1593.

[17] J. Berger, M. Girod, and D. Gogny, "Time-dependent quantum collective dynamics applied to nuclear fission," *Comput. Phys. Commun.* **63** no. 1–3, (1991) 365 – 374.

[18] J. Libert, M. Girod, and J.-P. Delaroche, "Microscopic descriptions of superdeformed bands with the Gogny force: Configuration mixing calculations in the $A \sim$190 mass region," *Phys. Rev. C* **60** (Sep, 1999) 054301.

[19] D. Cline, H. Gertzman, H. Gove, P. Lesser, and J. Schwartz, "The static quadrupole moment of the first excited state of 60Ni," *Nucl. Phys. A* **133** no. 2, (1969) 445 – 464.

[20] T. Czosnyka, D. Cline, and C. Wu, "Internal laboratory report UR/NSRL 308/1986," *Bull. Am. Phys. Soc.* **28** (1983) 745.

[21] A. Dewald, O. Möller, and P. Petkov, "Developing the Recoil Distance Doppler-Shift technique towards a versatile tool for lifetime measurements of excited nuclear states," *Prog. Part. Nucl. Phys.* **67** no. 3, (2012) 786 – 839.

[22] P. Haustein, H. Taylor, R. McPherson, and R. Fairchild, "A tabulation of gamma-gamma directional-correlation coefficients for states of high angular momenta," *At. Data. Nucl. Data Tables* **10** no. 4, (1972) 321 – 467.

[23] K. Siegbahn, *Alpha-,Beta-, and Gamma-Ray Spectroscopy (Part2)*. NorthHolland, 1968.

[24] G. Knoll, *Radiation Detection and Measurement*. John Wiley & Sons, 2010. `http://eu.wiley.com/WileyCDA/WileyTitle/productCd-EHEP001606.html`.

[25] N. Warr, J. Van de Walle, M. Albers, F. Ames, B. Bastin, C. Bauer, V. Bildstein, A. Blazhev *et al.*, "The Miniball spectrometer," *Eur. Phys. J. A* **49** no. 3, (2013) .

[26] S. Akkoyun, A. Algora, B. Alikhani, F. Ameil, G. de Angelis, L. Arnold, A. Astier, A. Ataç *et al.*, "AGATA—Advanced GAmma Tracking Array," *Nucl. Instr. Meth. Phys. Res. A* **668** (2012) 26 – 58.

[27] W. Kane and M. Mariscotti, "An empirical method for determining the relative efficiency of a Ge(Li) gamma-ray detector," *Nucl. Instr. Meth.* **56** no. 2, (1967) 189 – 196.

[28] A. N. Andreyev, M. Huyse, P. Van Duppen, L. Weissman, D. Ackermann, J. Gerl, F. P. Hessberger, S. Hofmann *et al.*, "A triplet of differently shaped spin-zero states in the atomic nucleus," *Nature* **405** no. 6785, (May, 2000) 430–433.

[29] N. Bree, K. Wrzosek-Lipska, A. Petts, A. Andreyev, B. Bastin, M. Bender, A. Blazhev, B. Bruyneel *et al.*, "Shape Coexistence in the Neutron-Deficient Even-Even $^{182-188}$Hg Isotopes Studied via Coulomb Excitation," *Phys. Rev. Lett.* **112** (Apr, 2014) 162701.

[30] M. A. Cardona, S. Lunardi, D. Bazzacco, G. de Angelis, and V. Roca, "Shape coexistence in ^{140}Sm and the onset of deformation below N =82 from lifetime measurements," *Phys. Rev. C* **44** (Aug, 1991) 891–894.

[31] R. B. Firestone, J. Gilat, J. M. Nitschke, P. A. Wilmarth, and K. S. Vierinen, "Decay studies of neutron deficient nuclei near the Z =64 subshell: ^{142}Dy, ^{140,142}Tb, ^{140,142}Gd, ^{140,142}Eu, ^{142}Sm, and ^{142}Pm," *Phys. Rev. C* **43** (Mar, 1991) 1066–1085.

[32] B. D. Kern, R. L. Mlekodaj, G. A. Leander, M. O. Kortelahti, E. F. Zganjar, R. A. Braga, R. W. Fink, C. P. Perez *et al.*, "Transition through triaxial shapes of the light samarium isotopes and the beta decay of ^{136,138,140}Eu," *Phys. Rev. C* **36** (Oct, 1987) 1514–1521.

[33] J. Samorajczyk, M. Klintefjord, C. Droste, A. Görgen,
     T. Marchlewski, J. Srebrny, T. Abraham, F. L. B. Garrote *et al.*,
     "Revised spin values of the 991 keV and 1599 keV levels in ^{140}Sm,"
     Phys. Rev. C **92** (Oct, 2015) 044322.

[34] O. Kester, T. Sieber, S. Emhofer, F. Ames, K. Reisinger, P. Reiter,
     P. Thirolf, R. Lutter *et al.*, "Accelerated radioactive beams from
     REX-ISOLDE," *Nucl. Instr. Meth. Phys. Res. B* **204** (2003) 20 – 30. 14th
     International Conference on Electromagnetic Isotope Separators and
     Techniques Related to their Applications.

[35] V. Fedosseev, L.-E. Berg, N. Lebas, O. Launila, M. Lindroos,
     R. Losito, B. Marsh, F. Österdahl *et al.*, "ISOLDE RILIS: New beams,
     new facilities," *Nucl. Instr. Meth. Phys. Res. B* **266** no. 19–20, (2008)
     4378–4382. Proceedings of the XVth International Conference on
     Electromagnetic Isotope Separators and Techniques Related to their
     Applications.

[36] F. Schwellnus, R. Catherall, B. Crepieux, V. Fedosseev, B. Marsh,
     C. Mattolat, M. Menna, F. Österdahl *et al.*, "Study of low work
     function materials for hot cavity resonance ionization laser ion
     sources," *Nucl. Instr. Meth. Phys. Res. B* **267** no. 10, (2009) 1856–1861.

[37] P. Schmidt, F. Ames, G. Bollen, O. Forstner, G. Huber, M. Oinonen,
     and J. Zimmer, "Bunching and cooling of radioactive ions with
     REXTRAP," *Nucl. Phys. A* **701** no. 1–4, (2002) 550 – 556. 5th
     International Conference on Radioactive Nuclear Beams.

[38] F. Wenander, "EBIS as charge breeder for radioactive ion beam
     accelerators," *Nucl. Phys. A* **701** no. 1–4, (2002) 528 – 536. 5th
     International Conference on Radioactive Nuclear Beams.

[39] A. Ostrowski, S. Cherubini, T. Davinson, D. Groombridge, A. Laird,
     A. Musumarra, A. Ninane, A. di Pietro *et al.*, "CD: A double sided
     silicon strip detector for radioactive nuclear beam experiments,"
     Nucl. Instr. Meth. Phys. Res. A **480** no. 2–3, (2002) 448–455.

[40] C. Bauer. Private communication, 2012.

[41] O. Niedermaier. Private communication, 2012.

[42] O. Tarasov and D. Bazin, "LISE++: Radioactive beam production
     with in-flight separators," *Nucl. Instr. Meth. Phys. Res. B* **266**
     no. 19–20, (2008) 4657 – 4664.

[43] N. Kesteloot, B. Bastin, L. P. Gaffney, K. Wrzosek-Lipska, K. Auranen, C. Bauer, M. Bender, V. Bildstein *et al.*, "Deformation and mixing of coexisting shapes in neutron-deficient polonium isotopes," *Phys. Rev. C* **92** (Nov, 2015) 054301.

[44] F. L. Bello Garrote, A. Görgen, J. Mierzejewski, C. Mihai, J. P. Delaroche, M. Girod, J. Libert, E. Sahin *et al.*, "Lifetime measurement for the 2_1^+ state in ^{140}Sm and the onset of collectivity in neutron-deficient Sm isotopes," *Phys. Rev. C* **92** (Aug, 2015) 024317.

[45] J. F. Ziegler, M. Ziegler, and J. Biersack, "SRIM – The stopping and range of ions in matter (2010)," *Nucl. Instr. Meth. Phys. Res. B* **268** no. 11–12, (2010) 1818 – 1823. 19th International Conference on Ion Beam Analysis.

[46] T. Kibédi, T. Burrows, M. Trzhaskovskaya, P. Davidson, and C. N. Jr., "Evaluation of theoretical conversion coefficients using BrIcc," *Nucl. Instr. Meth. Phys. Res. A* **589** no. 2, (2008) 202 – 229.

[47] MATLAB, *version 8.6 (R2015b)*. The MathWorks Inc., Natick, Massachusetts, 2015.

[48] J. Mierzejewski, A. A. Pasternak, M. Komorowska, J. Srebrny, E. Grodner, and M. Kowalczyk, "The COMPA manual," tech. rep., Heavy Ion Laboratory, University of Warsaw, Poland, 2015. latest version available online at `http://www.slcj.uw.edu.pl/˜jmierz/compa.pdf`.

[49] National Nuclear Data Center. information extracted from the Chart of Nuclides database [2015, Dec. 3]. `http://www.nndc.bnl.gov/chart`.

[50] J. Mierzejewski, J. Srebrny, H. Mierzejewski, J. Andrzejewski, W. Czarnacki, C. Droste, E. Grodner, A. Jakubowski *et al.*, "EAGLE the central European Array for Gamma Levels Evaluation at the Heavy Ion Laboratory of the University of Warsaw," *Nucl. Instr. Meth. Phys. Res. A* **659** no. 1, (2011) 84 – 90.

[51] A. P. Zuker, "Three-Body Monopole Corrections to Realistic Interactions," *Phys. Rev. Lett.* **90** (Jan, 2003) 042502.

[52] C. Thibault, R. Klapisch, C. Rigaud, A. M. Poskanzer, R. Prieels, L. Lessard, and W. Reisdorf, "Direct measurement of the masses of

^{11}Li and $^{26-32}$Na with an on-line mass spectrometer," *Phys. Rev. C* **12** (Aug, 1975) 644–657.

[53] B. H. Wildenthal and W. Chung, "Collapse of the conventional shell-model ordering in the very-neutron-rich isotopes of Na and Mg," *Phys. Rev. C* **22** (Nov, 1980) 2260–2262.

[54] E. K. Warburton, J. A. Becker, and B. A. Brown, "Mass systematics for A =29–44 nuclei: The deformed $A \sim$32 region," *Phys. Rev. C* **41** (Mar, 1990) 1147–1166.

[55] A. Brown, "Viewpoint: Islands of insight in the nuclear chart," *Physics* **3** no. 104, (2010) .

[56] J. Ljungvall, A. Görgen, A. Obertelli, W. Korten, E. Clément, G. de France, A. Bürger, J.-P. Delaroche *et al.*, "Onset of collectivity in neutron-rich Fe isotopes: Toward a new island of inversion?," *Phys. Rev. C* **81** (Jun, 2010) 061301.

[57] S. Pullanhiotan, M. Rejmund, A. Navin, W. Mittig, and S. Bhattacharyya, "Performance of VAMOS for reactions near the Coulomb barrier," *Nucl. Instr. Meth. Phys. Res. A* **593** no. 3, (2008) 343 – 352.

[58] W. H. Press, S. A. Teukolsky, W. T. Vetterling, and B. P. Flannery, *Numerical Recipes in C (2Nd Ed.): The Art of Scientific Computing*. Cambridge University Press, New York, NY, USA, 1992. `http://apps.nrbook.com/c/index.html`.

[59] J. Ljungvall. Private communication, 2015.

[60] B. Singh, "Nuclear Data Sheets for A = 64," *Nucl. Data Sheets* **108** no. 2, (2007) 197 – 364.

[61] S. Agostinelli, J. Allison, K. Amako, J. Apostolakis, H. Araujo, P. Arce, M. Asai, D. Axen *et al.*, "Geant4—a simulation toolkit," *Nucl. Instr. Meth. Phys. Res. A* **506** no. 3, (2003) 250 – 303.

[62] E. Browne and J. Tuli, "Nuclear Data Sheets for A = 60," *Nucl. Data Sheets* **114** no. 12, (2013) 1849 – 2022.

[63] N. Hoteling, C. J. Chiara, R. Broda, W. B. Walters, R. V. F. Janssens, M. Hjorth-Jensen, M. P. Carpenter, B. Fornal *et al.*, "Structure of ^{60,62}Fe and the onset of $\nu g_{9/2}$ occupancy," *Phys. Rev. C* **82** (Oct, 2010) 044305.

[64] V. Modamio, J. J. Valiente-Dobón, S. Lunardi, S. M. Lenzi, A. Gadea, D. Mengoni, D. Bazzacco, A. Algora *et al.*, "Lifetime measurements in neutron-rich ^{63,65}Co isotopes using the AGATA demonstrator," *Phys. Rev. C* **88** (Oct, 2013) 044326.

[65] J. J. Valiente-Dobón, S. M. Lenzi, S. J. Freeman, S. Lunardi, J. F. Smith, A. Gottardo, F. D. Vedova, E. Farnea *et al.*, "Spectroscopy of neutron-rich $^{59-63}$Mn isotopes," *Phys. Rev. C* **78** (Aug, 2008) 024302.

[66] A. M. Nathan, J. W. Olness, E. K. Warburton, and J. B. McGrory, "Yrast decay schemes from heavy ion + ^{48}Ca fusion-evaporation reactions. I. $^{54-56}$Mn, ^{56}Cr, and $^{52-53}$V," *Phys. Rev. C* **16** (Jul, 1977) 192–214.

[67] T. Anfinsen, K. Bjørndal, A. Graue, J. Lien, G. Sandvik, L. Tveita, K. Ytterstad, and E. Cosman, "Nuclear reaction studies in the nickel isotopes: The 62Ni(d, p)63Ni and 64Ni(d, p)65Ni reactions," *Nucl. Phys. A* **157** no. 2, (1970) 561 – 576.

[68] E. K. Warburton, J. W. Olness, A. M. Nathan, and A. R. Poletti, "Yrast decay schemes from heavy-ion + ^{48}Ca fusion-evaporation reactions: IV: ^{53}Cr, ^{54}V, ^{62}Co, and $^{61-63}$Ni," *Phys. Rev. C* **18** (Oct, 1978) 1637–1650.

[69] R. Wadsworth, G. D. Jones, A. Kogan, P. R. G. Lornie, T. Morrison, O. Mustaffa, H. G. Price, D. Simister *et al.*, "Gamma ray spectroscopy in 61Ni-levels above 2.2 MeV in excitation," *J. Phys. G* **3** no. 6, (1977) 833.

[70] P. Lesser, D. Cline, C. Kalbach-Cline, and A. Bahnsen, "Reorientation measurements in the even nickel isotopes," *Nucl. Phys. A* **223** no. 3, (1974) 563 – 576.

[71] N. Stone, "Table of nuclear electric quadrupole moments," *At. Data Nucl. Data Tables* (2016) –.

[72] T. Sanami, M. Hagiwara, T. Oishi, M. Baba, and M. Takada, "A Bragg curve counter with an active cathode to improve the energy threshold in fragment measurements," *Nucl. Instr. Meth. Phys. Res. A* **589** no. 2, (2008) 193 – 201.

[73] J. Asselineau, J. Duchon, M. L'Haridon, P. Mosrin, R. Regimbart, and B. Tamain, "Performance of a Bragg curve detector for heavy ion identification," *Nucl. Instr. Meth. Phys. Res.* **204** no. 1, (1982) 109 – 115.

[74] G. Westfall, J. Yurkon, J. V. D. Plicht, Z. Koenig, B. Jacak, R. Fox, G. Crawley, M. Maier *et al.*, "A logarithmic detection system suitable for a 4π array," *Nucl. Instr. Meth. Phys. Res. A* **238** no. 2, (1985) 347 – 353.

[75] G. Santos, J. Acquadro, P. Gomes, R. Anjos, R. L. Neto, N. Added, N. Medina, N. Carlin *et al.*, "The Brazilian Bragg curve detector built for AMS studies," *Nucl. Instr. Meth. Phys. Res. B* **172** no. 1, (2000) 310–315.

[76] C. Schiessl, W. Wagner, K. Hartel, P. Kienle, H. Körner, W. Mayer, and K. Rehm, "A Bragg-curve spectroscopy detector," *Nucl. Instr. Meth. Phys. Res.* **192** no. 2, (1982) 291 – 294.

[77] O. Tarasov and D. Bazin, "Development of the program LISE: application to fusion-evaporation," *Nucl. Instr. Meth. Phys. Res. B* **204** no. Complete, (2003) 174–178.